UNIVERSITY OF ALBERTA

Applications of Multimode Interference Couplers in Wavelength-Division Multiplexing

BY

Mohammad Reza Paiam

A thesis submitted to the faculty of Graduate Studies and Research in partial fulfillment of the requirements for the degree of **Doctor of Philosophy**.

DEPARTMENT OF ELECTRICAL AND COMPUTER ENGINEERING

Edmonton, Alberta
Fall, 1997

National Library
of Canada

Acquisitions and
Bibliographic Services

395 Wellington Street
Ottawa ON K1A 0N4
Canada

Bibliothèque nationale
du Canada

Acquisitions et
services bibliographiques

395, rue Wellington
Ottawa ON K1A 0N4
Canada

Your file Votre référence

Our file Notre référence

The author has granted a non-exclusive licence allowing the National Library of Canada to reproduce, loan, distribute or sell copies of this thesis in microform, paper or electronic formats.

L'auteur a accordé une licence non exclusive permettant à la Bibliothèque nationale du Canada de reproduire, prêter, distribuer ou vendre des copies de cette thèse sous la forme de microfiche/film, de reproduction sur papier ou sur format électronique.

The author retains ownership of the copyright in this thesis. Neither the thesis nor substantial extracts from it may be printed or otherwise reproduced without the author's permission.

L'auteur conserve la propriété du droit d'auteur qui protège cette thèse. Ni la thèse ni des extraits substantiels de celle-ci ne doivent être imprimés ou autrement reproduits sans son autorisation.

0-612-23053-8

Canada

UNIVERSITY OF ALBERTA

RELEASE FORM

NAME OF AUTHOR: **Mohammad Reza Paiam**

TITLE OF THESIS: **Applications of Multimode Interference Couplers in Wavelength-Division Multiplexing**

DEGREE: **Doctor of Philosophy**

YEAR THIS DEGREE GRANTED: **1997**

Permission is hereby granted to the University of Alberta Library to reproduce single copies of this thesis and to lend or sell such copies for private, scholarly or scientific research purposes only.

The author reserves all other publication and other rights in association with the copyright in the thesis, and except as hereinbefore provided, neither the thesis nor any substantial portion thereof may be printed or otherwise reproduced in any material form whatever without the author's prior written permission.

M. R. Pai

#24, 11th Street
Northern Golnaz Avenue
Sattarkhan, Tehran
Iran, 14516

DATE: Sep 26/1997

UNIVERSITY OF ALBERTA

FACULTY OF GRADUATE STUDIES AND RESEARCH

The undersigned certify that they have read, and recommend to the Faculty of Graduate Studies and Research for acceptance, a thesis entitled **Applications of Multimode Interference Couplers in Wavelength-Division Multiplexing** submitted by **Mohammad Reza Paiam** in partial fulfillment of the requirements for the degree of **Doctor of Philosophy**.

R. I. MacDonald, Supervisor

J.N. McMullin

J. N. McMullin

A. M. Robinson

F.E. Vermeulen

F. E. Vermeulen

Doug Gingrich

D. M. Gingrich

S. Charbonneau

S. Charbonneau, External Examiner

DATE: SEP 22/1997

For my Parents and my Wife.

Their support and devotion over the years
have made this work possible.

Abstract

Modal interference in homogeneous planar multimode optical waveguides results in a self-imaging property by which an input field is reproduced in single or multiple images at periodic intervals along the propagation direction of the guide. Using this property, multimode interference (MMI) couplers can provide splitting and combining of optical beams. MMI couplers have good attributes such as compact size, low loss, ease of fabrication, relative insensitivity to polarization, and good fabrication tolerances. There is a growing interest in using MMI couplers in complex photonic integrated circuits such as wavelength multiplexers and optical switches.

Wavelength-division multiplexing (WDM) is an effective method of exploiting the large bandwidth of optical fibers. In addition to increasing the transmission capacity of a point-to-point link, WDM is also becoming important in optical networks for routing and circuit switching. This thesis is mainly concerned with the design and development of novel wavelength multiplexers using MMI couplers.

First, the underlying self-imaging principle in generalized MMI couplers is reviewed. Analytical expressions describing the positions, intensities, and phases of the self-images are given. Optical bandwidth and fabrication tolerances of the MMI couplers are examined. The measured performance of several five-port MMI couplers, which were fabricated in the course of the work, are reported. These measured values indicated good agreement with the theoretical predictions. A silicon oxynitride rib waveguide system was used for device fabrication throughout this thesis.

Next, the design of a new class of planar phased-array wavelength multiplexers known as MMI-phasar multiplexers is considered. An MMI-phasar device consists of two MMI couplers connected by an array of N monomode waveguides. The MMI couplers function as power splitters/combiners and the waveguide array as a dispersive element. A general theoretical formulation for the MMI-phasar multiplexers is presented and a simple procedure for finding an optimum set of lengths for the array guides is given. It is shown that these devices can operate as $N \times N$ wavelength-selective interconnecting components. Also, it is demonstrated that sidelobes in the multiplexer spectral response can be suppressed by weighting the power samples in the array guides with an appropriate MMI nonuniform power splitter. Furthermore, tunable wavelength multiplexing and dynamic wavelength routing can be obtained by incorporating phase-shifters on the array guides of the MMI-phasar devices. Two variations of a five-channel multiplexer with 2-nm channel spacing at 1550-nm wavelength were designed and fabricated. Both simulated and experimental results are presented.

Finally, a 980/1550-nm wavelength multiplexer useful for integration with rare-earth doped waveguide amplifiers and lasers is discussed. This multiplexer has a simple structure consisting of a central multimode waveguide and three access guides. The device operation is based on wavelength-selective coupling in the multimode waveguide, where one wavelength is in the cross-coupled state and the other is bar-coupled. The waveguide parameters and, in particular, the coupler width, are chosen to optimize the device performance. High performance with a compact device was achieved.

Acknowledgments

I would like to express my most sincere thanks to my supervisor Dr. Ian MacDonald for his constant guidance, support, and encouragement. His vast technical knowledge, insight, and experience have been sources of strength for me throughout this work. Also, I want to acknowledge Dr. James McMullin and Dr. Barrie Keyworth who had numerous inputs to this work and were always willing to offer their technical advice.

I would like to thank all the staff and students, past and present, of the Telecommunications Research Laboratories (TRLabs) for providing a pleasant and superb research environment. In particular, I want to thank all the members of the HyPIC project for their moral support and camaraderie. My special thanks are due to Dino Corazza, Chris Janz, Madhu Krishnaswamy, Rajkumar Nagarajan, Ray DeCorby, Neil Lagali, Alan Hnatiw, David Boertjes, Heather Hnatiuk, Dr. Ken McGreer, Nona McDonagh, Luke Chong, and David Clegg.

I extend my thanks to the staff of the Alberta Microelectronic Center (AMC) for the training and for their technical assistance during various stages of fabrication of the devices reported in this thesis. In this regard, I would like to mention Dr. James Broughton, Tran Tran, Graham McKinnon, Glen Fitzpatrik, and Yan Loke.

I would also like to thank the members of my examining committee for their effort and diligence in reading the manuscript of this thesis.

Finally, I am grateful to my family, particularly my parents and my wife for their support, love, and encouragement over the years.

Table of Contents

1. Introduction **1**
  1.1 Multimode Interference Couplers 4
  1.2 Wavelength Multiplexers 7
  1.3 Thesis Outline 11

2. Theory of Multimode Interference Couplers **13**
  2.1 Slab Waveguides 13
    2.1.1 Effective Index Method 19
  2.2 Modal Propagation Analysis 21
  2.3 General Self-Imaging Properties in $N \times N$ Multimode Interference Couplers 23
    2.3.1 From Modal Representation to Self-Images 28
    2.3.2 Derivation of the Phases 32
  2.4 Overlapping-Image Multimode Interference Couplers 34
    2.4.1 Uniform Power Splitters 39

3. Performance of Multimode Interference Couplers **41**
  3.1 Waveguide Structure and Device Fabrication 41
  3.2 Five-Port MMI Couplers 45
    3.2.1 Waveguide Losses 51
  3.3 Tolerances of MMI Couplers 52
    3.3.1 Fabrication Tolerances 54
    3.3.2 Optical Bandwidth 56
    3.3.3 Polarization Dependence 58

4. Phased-Array Wavelength Multiplexers Using Multimode Interference Couplers **60**
  4.1 Basic Device Structures and the Operation Principle 60
  4.2 Theoretical Formulation and Device Design 65
  4.3 Five-Channel Multiplexers 73
  4.4 Application as Dynamic Wavelength Routers 81
  4.5 MMI-phasar for Multiwavelength Laser Applications 82
    4.5.1 A Twelve-Channel Multiplexer 83

5. MMI Couplers for Broadly-Spaced Dual-Channel Wavelength Demultiplexing 87
5.1 Compact 980/1550-nm Wavelength Demultiplexer....88
5.2 Polarization-Insensitive 980/1550-nm Wavelength Demultiplexer 94

6. Summary and Conclusion....97
6.1 Future Work 100

References 102

List of Tables

Table 2.1 Summary of different multimode interference types that result in N outputs with uniform power. 40

Table 3.1 Various parameters of the five-port MMI couplers designed and implemented in the SiON–SiO$_2$ rib waveguide system. 46

Table 3.2 Analytical estimates of the fabrication tolerances and optical bandwidth of the five-port MMI couplers for 0.5 dB excess losses. 53

Table 4.1 Values of $\psi_{j,k}$ for the case of $m = 2$ in a five-channel multiplexer. The last column shows the value of $d_j^{\max}$ for each possible set of values of d_j. The shaded row, which corresponds to the smallest $d_j^{\max}$, is used to obtain an optimum set of values of d_j. Channel assignment of the multiplexer can be determined from the shaded column. 69

Table 4.2 Optimum set of values of the array arm factor d_j for an N-channel multiplexer. The cases of $N = 3$ to as high as $N = 12$ are shown. 70

Table 4.3 Wavelength assignment of a five-channel MMI-phasar multiplexer. A 5 × 5 WDM interconnection is possible. 71

Table 4.4 Various parameters of the designed five-channel multiplexers. 73

List of Figures

Figure 1.1 Schematic diagram of a WDM transmission link. 2

Figure 1.2 Layout of a conventional directional coupler. 4

Figure 1.3 Layout of a general $N \times N$ MMI coupler. Light from any of the input ports is launched into the MMI section, propagated, and imaged into the output ports of the coupler. 6

Figure 1.4 Schematic diagram of an arrayed-waveguide grating multiplexer. 8

Figure 1.5 Operation of the AWG multiplexer as (a) $N \times N$ WDM interconnect and (b) add-drop wavelength multiplexer with loop-back configuration. 9

Figure 1.6 Layouts of (a) an erbium-doped waveguide amplifiers and (b) an erbium-doped waveguide ring laser, which use wavelength-selective MMI couplers for (de)multiplexing the pump and signal lights. 11

Figure 2.1 The symmetric three-layer slab waveguide with the step-index profile shown on the right. 13

Figure 2.2 Amplitude distributions of the bound modes of a symmetric slab waveguide of width W. The first six modes are shown. The modes can be assumed to be confined within an effective width of W_e. 17

Figure 2.3 A ridge waveguide is modeled as an equivalent slab waveguide. (a) Schematic diagram of a ridge waveguide, (b) the equivalent symmetric three-layer slab waveguide with the effective step-index profile shown on the right. 20

Figure 2.4 The effective refractive indices of the equivalent slab waveguide are obtained by solving the equations of the slabs defined along the vertical dashed lines on the ridge structure. 20

Figure 2.5 Schematic view of a practical $N \times N$ MMI coupler implemented in a ridge waveguide system (the case of $N = 5$ is shown). 24

Figure 2.6 Any input field to a general MMI coupler of length $L_c = 3L_\pi/N$ is recreated in the form of N images at the output plane of the coupler. These output images have equal power and different phases. 25

Figure 2.7 MMI section with input light distribution $T(x)$ and decomposition into the bound modes $F_\nu(x)$ of the structure. For theoretical purposes the functions $F_\nu(x)$ and $T(x)$ are antisymmetrically extended to the virtual MMI section and periodically repeated on the whole x axis. 27

Figure 2.8 MMI section with length $L_c = 3L_\pi / N$ produces N images of the extended input field $T_{ext}(x)$. The real MMI section of effective width W_e contains N images of the real input $T(x)$ at the output of the MMI. Half of the images are phase-inverted. 30

Figure 2.9 Schematic diagram of a general $N \times N$ MMI coupler. Input and output positions have a free parameter a, which is limited to $0 \le a \le W_e / N$ 31

Figure 2.10 An $N \times N$ MMI coupler with equally spaced access guides. The same numbering direction has been used for both input and output guides 34

Figure 2.11 Overlapping-image MMI coupler with a reduced number of images. There is a pair of overlapped images at every other output position. (a) Outputs have been numbered in the opposite direction to that of inputs. (b) The same numbering direction has been used for both inputs and outputs. 37

Figure 2.12 Schematic diagram of a $1 \times N$ MMI power splitter where parameters h_2 and N' have to be chosen from $h_2 = 1, 2$ and $N' = 2N + h_2, 2N + h_2 - 1$ such that the term $h_1 + h_2 + N'$ is even. Depending on the position of the input guide, both equal and unequal power splitting is possible. All the values of h_1 except $N'/2$, $N'/3$, and $2N'/3$ result in nonuniform power distributions. 39

Figure 3.1 Cross-section of the SiO_2–SiON rib waveguide. The numbers inside the brackets indicate the refractive index values at 1550-nm wavelength. 42

Figure 3.2 Photolithography and RIE process steps involved in the fabrication of the SiON–SiO_2 rib waveguide. 44

Figure 3.3 A SEM picture illustrating the rib profile. 45

Figure 3.4 Scalar contour plot of the field distribution in the single-mode rib waveguide. The contours correspond to the intensity levels at 10% intervals from 10% to 90%... 45

Figure 3.5 Light intensity pattern in the 5×5 MMI coupler, showing the excitation at input 3 (top) and input 1 (bottom). 47

Figure 3.6 SEM picture of (a) the 5×5 MMI coupler fabricated in the rib waveguide structure, and (b) the magnified view of the output junction of the coupler. 48

Figure 3.7 SEM picture of the 1×5 MMI power splitter. 48

Figure 3.8 A picture showing the top view of actual light propagation in the 5×5 MMI coupler and its access guides. The picture was taken by a CCD camera, and a visible light wavelength of 670 nm was used. 49

Figure 3.9 Experimental set-up used for measuring the transmission of the MMI couplers. 49

Figure 3.10 Measured on-chip transmission loss of the 5 × 5 MMI coupler at 1550-nm wavelength; the 7-dB inherent loss of the coupler is included. Each group of bars relates to the five images of an input. The estimated error in the measurements is ±0.2 dB. 50

Figure 3.11 On-chip transmission loss of the 1 × 5 MMI nonuniform power splitter at 1550-nm wavelength. 51

Figure 3.12 Insertion loss of the 5 × 5 MMI coupler as a function of the coupler length. A wavelength of 1550 nm was used. 54

Figure 3.13 Typical relative transmission of the outputs of the 5 × 5 coupler as a function of the coupler length. 55

Figure 3.14 Typical phase deviations of the outputs of the 5 × 5 MMI coupler as a function of the coupler length. 56

Figure 3.15 Experimental arrangement used for measuring the optical bandwidth of the MMI couplers. 57

Figure 3.16 Optical bandwidth of the 5 × 5 MMI coupler. The performance has been considered at a coupler length of 715 μm. 57

Figure 3.17 Optical bandwidth of the 1 × 5 MMI nonuniform power splitter. The performance has been considered at a coupler length of 355 μm. 58

Figure 4.1 General layouts of MMI-phasar multiplexers. Array guides do not cross, and the shortest array guide can be any arm other than arm 1 or arm N (i.e., $m \neq 1, N$). (a) With an $N \times N$ MMI coupler as the power splitter, (b) with a $1 \times N$ MMI nonuniform power splitter. 62

Figure 4.2 General layout of an MMI-phasar multiplexer that is similar to the structure depicted in Figure 4.1(a) except that the shortest array guide in this case is the first arm ($m = 1$). 63

Figure 4.3 Normalized output power distribution of a 1 × 5 MMI nonuniform power splitter versus the array guide factor (d_j). The number next to each symbol indicates the corresponding output j. 74

Figure 4.4 Layouts of the five-channel MMI-phasar multiplexers with the optimized set of values d_j: (a) with a 5 × 5 MMI coupler as the power splitter, (b) with a 1 × 5 MMI nonuniform power splitter. 75

Figure 4.5 Layout of the five-channel MMI-phasar multiplexer in which the shortest array guide is the first arm ($m = 1$)....76

Figure 4.6 Spectral response of the multiplexer of Figure 4.4(a). The response of all five routes associated with one input guide are shown only. The routes originating from other inputs have similar transmissions. (a) Simulated performance. (b) Measured response....78

Figure 4.7 Spectral response of the multiplexers of Figure 4.4(b); the transmission at only one output guide is displayed. Other routes behave similarly. (a) Simulated performance. (b) Measured response....79

Figure 4.8 Simulated spectral response of the multiplexer of Figure 4.5; the response of only one route is displayed....80

Figure 4.9 Expected spectral response of a combined configuration of multiplexers of Figures 4.4(b) and 4.5. Only one channel is shown....80

Figure 4.10 Layout of an MMI-phasar WDM cross-connect switch....82

Figure 4.11 Schematic diagram of a multifrequency laser incorporating the MMI-phasar multiplexer as an intra-cavity filter....83

Figure 4.12 Layout of the 12-channel MMI-phasar multiplexer. Parameters h_1 and N' of the 1×12 MMI nonuniform power splitter are as described in the text....84

Figure 4.13 Simulated spectral response of the 12-channel MMI-phasar multiplexer. The transmission of only the center channel is displayed. Other channels have similar transmissions, except for appropriate wavelength shifts of integer multiples of the channel spacing (1 nm). (a) With nonuniform power splitter as depicted in Figure 4.12, (b) with equal power splitting....85

Figure 5.1 Calculated beat length ratio ($L_\pi^{980} / L_\pi^{1550}$) as a function of the MMI coupler width; TE polarization. A ratio of 1.5 (3 /2) is predicted at a width of about 6 μm.......89

Figure 5.2 Top view of the demultiplexing coupler. 980-nm wavelength is in bar-coupled state and 1550 nm is cross-coupled. The widths of the multimode section, input guide, top and bottom output guides are 6, 3, 2.3 and 3 μm, respectively.....90

Figure 5.3 A SEM picture of the 0.7 μm gap at the output junction of the MMI demultiplexing coupler....90

Figure 5.4 Simulated light intensity pattern in the 980/1550 nm demultiplexing coupler. The upper and lower pictures represent the 980- and 1550-nm wavelength, respectively....91

Figure 5.5 Simulated TE performance of the MMI demultiplexing coupler as a function of the coupler length (L_c). The multimode section is 6-μm wide..............................92

Figure 5.6 Schematic diagram of the experimental arrangement used for testing the 980/1550-nm wavelength demultiplexer..............................93

Figure 5.7 Measured TE performance of the fabricated devices with coupler length (L_c) varying in steps of 5 μm. The multimode section is 6-μm wide. Thin lines are quadratic curve fits and thick lines are fourth degree polynomial fits..............................93

Figure 5.8 Cross-section of the rib waveguide structure for the polarization-insensitive MMI demultiplexing coupler..............................94

Figure 5.9 Beat length ratio as a function of the MMI coupler width (TE polarization). Also, the beat length difference of the two polarizations ($L_{\pi,\mathrm{TM}} - L_{\pi,\mathrm{TE}}$) is shown for both wavelengths; thin solid line and thin dashed line relate to 980 nm and 1550 nm, respectively..............................95

Figure 5.10 Modeled performance of the polarization-insensitive 980/1550 nm demultiplexing coupler as a function of the coupler length (L_c). The MMI coupler is 6.5-μm wide..............................95

List of Symbols

a	free offset parameter used in positioning the access ports of a MMI coupler
a_ν	amplitude coefficient of the ν-th normalized mode in an optical waveguide (complex)
A	an integer variable
B	a real-valued constant
b	an integer variable
c	speed of light in free space
C	constant coefficient used in self-imaging analysis
d_j	the array arm factor related to the j-th arm of a MMI-phasar device
E	electric field
f	time-dependent field or wave function (complex)
F, F_ν	amplitude distribution of a modal field, F of the ν-th mode
H	magnetic field
h_1, h_2	parameters of a $1 \times N$ MMI nonuniform power splitter
i	index denoting the input ports of a MMI-phasar
j	index denoting the array arms of a MMI-phasar; also $\sqrt{-1}$
k	index denoting the output ports of a MMI-phasar
K	wave number in free space ($2\pi/\lambda$)
l	index indicating waveguide layer in a slab waveguide
L	length
L_c, L'_c	optimum length of a multimode interference coupler, optimum length of an overlapping-image multimode interference coupler
L_j	length of the j-th arm in a MMI-phasar
L_π, L_π^λ	beat length, beat length at wavelength λ
m	index denoting the shortest arm in the array of a MMI-phasar, i.e., L_m is the shortest arm
M	a positive integer such that M and N have no common divisors
n, n_l	index of refraction, refractive index of the l-th layer in a slab waveguide

n_{cl}	slab effective index (transverse analysis) at the cladding region of a ridge waveguide
n_e, n_{e0}	effective index of a mode, the value of n_e at the center wavelength λ_0
n_g	slab effective index (transverse analysis) at the guiding region of a ridge waveguide
N	the number of ports of a multimode interference coupler, the number of wavelength channels of a MMI-phasar
N'	total number of (overlapped) images in an overlapping-image MMI coupler
p, q	mode parameters; also, integer variables (in Chapter 5)
P, Q	parameters used in self-imaging analysis
r	output power distribution of a MMI coupler
s	an integer subscript denoting the wavelength channels of a MMI-phasar
t	time
T	the field in an optical waveguide (complex)
T_{ext}	the periodically extended field at the input plane of a MMI coupler
T_{out}	the field at the output plane of a MMI coupler
v	mode number
V	total number of the bound modes in a slab waveguide
w_o	Gaussian beam waist diameter
W	width of a rib waveguide, thickness of a slab waveguide
W_e	effective width of a multimode waveguide
x_i^{in}, x_j^{out}	lateral positions of input, output ports of a MMI coupler
x, y, z	Cartesian spatial coordinates

Greek Symbols

α_ν	amplitude coefficient of the ν-th mode in an optical waveguide (complex)
β, β_ν	propagation constant, the value of β for the ν-th mode
ΔL	the length which produces a phase shift of $2\pi/N$ between two adjacent wavelength channels of a MMI-phasar multiplexer
$\Delta\varphi$	phase difference between different signal components at the output of a MMI-phasar multiplexer

$\Delta\lambda$	channel spacing in the MMI-phasar multiplexer
ε_o	electric permittivity of free space
ϕ	phase constant
Φ	resultant phase of two overlapped images
φ	denotes the phase relation between inputs and outputs of a multimode interference coupler
λ	free-space wavelength
λ_0	center wavelength in a MMI-phasar multiplexer
λ_s	denotes the wavelength channels of a MMI-phasar
μ_o	magnetic permeability of free space
π	3.14159
ρ	a real number
σ	polarization parameter used in the analysis of the slab waveguides
ω	optical frequency
Ω	a parameter used in self-imaging analysis
ψ	denotes a function defined based on $\Delta\varphi$

List of Abbreviations

AMC	Alberta Microelectronic Center
ASE	Amplified Spontaneous Emission
AWG	Arrayed-Waveguide Grating
CCD	Charge-Coupled Device
Demux	Demultiplexer
DFB	Distributed Feedback
EDFA	Erbium-Doped Fiber Amplifier
EIM	Effective Index Method
FSR	Free Spectral Range
FWHM	Full-Width at Half-Maximum
HMDS	HexaMethylene DiSilazane
HyPIC	Hybrid Photonic Integrated Circuit
MMI	Multimode Interference
MMI-phasar	Phased-array wavelength division multiplexing device which is based on Multimode Interference Couplers
MUX	Multiplexer
OC-192	Optical Carrier-level 192
PECVD	Plasma Enhanced Chemical Vapour Deposition
RIE	Reactive Ion Etching
SEM	Scanning Electron Microscope
SiO_2	Silicon Oxide
SiON	Silicon Oxynitride
TDM	Time-Division Multiplexing
TE	Transverse Electric
TM	Transverse Magnetic
TRLabs	Telecommunications Research Laboratories
WDM	Wavelength-Division Multiplexing

1. Introduction

Telecommunications in the current information age is undergoing a large-scale transformation. With the proliferation of Internet and multimedia services, there is an ever increasing demand to transport large volumes of data. The widespread use of personal computers and the desire to connect them together and to information resources is intensifying the pressure to increase the capacity (bandwidth) available to the end-users. Photonic applications in the telecommunication networks are playing an important role in meeting this increasing bandwidth requirement. Today almost all high-capacity long-distance transmission links are realized using optical fibers. This has been made possible by the development of high-speed semiconductor lasers, photodetectors, low-loss inexpensive single-mode glass fibers, efficient erbium-doped fiber amplifiers, and various other photonic components. Single-mode optical fiber has a huge bandwidth, however this capacity has been far under-utilized up to now. The challenge is to find the most practical and cost-effective way of exploiting the inherent bandwidth of optical fiber.

The transmission capacity of an optical link can be increased by time-division multiplexing (TDM) or/and wavelength-division multiplexing (WDM). In TDM, several signals are multiplexed in the time domain and the aggregate high-speed signal is transmitted on a single optical carrier. Digital data in conventional optical communication are represented by pulses of light, and TDM accommodates higher bit rate by using narrower pulses. Currently the top-of-the-line commercially available system (OC-192) offers a bit rate of 10 Gb/s. However, because of the dispersion and nonlinearities in optical fiber and the limitations of electronics, it is getting very difficult to increase the data rate much beyond this level with TDM.

The multiplexing operation in the WDM approach is done in the optical domain where several independent optical carriers (wavelengths) are simultaneously transmitted along the fiber. Each wavelength can carry a TDM signal, and the total data rate is then directly proportional to the number of wavelengths used in the transmission system. A WDM transmission link is schematically shown in Figure 1.1. Early WDM systems were rather expensive because a separate optoelectronic regenerator was required for each wavelength to compensate for fiber optic loss and signal degradations. Optoelectronic regeneration is a process in which an optical signal is detected and converted into an electronic signal, which in turn is amplified and used to drive a laser diode, which recreates the original optical signal. Thus wavelength (de)multiplexers, multiple lasers, detectors, and the related electronic circuitry are needed at each optoelectronic regenerating station. But, the commercial significance of WDM transmission systems was fundamentally improved after the development of practical erbium-doped fiber amplifiers (EDFA) in the late 1980's. EDFA's provide a low noise and broadband gain in the 1.55-μm wavelength low-loss fiber band. An EDFA can amplify more than one wavelength at a time, thereby replacing multiple optoelectronic regenerators and reducing the cost of WDM systems. The optical bandwidth available in EDFA is approximately 30 nm or 3 THz, and the easiest way to access this bandwidth is through WDM.

The initial objective of WDM was to increase the capacity of point-to-point optical transmission links. However, it was soon realized that WDM can have network applications as well. A key feature of WDM is that discrete wavelengths form an orthogonal set of carriers which can be separated, routed, and switched without interfering with each other. Wavelength can be introduced as an additional network dimension to increase the flexibility and capacity of telecommunication networks. WDM technology enables us to implement in the optical domain some of the functions that had previously been done only in the electronic domain. Several applications of WDM in optical networks and a number of related WDM architectures have been discussed in [1].

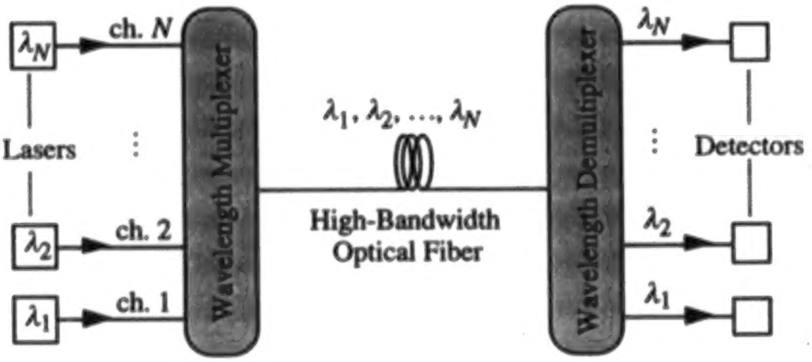

Figure 1.1 Schematic diagram of a WDM transmission link.

To realize the full potential of optical communications and to further extend the deployment of fiber optic networks, it is essential to develop various photonic components such as power splitters, space switches, modulators, and wavelength demultiplexers. These components must be technically sufficient, reliable, and cost effective. All these devices can be made as discrete components using bulk optics but the trend in photonic technology is toward using integrated optics and planar lightwave circuits to reduce the cost and add more functional complexity at the same time. This is similar to what has happened in the electronic industry where microelectronics technology has replaced discrete electrical components with integrated circuits. Photonics integrated circuits use the same fabrication processes that have already been established for years in the microelectronics industry. Optical devices that are based in planar lightwave technology are expected to be superior to their bulk-type counterparts in terms of reliability, compactness, and cost due to mass production.

Photonic integrated circuits consist mainly of optical waveguide structures. Optical waveguides are dielectric conduits that can confine the propagating light and transport it from one point to another. An optical guide is made up of a core material of one refractive index surrounded by a medium of lower refractive index. The basic concept of optical confinement in dielectric waveguides is total internal reflection, whereby light in the core of the guide is totally reflected at the interface with the surrounding medium. Light remains guided by undergoing multiple internal reflections as it travels along the length of the waveguide.

Passive waveguide couplers are among the key components of photonic integrated circuits since they can perform some important functions such as signal routing and splitting/combining of multiple optical beams. An interesting class of waveguide couplers known as multimode interference (MMI) couplers is rapidly gaining popularity for many applications in integrated optics. The MMI coupler has a simple structure consisting of a homogeneous planar multimode waveguide connected to a number of, usually single-mode, access guides. MMI couplers possess good characteristics such as low loss, compact size, and relaxed fabrication tolerances. In this thesis, various aspects of the MMI couplers are examined both theoretically and experimentally, and novel wavelength multiplexers are developed using these couplers. MMI couplers are briefly described in the next section, and a more comprehensive treatment of the related theory will be given in Chapter 2.

1.1 Multimode Interference Couplers

Optical couplers are essential components in photonic integrated circuits. The various planar optical components that have been developed to realize coupling and power splitting functions can be classified as diverging beam splitters, *Y*-branch splitters, inter-waveguide coupling devices (directional couplers), and multimode interference couplers. Diverging beam splitters [2] have an inherent nonuniformity and they are relatively large. Both *Y*-branch splitters [3] and directional couplers [4] suffer from poor reproducibility, large dimensions, and wavelength sensitivity; in addition, multiport couplers have to be formed as tree structures, which makes the device even longer.

Layout of a conventional or synchronous directional coupler is shown in Figure 1.2. Two single-mode waveguides are placed in sufficient proximity so that their evanescent fields overlap, resulting in a coupled waveguide system. There are two supermodes in this coupled system, a symmetric and an anti-symmetric one. The operation of the directional coupler relies on the beating between these two supermodes, which have different propagation constants. An input field to one of the guides excites both supermodes, which pass in and out of phase as they propagate. The lateral distribution of the total guided field changes as a function of the device length; the optical power is transferred between the guides. By properly choosing the device length, a 3-dB,

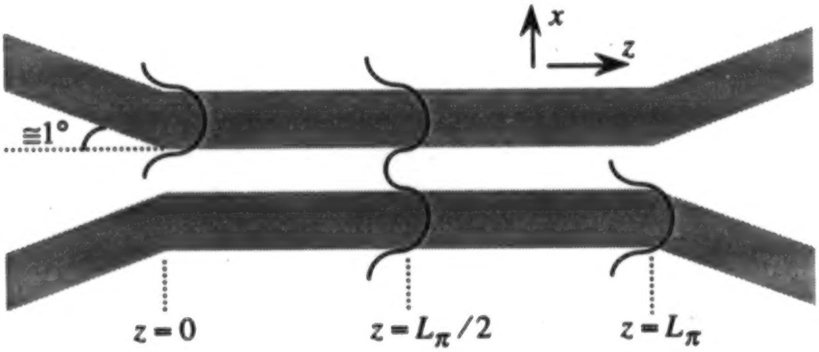

Figure 1.2 Layout of a conventional directional coupler.

cross, or bar coupler can be obtained. As shown in Figure 1.2, cross coupling and 3-dB coupling are achieved at device lengths of L_π and $L_\pi/2$, respectively, where the beat length L_π is defined as the propagation length over which the two supermodes acquire a phase difference of π radians. The interaction between the guides in a synchronous directional coupler is not strong and hence the beat length is very large, usually in the order of millimeters or centimeters. Furthermore, synchronous directional couplers cannot be implemented with deeply-etched rib waveguides since the guides have to be weakly confining to allow the lateral evanescent fields of the two guides to overlap. Thus, we cannot use large angles and tight bends for separating the access guides; a typical separation angle between the access guides would be about one or two degrees. This introduces extra coupling in the access guides, resulting in uncertainty in the actual length of the directional coupler. Also, the fabrication tolerances of the synchronous directional couplers are delicate since the waveguide dimensions have to be precisely controlled. All of these limitations can be overcome using multimode interference couplers.

Multimode waveguides can be used to form multiple images of an input excitation field. This self-imaging effect was first suggested by Bryngdahl [5] in 1973, and then was demonstrated by Ulrich *et al.* [6], [7] in planar glass waveguides. Using ray optics, they successfully described the formation of multiple images at certain device lengths. A few years later, Soldano *et al.* [8] used a modal propagation analysis to illustrate self-imaging or mode-beating in multimode guides. The modes of a multimode guide have different amplitude distributions and travel with different speeds determined by their effective refractive indices. The relation between the effective indices of the modes of a multimode guide is such that the modes interfere constructively at certain lateral positions at periodic intervals along the propagation direction. In other words, images of the field input to the multimode waveguide are reproduced at those positions. An MMI coupler consists of a multimode waveguide that is single-mode in the transverse direction and multimode on the lateral direction, connected to a number of, usually single-mode, input/output access guides. As an example, the layout of a general $N \times N$ MMI coupler is shown in Figure 1.3. A field distribution at any of the N inputs is reproduced at the output plane of the coupler in the form of N self-images that have equal magnitudes and different phases. The MMI coupler has a characteristic length L_c that is simply determined by the waveguide parameters and the coupler width, as will be described in Chapter 2.

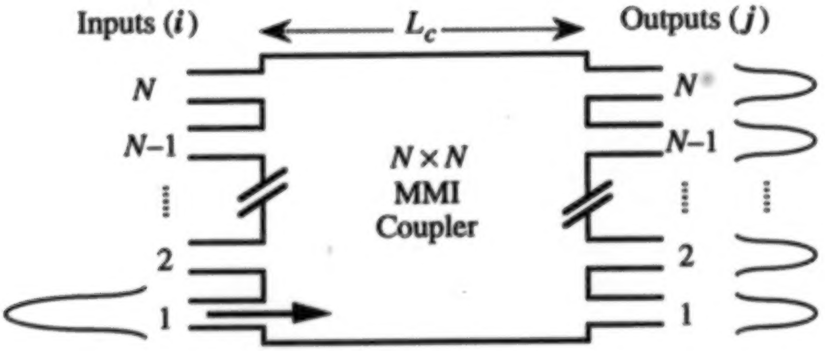

Figure 1.3 Layout of a general $N \times N$ MMI coupler. Light from any of the input ports is launched into the MMI section, propagated, and imaged into the output ports of the coupler.

MMI couplers are almost always designed in highly confining waveguide structures that prevent coupling between the access guides. This avoids uncertainty in determining the actual coupler length, a problem common with conventional directional couplers. Hence, MMI couplers are easy to design, and have small sizes and relaxed fabrication tolerances. Also, MMI couplers have low losses because of efficient imaging of the input field onto the output guides.

The uniformity or balance of MMI couplers is much better than that of the conventional directional couplers. The uniformity of power splitters/combiners employed in Mach–Zehnder switches and wavelength-division multiplexers translates directly into crosstalk. For example, a 0.5-dB power imbalance would limit the crosstalk to –25 dB. With respect to uniformity, MMI couplers operate fundamentally differently from conventional directional couplers. The output powers of a conventional directional coupler are proportional to $\cos^2(\pi z / 2L_\pi)$ and $\sin^2(\pi z / 2L_\pi)$, meaning that the sensitivity of the transmission to length variations is maximum at the 3-dB point. As will be shown later in Chapter 3, each self-image in an MMI coupler is at a local maximum with respect to the coupler length, implying that the sensitivity is minimum at the optimum coupler length of L_c, and that all output powers decrease similarly for deviations from the optimum length. Consequently, a very good uniformity is maintained over a large range of fabrication and operational variations.

The theory, properties and several applications of the MMI couplers have been covered in the literature. A general theoretical treatment of the self-imaging properties of the MMI couplers has been provided in [9] and [10]. Optical bandwidth and the fabrication tolerances of the MMI couplers have been considered in [11]. Reflection properties of the MMI devices have been studied in [12]. MMI couplers have been implemented in various materials and technologies. In addition to their use as single couplers and power splitters [13]–[22], MMI devices have been applied to perform a number of other more complex functions [23]. MMI couplers have been utilized for polarization splitting [24]. They have been employed for combining the signal and the local oscillator power in an optical coherent receiver front-end [25]. They have proven successful outcoupling elements in waveguide ring lasers [26]. They have been used to realize very compact optical switches in the form of the generalized Mach–Zehnder structures [27]–[39]. MMI couplers can also allow for interesting new functionalities such as mode filtering, mode splitting/combining, and mode converting [10], [30].

1.2 Wavelength Multiplexers

Wavelength (de)multiplexers are key components of WDM communication systems. Wavelength (de)multiplexers have been demonstrated using various techniques including reflection gratings [31]–[33], planar microlenses [34], multiple reflections in glass plates [35], and cascaded Mach–Zehnder interferometers [36], [37]. A popular device, which has witnessed rapid progress in recent years, is the arrayed-waveguide grating (AWG) multiplexer. This device has been extensively covered in the literature [38]–[46]. Due to the increasing importance of AWG in the current WDM systems, a brief description of this device and its applications is given below.

Layout of an AWG multiplexer is displayed in Figure 1.4. The AWG consists of *N* input ports, *N* output ports, and two free-space regions (slab waveguides) connected by an arrayed-waveguide grating, all of which are integrated on the same substrate. The input light is diffracted in the first slab and coupled into the array waveguides. The array has sufficient number of waveguides to collect all the light power diffracted in the slab. The waveguides in the array are arranged so that the lengths of adjacent guides differ by a constant value. After traveling through the array, each component of light attains a different phase delay proportional to the length of the array guide. This results in wavelength-dependent wavefront tilting. The arrayed-waveguide operates like a concave diffraction grating. The light from the array guides is focused in the vicinity of the output ports by the second free-space region. The focal position depends on the wavelength because of the wavelength-dependent phase shift in the array. Hence, the light is separated as a function of wavelength, and each wavelength is coupled into its respective output port. The AWG operates at high diffraction order and, consequently, it can support a large number of narrowly-spaced wavelength channels.

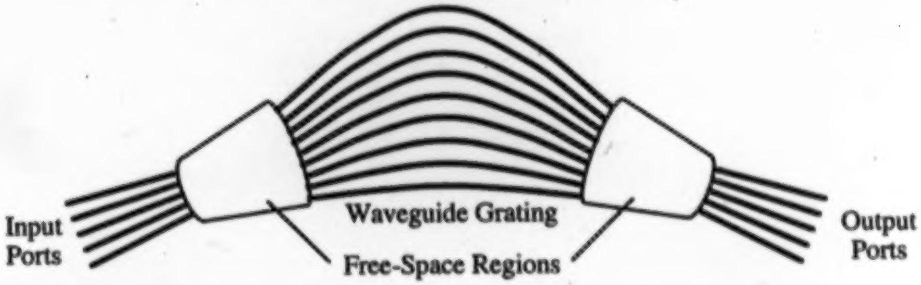

Figure 1.4 Schematic diagram of an arrayed-waveguide grating multiplexer.

The AWG has interesting wavelength-routing properties and can route WDM channels on the basis of not only their wavelengths but their input ports as well. Each of the N input ports can be used for WDM operation, but there is a cyclical relationship between the input port number, the output port number, and the optical channel number. That is, the same wavelengths are assigned to routes (i, k) and $(i + b, k + b)$, where i, k, and b represent the input port number, the output port number, and an integer variable, respectively. Therefore, in addition to basic wavelength (de)multiplexing operation, an AWG can offer functions such as $N \times N$ WDM interconnection, and wavelength add-drop multiplexing; see Figure 1.5. These functions are essential in WDM optical network applications. There are N^2 unique paths in an $N \times N$ interconnection and it is well known that the minimum number of wavelength channels required for an $N \times N$ WDM interconnection is N. As shown in Figure 1.5(a), the AWG makes efficient use of a given finite set of wavelengths to achieve the $N \times N$ interconnection, thereby replacing the N demultiplexers, N multiplexers, and N^2 fibers in an earlier reported WDM-based $N \times N$

optical network [1] by a single device. The second function is add-drop multiplexing, in which one or more wavelengths are dropped and inserted at a node in an optical network. The add-drop function requires a demultiplexer and a multiplexer. The input signal is demultiplexed and the drop-wavelengths are removed, then the remaining wavelengths and the wavelengths to be added are combined by a multiplexer. Using the loop-back configuration shown in Figure 1.5(b), a single AWG can perform the add-drop operation by acting as both a demultiplexer and a multiplexer at the same time. The wavelength channels are dropped and inserted by opening the respective loops.

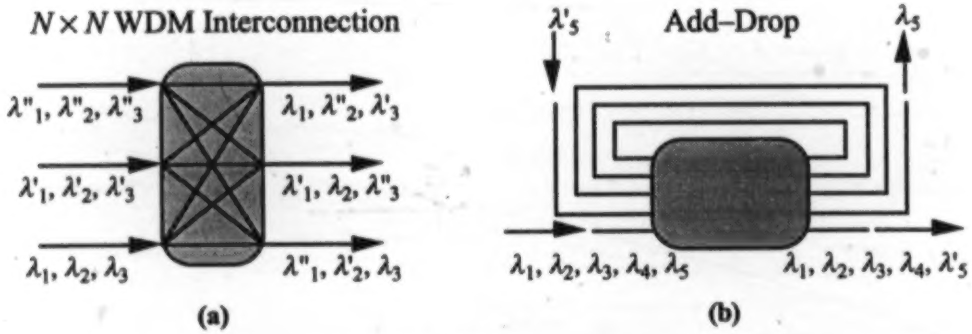
$N \times N$ WDM Interconnection
$\lambda''_1, \lambda''_2, \lambda''_3$
$\lambda'_1, \lambda'_2, \lambda'_3$
$\lambda_1, \lambda_2, \lambda_3$
$\lambda_1, \lambda''_2, \lambda'_3$
$\lambda'_1, \lambda_2, \lambda''_3$
$\lambda''_1, \lambda'_2, \lambda_3$
λ'_5
Add–Drop
λ_5
$\lambda_1, \lambda_2, \lambda_3, \lambda_4, \lambda_5$
$\lambda_1, \lambda_2, \lambda_3, \lambda_4, \lambda'_5$

(a) **(b)**

Figure 1.5 Operation of the AWG multiplexer as (a) $N \times N$ WDM interconnect and (b) add-drop wavelength multiplexer with loop-back configuration.

The AWG has been proposed for and/or applied in many other applications as well [45]–[50]. Fast tunable filters, lasers, and receivers operating over a wide optical frequency band can be realized by combining the passive AWG with active elements [45]. Low-cost passive optical networks based on AWG have been demonstrated [46]; these optical distribution systems have been proposed as upgradable local loop architectures to replace copper telephony. The AWG has been used as an intracavity filter in multiwavelength lasers [47]–[50]. The wavelength-routing properties of the AWG has made it a suitable choice for various WDM applications. The relevance of the AWG to our work is that the wavelength multiplexers, which we develop in this thesis, possess wavelength-routing characteristics and functionalities similar to those of the AWG.

The main aim of this thesis is to investigate how MMI couplers can be used for WDM functions. Towards this goal, we design and develop a new type of wavelength multiplexer, which consists of two MMI couplers interconnected by an array of N single-mode waveguides. The MMI couplers operate as power splitters/combiners, and the waveguide array is the dispersive element. The array guides have different lengths, and this induces relative phase delays proportional to the length difference between the guides. For brevity we refer to these MMI-based phased-array devices as MMI-phasar multiplexers. An MMI-phasar multiplexer operates on N equally spaced wavelength channels. The design of the MMI-phasar multiplexer is complicated by the fact that, unlike the AWG, the lengths of the array arms are not necessarily governed by a simple linear relationship. An important issue in the design of MMI-phasar multiplexer is finding an optimum combination of the lengths of the array arms that results in a compact device with the best spectral response. In Chapter 4, it is shown that MMI-phasar multiplexers can operate as $N \times N$ WDM interconnecting components and add-drop wavelength multiplexers. A five channel MMI-phasar was fabricated in a SiO_2–SiON rib waveguide system and its performance was measured. It is interesting to note that the number of guides in the array of the MMI-phasar is much smaller than that of the AWG. Consequently, it is possible to convert the MMI-phasar to a WDM cross-connect switch by placing phase shifters on the array arms, while this is not practicable for the AWG. A WDM cross-connect switch or dynamic wavelength router is highly desired in WDM optical networks because it is capable of reconfiguring the wavelength-routing on demand.

The wavelength multiplexers, which we have been discussing up to now, are known as dense wavelength multiplexers since their channel spacing is on the order of a few nanometers or less. However, coarse wavelength multiplexers are also required for some applications. For example, dual-channel coarse wavelength multiplexers are needed for combining/separating the signal and pump light before/after erbium-doped optical amplifiers. In erbium-doped optical amplifiers, the signal is in the 1550-nm band while the pump light is either 1480 nm or 980 nm. In the final portion of this thesis, we demonstrate a 980/1550-nm wavelength demultiplexer using MMI couplers and implemented in a SiO_2–SiON rib waveguide system. This device has a very simple structure consisting of a central multimode waveguide and three access guides. An MMI coupler can perform dual-channel wavelength demultiplexing when it is designed to be bar-coupled for one wavelength and cross-coupled for the other. Generally, the length of MMI couplers used for dual-channel wavelength multiplexing would be too long because MMI couplers are relatively insensitive to wavelength variations, but if the two wavelengths of interest are on the order of a few hundreds of nanometers apart, fairly small-size devices can be designed. Our work reveals that good performance with a compact multiplexer can be achieved. This multiplexer is a suitable candidate for integration with erbium-doped waveguide amplifiers and waveguide ring lasers, as shown in Figure 1.6.

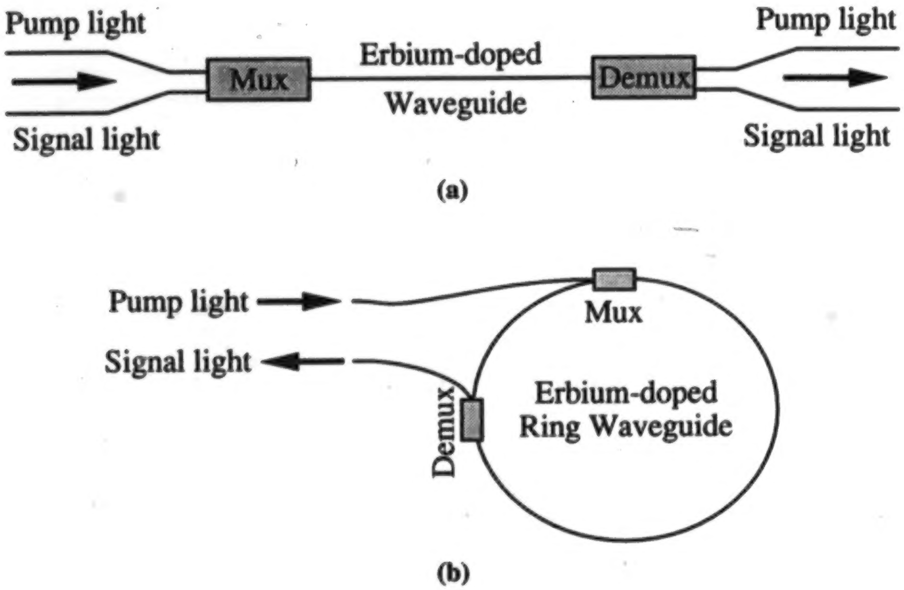
Pump light
Signal light
Mux
Erbium-doped
Waveguide
Demux
Pump light
Signal light
(a)
Pump light
Signal light
Mux
Demux
Erbium-doped
Ring Waveguide
(b)

Figure 1.6 Layouts of (a) an erbium-doped waveguide amplifiers and (b) an erbium-doped waveguide ring laser, which use wavelength-selective MMI couplers for (de)multiplexing the pump and signal lights.

1.3 Thesis Outline

This thesis can be separated into two main parts. The first part consisting of Chapters 2 and 3 deals with the theory and properties of the MMI couplers and the fabrication issues involved in this work. The second part comprising of Chapters 4 and 5 presents the work on the MMI-phasar and the 980/1550-nm wavelength multiplexers.

In Chapter 2 some theoretical aspects of optical waveguides relevant to the analysis of the MMI couplers are reviewed. Modal propagation analysis, which is used to simulate the propagation characteristics of light in MMI couplers, is described. Generalized self-imaging properties of the MMI couplers are derived. Overlapping-image MMI couplers, which permit both uniform and nonuniform power splitting, are discussed. Analytical expression that relate the coupler geometry to image intensities, positions, and phases are presented.

In Chapter 3 the waveguide structure and the fabrication procedure adopted in this work are explained. Optical bandwidth and fabrication tolerances of the MMI couplers are examined. A 5 × 5 general MMI coupler and a 1 × 5 overlapping-image MMI coupler are fabricated in a rib waveguide system and their transmissions are measured.

In Chapter 4 the design of the MMI-phasar multiplexers is considered. A general theoretical formulation for an *N*-channel multiplexer is presented, and a simple procedure for finding an optimum set of lengths for the array guides is provided. It is shown that these multiplexers can function as $N \times N$ wavelength-selective interconnecting components. Also, it is demonstrated that sidelobes in the multiplexer spectral response can be suppressed by employing an appropriate MMI nonuniform power splitter to suitably weight the power samples in the array guides. Two variations of a five-channel device with 2-nm channel spacing at 1550 nm are fabricated, and their performance are measured. Furthermore, the design of a 12-channel MMI-phasar multiplexer useful for application with multiwavelength lasers is examined.

In Chapter 5 a compact 980/1550-nm wavelength multiplexer consisting of a wavelength-selective MMI coupler and three access guides is demonstrated. This device is useful for integration with rare-earth doped waveguide amplifiers and lasers. It is shown that the device performance can be optimized with a right choice of the waveguide parameters and the coupler width. The device is fabricated in a rib waveguide system, and its experimental performance is compared with the simulated results.

2. Theory of Multimode Interference Couplers

This chapter provides the underlying theory of the self-imaging effect in planar multimode waveguides. The propagating light in a multimode waveguide can be decomposed into a set of orthogonal fields known as modes. The relation between the propagation constants of the modes of a homogeneous symmetric slab multimode waveguide is such that the modes interfere constructively at periodic intervals along the propagation direction. This mode-beating property results in the formation of images of the input excitation field. Let us begin our discussion by considering dielectric slab waveguides.

2.1 Slab Waveguides

Slab waveguides serve as useful approximate models for more complicated optical waveguide structures and can be used to illustrate the general characteristics of waveguide modes. As we shall see later, a comprehension of the modal characteristics of the symmetric three-layer slab waveguide is required to develop the theory of the MMI couplers. In their simplest forms, slab waveguides consist of a planar core layer with a higher refractive index than the two surrounding cladding regions. When the two cladding regions have the same refractive indices, the structure is called the symmetric slab waveguide. Figure 2.1 shows a symmetric slab waveguide with a core thickness of W. The light is confined in the x direction to the core region and propagates in the z direction. The following analysis in this section deals mainly with the symmetric slab waveguide.

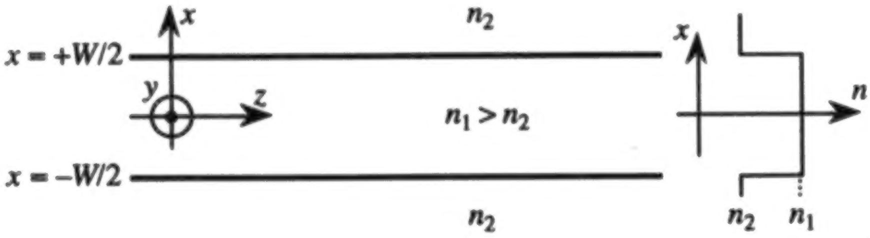

Figure 2.1 The symmetric three-layer slab waveguide with the step-index profile shown on the right.

Like any other electromagnetic field, light is described by two related vector fields: the electric field $E(x, y, z, t)$ and the magnetic field $H(x, y, z, t)$, where x, y, and z represent the positions in space, and t denotes the time. Each of these two vector functions consists of three components, which are (E_x, E_y, E_z) for the electric field and (H_x, H_y, H_z) for the magnetic field. The electric and the magnetic fields are related by Maxwell's equations. Assuming a linear, nondispersive, homogeneous, and isotropic medium with no free electric charges or currents, it can be shown through Maxwell's equations that each of the six components of E and H satisfies the wave equation given by

$$\nabla^2 f = \frac{n^2}{c^2}\frac{\partial^2 f}{\partial t^2}, \tag{2.1}$$

where f is a complex wave function, n is the refractive index of the medium, and c is the speed of light in free space. Let us assume that dependency of f on t and z can be fully described by

$$f(x, y, z, t) = F(x, y)\exp(j\omega t - j\beta z), \tag{2.2}$$

where ω is the optical frequency, β is the propagation constant, and F is a real-valued wave function called a mode. The modes form an orthogonal set of solutions of the wave equation and they propagate through the guide with their amplitude distributions unaltered. Slab waveguides are two-dimensional structures in the sense that the modal field F has no variations with respect to y, i.e.,

$$\partial F/\partial y = 0. \tag{2.3}$$

Hence, for slab waveguides the field F is one-dimensional and is a function of x only. Applying (2.2) and (2.3) to (2.1), the wave equation for each region of the slab becomes

$$\partial^2 F/\partial x^2 + (K^2 n_l^2 - \beta^2)F = 0, \tag{2.4}$$

where n_l is the refractive index of the l-th layer, K is the wave number in free space ($K = 2\pi/\lambda$), and λ is the wavelength in free space. The fields propagating in a waveguide must satisfy certain boundary conditions and so the problem becomes an eigenvalue one. This leads to a discrete set of solutions of (2.4) for the bound (or guided) modes. For the slab structure in Figure 1.1, the propagation constants of the bound modes lie in the range

$$Kn_2 < \beta < Kn_1. \tag{2.5}$$

The fields of the bound modes are exponential in the cladding and sinusoidal in the core layer. In addition to the bound modes there are other solutions with corresponding values of β smaller than Kn_2. These are radiation modes, which are sinusoidal in all layers and extend over all transverse space. Radiation modes have been ignored in this analysis since they are not significant in the operation of the practical MMI couplers.

We need to know which components of E and H are involved in the solutions. It can be shown that by applying condition (2.3) to Maxwell's equations the six components of E and H can be grouped into two independent and orthogonal sets. These two sets of fields are $\{E_y, H_z, H_x\}$ and $\{H_y, E_z, E_x\}$ known as transverse electric or TE and transverse magnetic or TM, respectively. The components of each set are related, and by determining only one component the other two in each set can be found, as well. For example, the relations between H_z and E_y, and E_z and H_y are

$$H_z = \frac{j}{\mu_o \omega} \frac{\partial E_y}{\partial x}, \tag{2.6}$$

$$E_z = -\frac{j}{\varepsilon_o n^2 \omega} \frac{\partial H_y}{\partial x}, \tag{2.7}$$

where μ_o is the permeability and ε_o is the permittivity in free space. Usually, solutions of E_y and H_y for TE and TM, respectively, are determined. Thus, the wave function F represents either E_y for the TE case or H_y for the TM case.

The fields are subject to boundary conditions. It is known from the electromagnetic theory that tangential components of E and H must be continuous across a dielectric discontinuity. For TE fields this implies that E_y and H_z must be continuous across planar dielectric boundaries perpendicular to the x axis in Figure 2.1. Similarly, for TM fields H_y and E_z must be continuous across dielectric boundaries. In view of Equations (2.6) and (2.7) these conditions imply that

$$\begin{array}{llll} \text{TE}: & E_y \text{ and } & \dfrac{\partial E_y}{\partial x} & \text{continuous} \\ \text{TM}: & H_y \text{ and } & \left(\dfrac{1}{n_i^2}\right)\dfrac{\partial H_y}{\partial x} & \text{continuous} \end{array} \tag{2.8}$$

across dielectric discontinuities.

Now, let us examine the solutions of the wave equation (2.4). To simplify the analysis, two mode parameters p and q, which have positive real values, are defined as

$$\begin{array}{ll} p^2 = K^2 n_1^2 - \beta^2 & \text{for the core layer,} \\ q^2 = \beta^2 - K^2 n_2^2 & \text{for the cladding layer.} \end{array} \tag{2.9}$$

It should be realized that p and q are not completely unrelated parameters. Their relationship can be clarified by eliminating β from (2.9) to get

$$p^2 + q^2 = K^2\left(n_1^2 - n_2^2\right). \tag{2.10}$$

For a symmetric slab waveguide it can be shown that solutions of (2.4) must be either even or odd functions. Using the definitions of p and q, the solutions for the modal fields derived from (2.4) can be written as

$$\begin{aligned}
&\text{core}\left(|x| < \frac{W}{2}\right): && F(x) = \begin{cases} \cos(px) & \text{for even modes,} \\ \sin(px) & \text{for odd modes,} \end{cases} \\
&\text{upper cladding}\left(x > \frac{W}{2}\right): && F(x) = B\exp(-qx) \qquad \text{for all modes,} \\
&\text{lower cladding}\left(x < -\frac{W}{2}\right): && F(x) = \begin{cases} B\exp(qx) & \text{for even modes,} \\ -B\exp(qx) & \text{for odd modes,} \end{cases}
\end{aligned} \tag{2.11}$$

where B is a constant, which is determined by considering the boundary conditions stated in (2.8). The value of B is given by

$$\begin{aligned}
B &= \cos(pW/2)\exp(qW/2) && \text{for even modes,} \\
B &= \sin(pW/2)\exp(qW/2) && \text{for odd modes,}
\end{aligned} \tag{2.12}$$

Also, note that the field given by (2.11) goes to zero at infinity. Applying the conditions of (2.8) to (2.11) at $x = W/2$ boundary results in the following constraint equations:

$$\begin{aligned}
q(n_1/n_2)^{2\sigma} &= p\tan\frac{pW}{2} && \text{for even modes,} \\
q(n_1/n_2)^{2\sigma} &= -p\cot\frac{pW}{2} && \text{for odd modes,}
\end{aligned} \tag{2.13}$$

where $\sigma = 0$ for TE and $\sigma = 1$ for TM. Expressions (2.13) and (2.10) define the constraints on β, p, and q. Values of β, p, and q that satisfy these constraints determine the bound modes that can propagate in the slab waveguide. By substituting for q from (2.13) in (2.10), we get

$$\begin{aligned}
p^2\left[1 + \left(\frac{n_2}{n_1}\right)^{4\sigma}\left(\tan\frac{pW}{2}\right)^2\right] &= K^2\left(n_1^2 - n_2^2\right) && \text{for even modes,} \\
p^2\left[1 + \left(\frac{n_2}{n_1}\right)^{4\sigma}\left(\cot\frac{pW}{2}\right)^2\right] &= K^2\left(n_1^2 - n_2^2\right) && \text{for odd modes.}
\end{aligned} \tag{2.14}$$

The value of p for each mode can be found from (2.14), and then the corresponding values of β and q are obtained from (2.9). By substituting for the values of p and q in (2.11), the amplitude distributions of the bound modes of the slab waveguide are found. As an example, the amplitude distributions of the first six modes of a symmetric slab waveguide are shown in Figure 2.2. The modes have been denoted by the mode number ν. The ν-th order mode is distinguished by having $\nu + 1$ lobes. The mode corresponding to $\nu = 0$ is also referred to as the fundamental mode. The modal power is not totally confined to the waveguide core since the exponential tails of the modes penetrate into the cladding. This lateral penetration depends on the waveguide characteristics and the mode order. In general, the modes can be assumed to be confined within an effective width W_e, which is larger than the actual width W of the guide. This effective width can be approximated by the effective width of the fundamental mode [51] and is given by

$$W_e \cong W + \left(\frac{\lambda}{\pi}\right)\left(\frac{n_2}{n_1}\right)^{2\sigma}\left(n_1^2 - n_2^2\right)^{-(1/2)} \tag{2.15}$$

where $\sigma = 0$ for TE and $\sigma = 1$ for TM. The difference between W_e and W gets smaller for waveguides with higher contrast (i.e., larger difference between n_1 and n_2).

The number of guided modes in a waveguide is always finite, and is dependent on the guide width, wavelength, and core and cladding indices. In the case of a symmetric

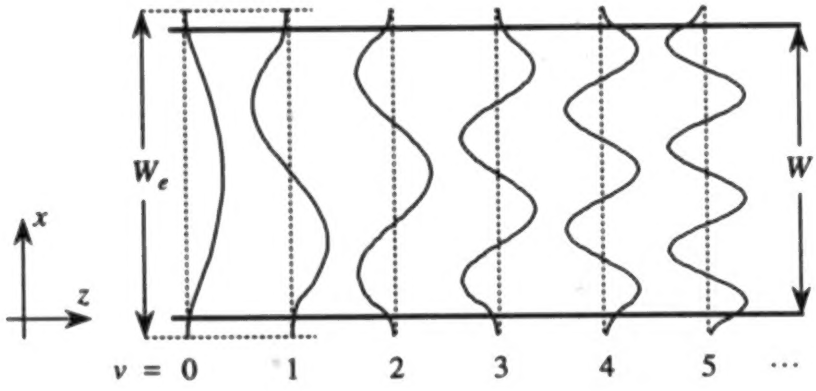

Figure 2.2 Amplitude distributions of the bound modes of a symmetric slab waveguide of width W. The first six modes are shown. The modes can be assumed to be confined within an effective width of W_e.

slab waveguide, the number of bound modes is limited by (2.5) and it can be shown [51] that the total number of guided modes V for each polarization is given by

$$V = \mathrm{Ceil}\left(\frac{2W}{\lambda}\sqrt{n_1^2 - n_2^2}\right), \tag{2.16}$$

where Ceil(x) is the smallest integer that is greater than or equal to x. The number of modes increases for larger waveguide thicknesses, larger differences of refractive indices, and for smaller values of wavelength.

If the refractive indices of the upper and lower claddings of the slab in Figure 2.1 are different, the structure is called an asymmetric slab waveguide. The asymmetric three-layer slab waveguide is treated similarly with a slight modification of the above formulation. Also, the above analysis, in principle, can be extended to the more general multi-layer (more than three layers) slab structures. The constants associated with the fields in two adjacent layers are related by a set of two linear equations. Since the number of constants and the number of linear equations grows by two for each additional interface in a multi-layer slab structure, the analysis soon becomes cumbersome as the number of layers increases. However, a method known as the transfer matrix approach [52] may be used to simplify the problem by multiplying 2×2 matrices relating the constants associated with the field for each layer, thus eliminating all constants except the one associated with the upper cladding and the one associated with the lower cladding. The determinant of the coefficients of these two remaining constants is set to zero to obtain the dispersion relation. Finally, the modes are found by solving the dispersion relation for β.

Most practical waveguide structures in photonic integrated circuits confine the optical field in both transverse dimensions (x and y directions). The field confinement in the y directions is achieved by features such as rib/ridge, channel, and strip loading. This two-dimensional transverse confinement can be used to direct the light to various locations on a substrate merely by defining the waveguide path. The boundary value problem for the two-dimensional modes in dielectric optical waveguides does not have a closed-form solution. A variety of numerical approaches based on discretizing the differential operators in the wave equation have been developed to find the modes in these waveguides. The numerical methods are accurate, but often complicated and computationally intensive. Moreover, they do not provide insight into the mechanism of the self-imaging effect in the MMI couplers. In addition to rigorous numerical techniques, a number of simpler analytical methods exist that produce approximate results, which are satisfactory for many cases. By far the simplest and the most popular of this group is the effective index method [53]–[57]. In the effective index method a waveguide with a two-dimensional profile is approximated as an equivalent slab waveguide. The relatively straightforward theory of slab waveguides is applied in conjunction with the effective index method to analyze the practical waveguides.

2.1.1 Effective Index Method

A ridge waveguide structure is schematically shown in Figure 2.3(a). The ridge is formed by etching the core layer. Ridge waveguides are the most suitable structures for designing MMI couplers and they have been employed in the device design and fabrication in this thesis. The basic idea of the effective index method (EIM) is to replace a rectangular structure such as a ridge waveguide by an equivalent slab with effective refractive indices. For example, the ridge waveguide of Figure 2.3(a) is replaced by the symmetric three-layer slab depicted in Figure 2.3(b). The thickness of the core layer of the equivalent slab is the same as the width W of the ridge. The effective refractive indices (n_g and n_{cl}) are obtained by solving the equations of the slab waveguides defined with index profiles as seen along each of the vertical dashed lines in Figure 2.4. It is assumed that the ridge waveguide is single-mode in the y-direction. Also, without loss of generality, it is assumed that the refractive indices of the layers of the ridge waveguide are such that $n_a > n_b \geq n_c$. The corresponding solution of the equivalent slab can be easily obtained after finding the effective indices n_g and n_{cl}. The propagation constants of the modes of the equivalent slab are approximately equal to those of the ridge waveguide. However, it is necessary to restrict the set of modes to those with propagation constants greater than Kn_b since only these solutions correspond to the bound modes of the ridge waveguide. Other solutions of the equivalent slab are spurious and should be ignored.

The EIM is the favorite approach for finding the modes of the guides used in the design of MMI couplers. It has been shown in the literature that the results of the EIM can be reasonably accurate in the limit of strongly confining waveguides with large ridge depths [57], [58]. Nevertheless, in general, the accuracy of the EIM varies with the waveguide structure and the mode order. The most significant parameter of an MMI

(a)

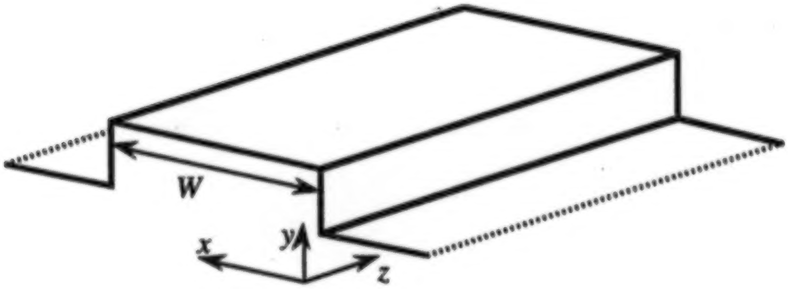

(b)

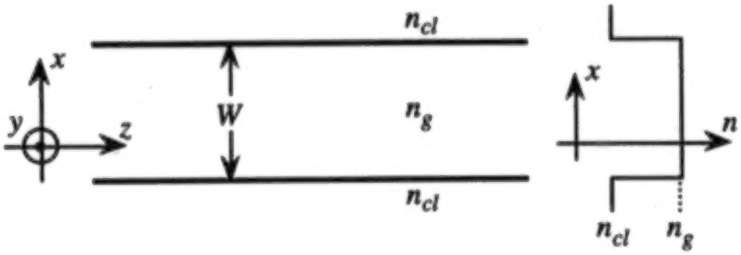
n_{cl}
x
y
z
W
n_g
n_{cl}
x
n
n_{cl}
n_g

Figure 2.3 A ridge waveguide is modeled as an equivalent slab waveguide. (a) Schematic diagram of a ridge waveguide, (b) the equivalent symmetric three-layer slab waveguide with the effective step-index profile shown on the right.

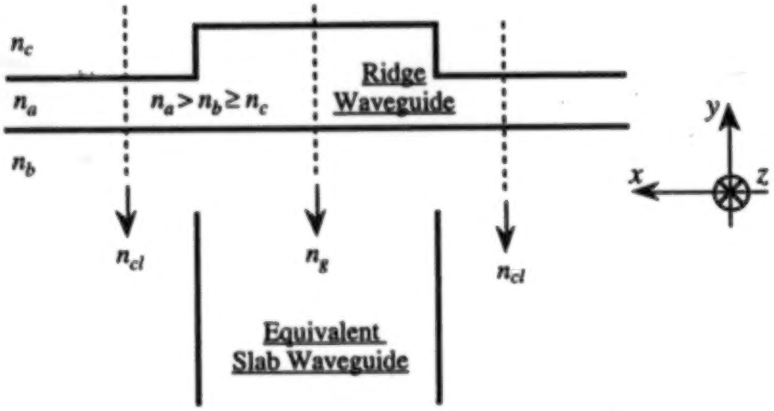
n_c
n_a
n_b
$n_a > n_b \geq n_c$
Ridge Waveguide
y
x
z
n_{cl}
n_g
n_{cl}
Equivalent Slab Waveguide

Figure 2.4 The effective refractive indices of the equivalent slab waveguide are obtained by solving the equations of the slabs defined along the vertical dashed lines on the ridge structure.

coupler is the beat length, and so it is desirable that both the ridge waveguide and its equivalent slab have the same beat lengths. The beat length L_π depends on the propagation constants of the first two modes and is defined as

$$L_\pi = \frac{\pi}{\beta_0 - \beta_1}, \tag{2.17}$$

where β_0 and β_1 are the propagation constants of the fundamental and first order modes, respectively. In our analysis, we first calculate the beat length of the ridge waveguide directly using a vectorial finite-difference 2D mode solver called FWave, which is available in the public domain [59]. Then the effective refractive index n_{cl} of the equivalent slab is chosen so that its beat length is the same as that of the ridge waveguide. Selecting a suitable value for n_{cl} is in harmony with the fact that in many cases no explicit solution for n_{cl} exists because the mode of the vertical slab defined at the region adjacent to the ridge might be beyond cutoff.

It was seen previously that the modes of a slab waveguide can be conveniently separated into orthogonal TE and TM polarizations. For non-slab waveguides such as ridge structures, purely orthogonal polarization states do not exist and the modes are not strictly TE or TM. In this case the modes are always hybrid, meaning that all three components of both the electric and magnetic fields are non-zero. However, for most practical waveguides, these six field components are not equally significant and some components are much stronger than the others. This leads to quasi-polarized modes referred to as quasi-TE and quasi-TM. It is assumed that the dominant field component are E_x and H_y for quasi-TE, and H_x and E_y for quasi-TM. The effective index method (EIM) can be used to solve for the modes of both polarizations. In the EIM, obviously the wave polarization has to be kept consistent when applying the slab analysis in each transverse direction. For example, in the case of quasi-TE, first the slab in the *y*-direction is solved for TE and then equivalent slab in the *x*-direction is solved for TM modes.

2.2 Modal Propagation Analysis

The modes of an optical waveguide constitute an orthogonal set and can be used to represent the propagating field in the waveguide. An MMI coupler consists of a central multimode guide and several input/output access guides; the stable propagating field in each of these sections can be expressed in terms of the local bound modes, having amplitudes determined by the transition relations at the junctions between the corresponding sections. Such a characterization of light propagation in waveguides is known as modal propagation analysis. Assuming an MMI coupler with its input plane at $z = 0$, an incoming field $T(x, 0^-)$ to the coupler can be written as

$$T(x,0^-) \cong \sum_{\nu} a_\nu \hat{F}_\nu(x), \tag{2.18}$$

where $\hat{F}_\nu(x)$ is a set of orthonormal functions obtained by appropriately normalizing the modal fields $F_\nu(x)$, i.e.,

$$\hat{F}_\nu(x) = \frac{F_\nu(x)}{\sqrt{\int_{-\infty}^{+\infty} \left|F_\nu(x)\right|^2 \mathrm{d}x}}, \tag{2.19}$$

and a_ν is a complex amplitude coefficient given by

$$a_\nu = \int_{-\infty}^{+\infty} \hat{F}_\nu^*(x) T(x,0^-) \mathrm{d}x, \tag{2.20}$$

where $\hat{F}_\nu^*(x)$ is the complex conjugate of $\hat{F}_\nu(x)$. It has been assumed that pre- and post-transition waveguides are sufficiently similar that any reflected power at the transition can be neglected. The number of guided modes is finite and some of the input power at the transition may be lost through radiation. This explains the approximation sign used in (2.18). For MMI couplers, the radiated power is not significant and is ignored in the modal analysis. Modal propagation analysis is not suitable for applications where the distribution of power radiated from a structure is important. Now, after determining the amplitude coefficients a_ν, the field in the MMI coupler at any longitudinal point z can be expressed as

$$T(x,z) = \sum_{\nu} a_\nu \hat{F}_\nu(x) \exp(-j\beta_\nu z), \tag{2.21}$$

where β_ν is the propagation constant of the ν-th mode. The transition at the output plane of the MMI coupler is handled in a similar fashion to the input plane transition, and the power coupled into the output access guides can be found.

Modal propagation analysis is simpler than various numerical beam propagation methods (BPM). However, modal analysis is applicable only to structures (like MMI couplers) that can be adequately represented by a few longitudinally invariant sections, each supporting a relatively small number of guided modes, to keep the required computations at a practical level. Modal propagation analysis is probably the most effective theoretical tool to describe the self-imaging effect in MMI couplers. It not only supplies the basis for modeling and design, but it also provides insight into the operation of MMI couplers.

2.3 General Self-Imaging Properties in $N \times N$ Multimode Interference Couplers

Self-imaging is a property of homogeneous multimode waveguides by which an input field is reproduced in single or multiple images at periodic intervals along the propagation direction of the guide. This property has been used to design MMI couplers suitable for power splitting/combining applications. Several self-imaging mechanisms in MMI couplers have been described in the literature. The most general type of MMI coupler is the $N \times N$ coupler. Other variations of MMI couplers, such as the 3-dB coupler, cross coupler, and overlapping-image couplers can be considered as special cases of $N \times N$ MMI couplers. A layout of a practical $N \times N$ MMI coupler designed in a ridge waveguide system is shown in Figure 2.5. A field distribution at any of the N inputs is reproduced at the output plane of the coupler in the form of N images that have equal magnitudes and different phases. We are going to follow the general treatment of Bachmann *et al.* [9] to theoretically derive the complete self-imaging properties, which leads to compact expressions for the positions, intensities, and phases of the images. An arbitrary input light distribution is decomposed into the guided modes of the MMI section, which are propagated down the length of the coupler and superimposed at the output. The resulting equation for the field at the output plane is analytically transformed to describe the output field as a superposition of N images. In many applications, like generalized Mach–Zehnder switches and MMI-phasar multiplexers, not only the magnitudes but also the phases of the output images of the MMI couplers are relevant. Derivation of closed-form expressions for the phases give us the tools to design these relatively complex devices.

An $N \times N$ MMI coupler generally has a length of $L_c = 3L_\pi M / N$, where L_π is the beat length of the coupler and M is a positive integer such that M and N are without a common divisor. M is just a multiple occurrence of the N images at different device lengths. For practical applications, the device length has to be as short as possible; this is achieved by choosing $M=1$. Consequently, the length of the $N \times N$ MMI coupler considered in this analysis is

$$L_c = 3L_\pi / N. \tag{2.22}$$

The theory developed here is strictly correct only in the limit of strong guiding. This should not be a problem since MMI couplers are normally implemented in ridge waveguides, which are known to be "strongly guiding" or "strongly confining" as the large ridge depth tends to strongly confine the modal field within the bounds of the ridge. Using the effective index method described in Section 2.1.1, the three-dimensional coupler of Figure 2.5 is reduced to two dimensions as shown in Figure 2.6. The MMI coupler has an effective width W_e, which is slightly larger than its actual width and takes into account the lateral penetration depth of the modal fields. An expression for the effective width was given before in (2.15). In a strongly confining structure, the field distribution of the guided modes of the MMI coupler are well described by functions of the form

$$F_v(x) = \sin\left[\pi(v+1)x/W_e\right], \tag{2.23}$$

where v is the mode number. Note that, as illustrated in Figure 2.6, the x-axis has been placed such that the effective width of the coupler extends from $x=0$ to $x=W_e$. The modes are almost completely confined so that their field distributions contain an integer

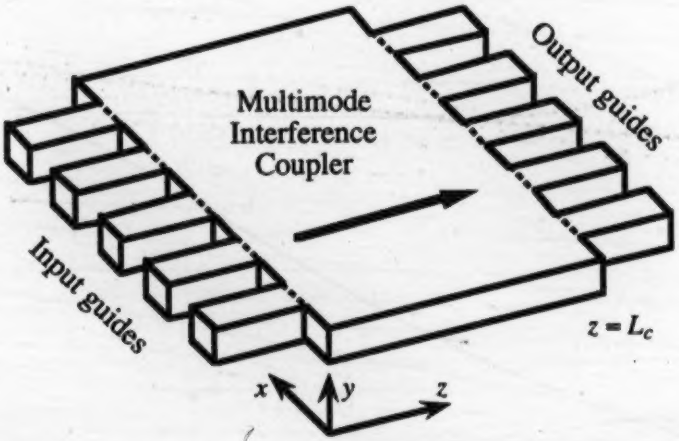

Figure 2.5 Schematic view of a practical $N \times N$ MMI coupler implemented in a ridge waveguide system (the case of $N = 5$ is shown).

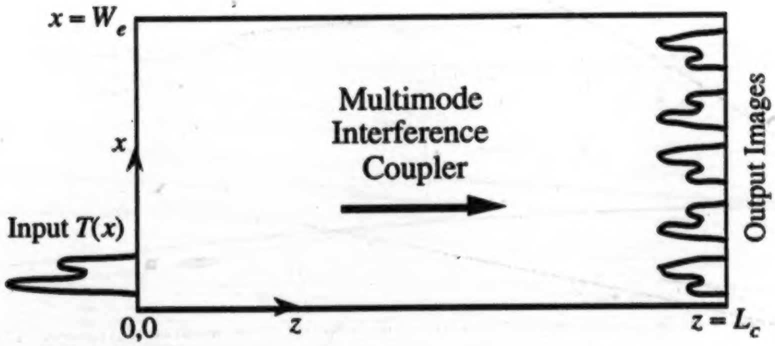

Figure 2.6 Any input field to a general MMI coupler of length $L_c = 3L_\pi/N$ is recreated in the form of N images at the output plane of the coupler. These output images have equal power and different phases.

number of half-periods within the waveguide. Now, by comparing (2.23) and (2.11), it is seen that the mode parameter p_v can be written as

$$p_v = \pi(v+1)/W_e. \tag{2.24}$$

But we know from (2.9) that the corresponding propagation constants are given by

$$\beta_v^2 = K^2 n_g^2 - p_v^2, \tag{2.25}$$

where n_g is, as described in Section 2.1.1, the effective index of the core layer of the equivalent slab, and K is the wave number in free space expressed by

$$K = 2\pi/\lambda, \tag{2.26}$$

where λ is the wavelength in free space. Using the paraxial approximation $p_v << \beta_v$ in (2.25), β_v can be approximated as

$$\beta_v \cong Kn_g - \frac{p_v^2}{2Kn_g}. \tag{2.27}$$

By substituting for K and p_v from (2.26) and (2.24), respectively, in (2.27) we obtain

$$\beta_v \cong \frac{2\pi n_g}{\lambda} - \frac{\pi\lambda(v+1)^2}{4n_g W_e^2}. \tag{2.28}$$

Using (2.28), the beat length L_π defined previously in (2.17) can be written as

$$L_\pi = \frac{\pi}{\beta_0 - \beta_1} \cong \frac{4 n_g W_e^2}{3\lambda}. \tag{2.29}$$

Using (2.28) and (2.29) the propagation constant of the ν-th mode β_ν can be expressed in terms of the propagation constant of the fundamental mode β_0 and the beat length as follows:

$$\beta_\nu \cong \beta_0 - \frac{\nu(\nu+2)\pi}{3L_\pi}. \tag{2.30}$$

From (2.30) it is observed that the propagation constant is a quadratic function of the mode number ν; this dependence establishes a definite phase relationship among all the modes of a homogeneous multimode waveguide and is the basis of resonant self-imaging.

Now, let us assume an arbitrary input field distribution at the entrance of the coupler. Although the access guides usually carry only one single, symmetrical mode, the analysis of this section applies to any arbitrary input field and can cover the situations where curved access guides are used or when the access guides may carry more than one mode. The input field is decomposed into the modes of the MMI coupler. For complete decomposition, in general we need an infinite number of guided modes (limit of strong guiding approximation). For the practical cases with a finite number of modes, the input field is decomposed into these modes, and the remaining field components are lost through radiation. However, the lost power is negligible for the strongly confining structures. Figure 2.7 shows the input light distribution $T(x)$ and the modal fields $F_\nu(x)$ of the coupler. For mathematical simplicity, the input field $T(x)$ defined in the real MMI section $0 < x < W_e$ has been extended to the virtual section $-W_e < x < 0$, forming the antisymmetrical function $T(x) - T(-x)$. This function is extended over the entire x-axis with $2W_e$ periodicity and named $T_{ext}(x)$. Using a spatial Fourier decomposition, $T_{ext}(x)$ can be rewritten as a superposition of the infinite number of modal fields:

$$T_{ext}(x) = \sum_{\nu=0}^{\infty} \alpha_\nu F_\nu(x), \tag{2.31}$$

where α_ν is a complex amplitude coefficient given by

$$\alpha_\nu = \frac{2}{W_e} \int_0^{W_e} F_\nu^*(x) T(x) dx. \tag{2.32}$$

Note that the functions $T(x)$ and $T_{ext}(x)$ are identical in the actual MMI coupler between $0 < x < W_e$, where the real physical problem is defined. The excited modes propagate over the length L_c of the MMI coupler and the output field $T_{out}(x)$ at the end of the coupler can be expressed as

$$T_{out}(x) = \sum_{\nu=0}^{\infty} \alpha_\nu F_\nu(x) \exp(-j\beta_\nu L_c). \tag{2.33}$$

Substituting for β_ν and L_c from (2.30) and (2.22), respectively, in (2.33) we get

$$T_{out}(x) = \sum_{\nu=0}^{\infty} \alpha_\nu P_\nu F_\nu(x), \tag{2.34}$$

where the parameter P_ν is given by

$$P_\nu = \exp\left[-j\beta_0 L_c + \frac{j\pi}{N}\nu(\nu+2)\right]. \tag{2.35}$$

The parameter P_ν has a physical meaning as it accounts for the phase change of the ν-th mode. P_ν can be calculated recursively, which is needed for the derivation of the self-imaging properties:

$$P_0 = \exp(-j\beta_0 L_c), \qquad P_\nu = P_{\nu-1} \exp[j\pi(2\nu+1)/N]. \tag{2.36}$$

In the above analysis the output light distribution of the MMI coupler has been represented as the superposition of the modal fields. The occurrence of multiple images

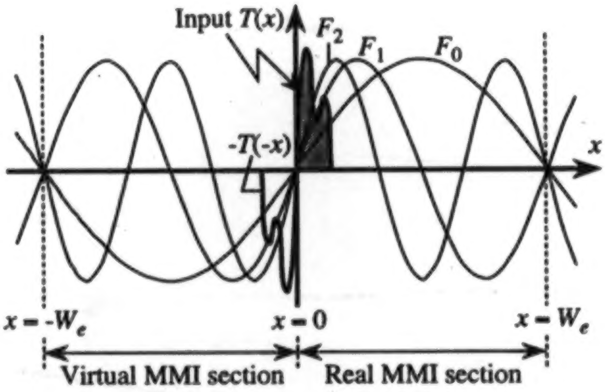

Figure 2.7 MMI section with input light distribution $T(x)$ and decomposition into the bound modes $F_\nu(x)$ of the structure. For theoretical purposes the functions $F_\nu(x)$ and $T(x)$ are antisymmetrically extended to the virtual MMI section and periodically repeated on the whole x axis.

is not obvious in this form. The positions, phases, and amplitudes of multiple images cannot easily be extracted from Equation (2.34). We have to find a way of rewriting (2.34) so as to see the multiple images of the input field in the equation. This will be done next.

2.3.1 From Modal Representation to Self-Images

Let us first reformulate the parameter P_v. A new parameter Q_v, which will be shown to be identical to P_v, is introduced and defined as follows:

$$Q_v = \frac{1}{C}\sum_{b=0}^{N-1}\exp\left(j\Omega_{v,b}\right), \tag{2.37}$$

where C is a complex normalization constant defined as

$$C = \exp\left(j\beta_0 L_c\right)\sum_{b=0}^{N-1}\exp\left(\frac{-j\pi x_b}{W_e} + j\varphi_b\right), \tag{2.38}$$

and Ω is a phase coefficient defined as

$$\Omega_{v,b} = -\pi\left(v+1\right)\frac{x_b}{W_e} + \varphi_b, \tag{2.39}$$

where x_b and φ_b are

$$x_b = \left(2b - N\right)W_e/N, \tag{2.40}$$

$$\varphi_b = b\left(N - b\right)\pi/N. \tag{2.41}$$

It will become clear later that x_b and φ_b represent the positions and phases, respectively, of the N images numbered by $b = 0, 1, \ldots, N-1$. Note that the phase coefficient $\Omega_{v,b}$ has a periodicity of N with respect to b. Using (2.39) with (2.40) and (2.41), and comparing $\Omega_{v-1,b}$ and $\Omega_{v,b-1}$ we obtain

$$\Omega_{v,b-1} = \Omega_{v-1,b} + \frac{\pi}{N}\left(2v+1\right). \tag{2.42}$$

Equation (2.42) is important in the derivation, although this is not yet very obvious. Now, the term with index b in (2.37) is replaced by $b-1$, and employing (2.42) and the N periodicity of the $\Omega_{v,b}$, the following relation between Q_v and Q_{v-1} is obtained:

$$Q_v = Q_{v-1}\exp\left[j\pi\left(2v+1\right)/N\right]. \tag{2.43}$$

Given the fact that (2.43) is the same as that obtained for P_v in (2.36), the identity $P_v = Q_v$ is proved if we show that $P_0 = Q_0$. By substituting for $v = 0$ and by appropriate insertions from (2.38) and (2.39) in (2.37), it is easily confirmed that $P_0 = Q_0$. Thus, we can conclude that $P_v = Q_v$ or

$$P_v = \frac{1}{C}\sum_{b=0}^{N-1}\exp\left[-j\pi(v+1)\frac{x_b}{W_e} + j\varphi_b\right]. \tag{2.44}$$

It is easy to show that $-\pi x_{-b}/W_e = \pi x_b/W_e + 2\pi$ from (2.40), and $\varphi_{-b} = \varphi_b - 2\pi$ from (2.41). We now replace the summation index b with $N-b$ in (2.44). Then using the N periodicity, and by replacing $-x_{-b}$ and φ_{-b} with x_b and φ_b, respectively, we obtain

$$P_v = \frac{1}{C}\sum_{b=0}^{N-1}\exp\left[j\pi(v+1)\frac{x_b}{W_e} + j\varphi_b\right]. \tag{2.45}$$

Equations (2.44) and (2.45) both yield expressions for P_v that differ only in the sign of the exponential terms. These new forms of P_v are inserted into Equation (2.34). Let us first examine the term $P_vF_v(x)$. The explicit form of $F_v(x)$ given by (2.23) is replaced with the exponential functions using the identity $\sin(x) = [\exp(jx) - \exp(-jx)]/(2j)$. We obtain

$$P_vF_v(x) = \frac{1}{2j}\left\{P_v\exp\left[j\pi(v+1)x/W_e\right] - P_v\exp\left[-j\pi(v+1)x/W_e\right]\right\}. \tag{2.46}$$

The two occurrences of P_v in (2.46) are inserted with Equations (2.44) and (2.45), respectively. This permits the introduction of the shifted modal fields $F_v(x - x_b)$ and results in a compact form:

$$P_vF_v(x) = \frac{1}{C}\sum_{b=0}^{N-1}\frac{1}{2j}\left\{\begin{matrix}\exp\left[j\pi(v+1)(x-x_b)/W_e\right] - \\ \exp\left[-j\pi(v+1)(x-x_b)/W_e\right]\end{matrix}\right\}\exp(j\varphi_b), \tag{2.47}$$

$$P_vF_v(x) = \frac{1}{C}\sum_{b=0}^{N-1}F_v(x-x_b)\exp(j\varphi_b). \tag{2.48}$$

This compact form of $P_vF_v(x)$ is inserted into (2.34). After interchanging the two sums we obtain

$$T_{\text{out}}(x) = \frac{1}{C}\sum_{b=0}^{N-1}\left[\sum_{v=0}^{\infty}\alpha_vF_v(x-x_b)\right]\exp(j\varphi_b). \tag{2.49}$$

The term inside the brackets of (2.49) is, by comparing to (2.31), the Fourier expansion of $T_{\text{ext}}(x - x_b)$. Therefore, we finally arrive at the desired form of the output function that is a superposition of N images of the input field:

$$T_{\text{out}}(x) = \frac{1}{C}\sum_{b=0}^{N-1}T_{\text{ext}}(x-x_b)\exp(j\varphi_b). \tag{2.50}$$

Equation (2.50) shows that the input field is repeated N times at the output of the MMI coupler. As we said before, x_b and φ_b represent the positions and phases of the images. Also, due to the principle of conservation of energy, we have $|C| = \sqrt{N}$.

An MMI coupler of length $L_c = 3L_\pi/N$ produces N-fold images of the extended input function $T_{ext}(x)$ at its output. As shown in Figure 2.8, the N-fold images of the extended input function are numbered with b. These images correspond to $2N$ images of the real input function $T(x)$ in the range $-W_e < x < W_e$. Half of the images are phase-inverted. The real MMI section $0 < x < W_e$ includes N images of $T(x)$, again half are phase-inverted. Remember that the physical problem is defined in the real MMI section only, and the terms with contributions to this limited range must be taken into account for the calculation of $T_{out}(x)$. Also, note that the phases φ_b are not included in the simple drawing of Figure 2.8. The possible positions of the images and their corresponding orientations are found from Equation (2.40) and Figure 2.8.

Access guides, which are placed at the input/output of practical MMI couplers, restrict the exciting and collecting light distributions to limited ranges. The $N \times N$ MMI coupler is designed such that different images of the input field at the output do not overlap. For properly positioned access guides, the self-images are smoothly coupled

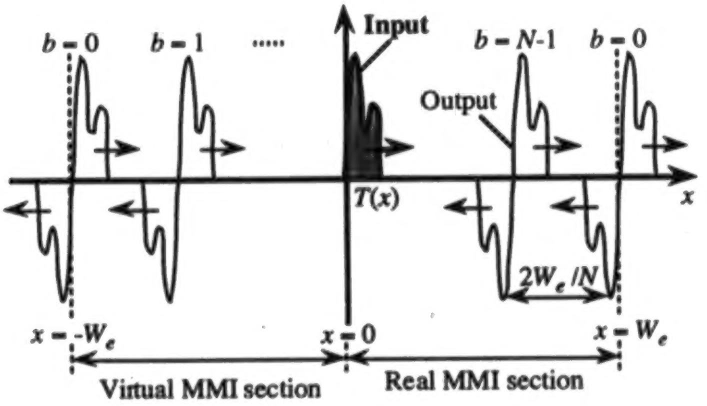

Figure 2.8 MMI section with length $L_c = 3L_\pi/N$ produces N images of the extended input field $T_{ext}(x)$. The real MMI section of effective width W_e contains N images of the real input $T(x)$ at the output of the MMI. Half of the images are phase-inverted.

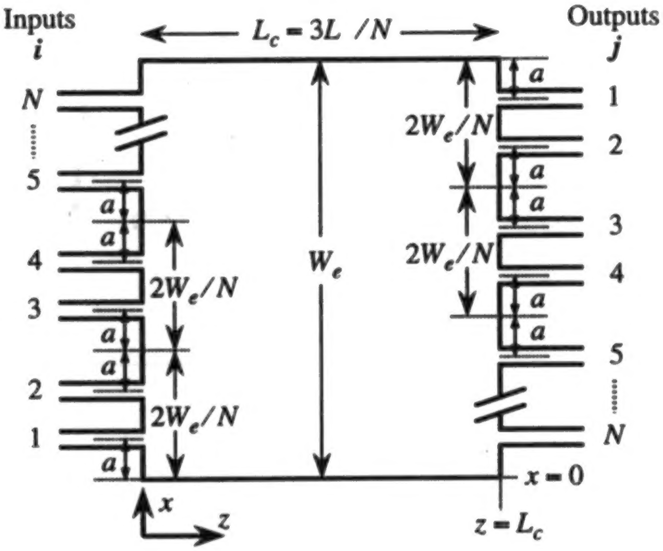

Figure 2.9 Schematic diagram of a general $N \times N$ MMI coupler. Input and output positions have a free parameter a, which is limited to $0 \le a \le W_e/N$.

into the output guides with minimal loss. An $N \times N$ MMI coupler has N input ports and N output ports. Each input position corresponds to the same set of output image positions but the images have different phases. A schematic diagram of the $N \times N$ MMI coupler is depicted in Figure 2.9. For a given effective width W_e and a chosen number of images N, we obtain an additional free parameter a for the input/output positions that is limited to $0 \le a \le W_e/N$. As the value of the parameter a increases, the images shift along the arrows shown in Figure 2.8. Normally it is desired that the access guides be equally spaced. By setting a to $a = W_e/(2N)$, equal spacing between the access guides is obtained. As shown in Figure 2.9, the input ports and the output ports of the coupler are denoted with indices i and j, respectively. The numbering direction of the inputs is bottom up while the numbering direction of the outputs is top down. Note that the index j should not be confused with the imaginary unity $j = \sqrt{-1}$.

Other variations of MMI couplers like 3-dB couplers and cross couplers are just special cases of the general $N \times N$ MMI coupler. For 3-dB couplers $N = 2$ and $L_c = 3L_\pi/2$, while for cross couplers $N = 1$ and $L_c = 3L_\pi$. In cross couplers, the input field and its single image are placed at laterally opposite positions. This image is a mirroring of the input field with respect to the longitudinal axis along the center of the coupler. Also, it is easy to see that an MMI coupler with a length of $6L_\pi$ produces a direct image of the input field at its output (i.e., bar coupling) since it can be considered as a concatenation of two cross couplers. Thus, MMI couplers have the interesting property that they are in bar and cross-coupled states at lengths equal to even and odd multiples of $3L_\pi$, respectively. This property will be used in the design of a 980/1550-nm wavelength demultiplexing coupler in Chapter 5.

2.3.2 Derivation of the Phases

In an $N \times N$ MMI coupler an input field is reproduced at the output plane of the coupler in the form of N discrete images of equal intensity and different phases. There is a phase $\varphi_{i,j}$ associated with imaging input i to output j. This relative phase can now be given in a compact form (remember the definition of the phase $\varphi = \omega t - Kz$). To find the phase $\varphi_{i,j}$, we have to find the correct value of b in Equation (2.41). This is done by comparing Figure 2.8 with Figure 2.9. Care must be taken to include the minus sign or an additional phase π for inverted images, which occur for $i + j$ even. To give an example, we choose input $i = 1$. Then the corresponding values of b for the output ports j are:

$$b = \begin{cases} N - (j-1)/2 & \text{for } j \text{ odd}, \\ N - j/2 & \text{for } j \text{ even}. \end{cases} \tag{2.51}$$

Now, let us look at the general input port i as shifted from input $i = 1$ by $i - 1$. The b values stay the same if the outputs j are also shifted. Odd and even outputs shift in opposite directions to each other. The correct shift of the outputs for general b is $i - 1$ for odd j, and $1 - i$ for even j. Allowing for the correctly shifted versions of j in (2.51), we obtain

$$b = \begin{cases} N - (j-i)/2 & \text{for } j \text{ odd or } i+j \text{ even}, \\ N - (j+i-1)/2 & \text{for } j \text{ even or } i+j \text{ odd}. \end{cases} \tag{2.52}$$

The b values from (2.52) are inserted in (2.41) to get

$$\varphi_{i,j} = \begin{cases} \phi_0 + \pi + \dfrac{\pi}{4N}(j-i)(2N-j+i) & \text{for } i+j \text{ even}, \\ \phi_0 + \dfrac{\pi}{4N}(j+i-1)(2N-j-i+1) & \text{for } i+j \text{ odd}. \end{cases} \tag{2.53}$$

Note the inclusion of the additional phase π for the case of $i+j$ even. The phase associated with the complex constant $1/C$ in (2.50) has been taken into account in (2.53) by ϕ_0. Using the reciprocity law for generalized quadratic Gaussian sums [60], it can be shown that the constant C given by (2.38) can be rewritten as

$$C = \sqrt{N}\exp\left[j\beta_0 L_c + \frac{j\pi}{N} + \frac{j\pi}{4}(N-1)\right]. \tag{2.54}$$

The phase constant ϕ_0 is simply equal to the argument of $1/C$, i.e.,

$$\phi_0 = -\beta_0\frac{3L_\pi}{N} - \frac{\pi}{N} - \frac{\pi}{4}(N-1). \tag{2.55}$$

It should be noted that the relative values, and not the absolute terms, of the phases $\varphi_{i,j}$ are of significance for applications in MMI-phasar multiplexers or generalized Mach–Zehnder switches. Hence, the phase constant ϕ_0 is simply ignored in our analysis in the following chapters of this thesis.

The phase expression of (2.53) is in the same format presented in [9]. Let us try to further simplify this phase expression. By expanding and regrouping its terms, Equation (2.53) can be rewritten as

$$\varphi_{i,j} = \begin{cases} \phi_0 + \frac{\pi}{2}(j-i+2) - \frac{\pi}{4N}(j-i)^2 & \text{for } i+j \text{ even}, \\ \phi_0 + \frac{\pi}{2}(j+i-1) - \frac{\pi}{4N}(j+i-1)^2 & \text{for } i+j \text{ odd}. \end{cases} \tag{2.56}$$

By inspection we can easily see that, (2.56) is equivalent to the following single relation:

$$\varphi_{i,j} = \phi_0 + \frac{\pi}{2}\left[j + \frac{1}{2} + (-1)^{i+j}\left(\frac{3}{2} - i\right)\right] - \frac{\pi}{4N}\left[j - \frac{1}{2} + (-1)^{i+j}\left(\frac{1}{2} - i\right)\right]^2. \tag{2.57}$$

Figure 2.10 depicts an $N \times N$ MMI coupler, in which the output ports have been numbered in the same way as the input ports. It will be seen in Chapter 4 that this numbering convention will facilitate the analysis of MMI-phasar multiplexers. By replacing j with $N+1-j$ the phase relation $\varphi_{i,j}$ can be modified to accommodate our newly adopted numbering convention of Figure 2.10. By performing this replacement in (2.57) and after some manipulations, we arrive at the final form of the phase relation:

$$\varphi_{i,j} = \phi_1 - \frac{\pi}{2}(-1)^{i+j+N} + \frac{\pi}{4N}\left[i + j - i^2 - j^2 + (-1)^{i+j+N}\left(2ij - i - j + \frac{1}{2}\right)\right], \tag{2.58}$$

where ϕ_1 is a constant phase given by

$$\phi_1 = -\beta_0 \frac{3L_\pi}{N} - \frac{9\pi}{8N} + \frac{3\pi}{4}. \tag{2.59}$$

Equation (2.58) will be used in the analysis of MMI-phasar multiplexers in Chapter 4. It is easily confirmed from (2.58) that the symmetry relation $\varphi_{i,j} = \varphi_{j,i}$ holds true for an $N \times N$ MMI coupler. Also, another symmetry relation $\varphi_{i,j} = \varphi_{N+1-i,N+1-j}$ can be derived by replacing i by $N + 1 - i$ and j by $N + 1 - j$ in (2.58) and utilizing the 2π periodicity of $\varphi_{i,j}$. These symmetry relations are useful in the analysis of MMI-phasar multiplexers.

The access guides in practical $N \times N$ MMI couplers are placed at equally spaced positions. In this case, as illustrated in Figure 2.10, the lateral positions of input and output ports of the coupler are

$$x_i^{\text{in}} = (2i-1)W_e/2N, \quad \text{and} \quad x_j^{\text{out}} = (2j-1)W_e/2N. \tag{2.60}$$

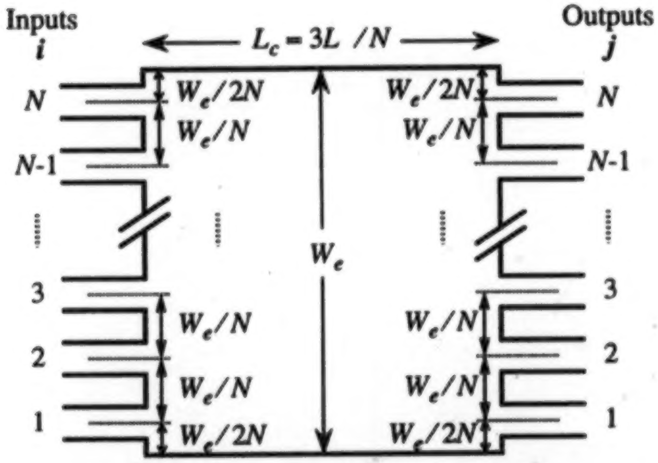

Figure 2.10 An $N \times N$ MMI coupler with equally spaced access guides. The same numbering direction has been used for both input and output guides.

2.4 Overlapping-Image Multimode Interference Couplers

As was mentioned in Section 2.3.1, the positions of the input/output ports of the general MMI couplers have a free parameter a. Considering an MMI coupler of length $3L_\pi/N'$, if we set a at one of its limits (i.e., $a = 0$ or $a = W_e/N'$), then N' previously distinct self-images merge in pairs and a reduced number of images is obtained. Each output field is found by calculating the interference between two overlapped images, and the output intensity distribution may be uniform or nonuniform depending on the position of the input excitation. A thorough theoretical treatment of these MMI devices, which are referred to as overlapping-image MMI couplers, has been presented in [10]. Some of the main aspects of these couplers are reviewed in this section.

In Figure 2.8 it was seen that shifting the input field $T(x)$ along the x-axis (or in other words increasing the value of the parameter a) moves the upright images in the same direction and the phase-inverted images in the opposite direction. Upright and phase-inverted images cross when the parameter a is at one of its limits. Complete interference occurs for either purely symmetric or purely antisymmetric input field distributions; both of these cases have been dealt with in [10]. Here we concern ourselves only with the symmetrical input field distributions as this is often the case for practical MMI couplers with single-mode access guides. Now, for two interfering images of equal intensity $1/N'$ and with known phases φ_1 and φ_2, the magnitude r and the phase Φ of the resulting image are derived from the addition of the complex amplitudes:

$$r\exp(j\Phi) = \frac{1}{\sqrt{N'}}\exp(j\varphi_1) + \frac{1}{\sqrt{N'}}\exp(j\varphi_2). \tag{2.61}$$

Rewriting (2.61):

$$r\exp(j\Phi) = \frac{2}{\sqrt{N'}}\cos[(\varphi_1 - \varphi_2)/2]\exp[j(\varphi_1 + \varphi_2)/2]. \tag{2.62}$$

The intensity r^2 of the resulting image is

$$r^2 = \frac{4}{N'}\cos^2[(\varphi_1 - \varphi_2)/2], \tag{2.63}$$

and the phase Φ is

$$\Phi = \begin{cases} (\varphi_1 + \varphi_2)/2 & \text{for } \cos[(\varphi_1 + \varphi_2)/2] > 0, \\ \pi + (\varphi_1 + \varphi_2)/2 & \text{for } \cos[(\varphi_1 + \varphi_2)/2] < 0. \end{cases} \tag{2.64}$$

The general Equations (2.63) and (2.64) for interfering two equally intense images can be applied to the interference taking place at the output of the overlapping-image MMI couplers. In a manner similar to what was described in the previous section, the correct value of b has to be inserted in Equation (2.41) to find the phases φ_1 and φ_2 as a function of the input/output port numbers. Then Equations (2.63) and (2.64) can be expressed in terms of the input/output port numbers by substituting for φ_1 and φ_2. Following this procedure it can be shown [10] that the intensity $r'^2_{i',j'}$ and the phase $\varphi'_{i',j'}$ of output j' resulting from a symmetric field excitation at input i' of the overlapping-image MMI coupler depicted in Figure 2.11(a) can be expressed as

$$r'^2_{i',j'} = \frac{4}{N'}\sin^2\left[(N'-j')i'\frac{\pi}{2N'}\right], \tag{2.65}$$

$$\varphi'_{i',j'} = \begin{cases} \phi'_0 - (i'^2 + j'^2)\dfrac{\pi}{4N'} + (j'+1)\dfrac{\pi}{2} & \text{for } \sin\left[(N'-j')i'\dfrac{\pi}{2N'}\right] > 0, \\ \phi'_0 - (i'^2 + j'^2)\dfrac{\pi}{4N'} + (j'+3)\dfrac{\pi}{2} & \text{for } \sin\left[(N'-j')i'\dfrac{\pi}{2N'}\right] < 0, \end{cases} \tag{2.66}$$

where i' and j' are any integer from 1 to $N'-1$, and $i'+j'$ must be even. Again ϕ'_0 is a constant phase given by

$$\phi'_0 = -\beta_0\frac{3L_\pi}{N'} - \frac{\pi}{N'} - \frac{\pi}{4}(N'-1). \tag{2.67}$$

Note that image overlapping occurs only at outputs j' with even $i'+j'$ while the remaining outputs are of no significance since they carry no power. We can simplify (2.66) and write it as a single-line expression:

$$\varphi'_{i',j'} = \phi'_0 - \frac{\pi}{4N'}(i'^2 + j'^2) + \frac{\pi}{2}(j'+2) - \frac{\pi}{2}\operatorname{sgn}\left(\sin\left((N'-j')i'\frac{\pi}{2N'}\right)\right), \tag{2.68}$$

where sgn(x) is defined as

$$\operatorname{sgn}(x) = \begin{cases} +1 & \text{if } x > 0, \\ -1 & \text{if } x < 0. \end{cases} \tag{2.69}$$

Let us reverse the numbering direction of the output ports so that they are numbered in the same way as that of the input ports; see Figure 2.11(b). This modified numbering convention can be accommodated by replacing j' with $N-j'$ in (2.65) and (2.68) to get

$$r'^2_{i',j'} = \frac{4}{N'}\sin^2\left(i'j'\frac{\pi}{2N'}\right), \tag{2.70}$$

$$\varphi'_{i',j'} = \phi'_0 + \frac{\pi N'}{4} + \pi - \frac{\pi}{4N'}(i'^2 + j'^2) - \frac{\pi}{2}\operatorname{sgn}\left(\sin\left((i'j')\frac{\pi}{2N'}\right)\right), \tag{2.71}$$

where i' and j' are any integer from 1 to $N-1$, and $i'+j'+N'$ must be even. Interesting symmetry relations $r'^2_{i',j'} = r'^2_{j',i'}$ and $\varphi'_{i',j'} = \varphi'_{j',i'}$ are easily derived from (2.70) and (2.71), respectively. The positions of inputs and outputs of the MMI coupler of Figure 2.11(b) are given by

$$x_{i'}^{in} = i'W_e/N', \tag{2.72}$$

$$x_{j'}^{out} = j'W_e/N', \quad \text{with even } i'+j'+N'. \tag{2.73}$$

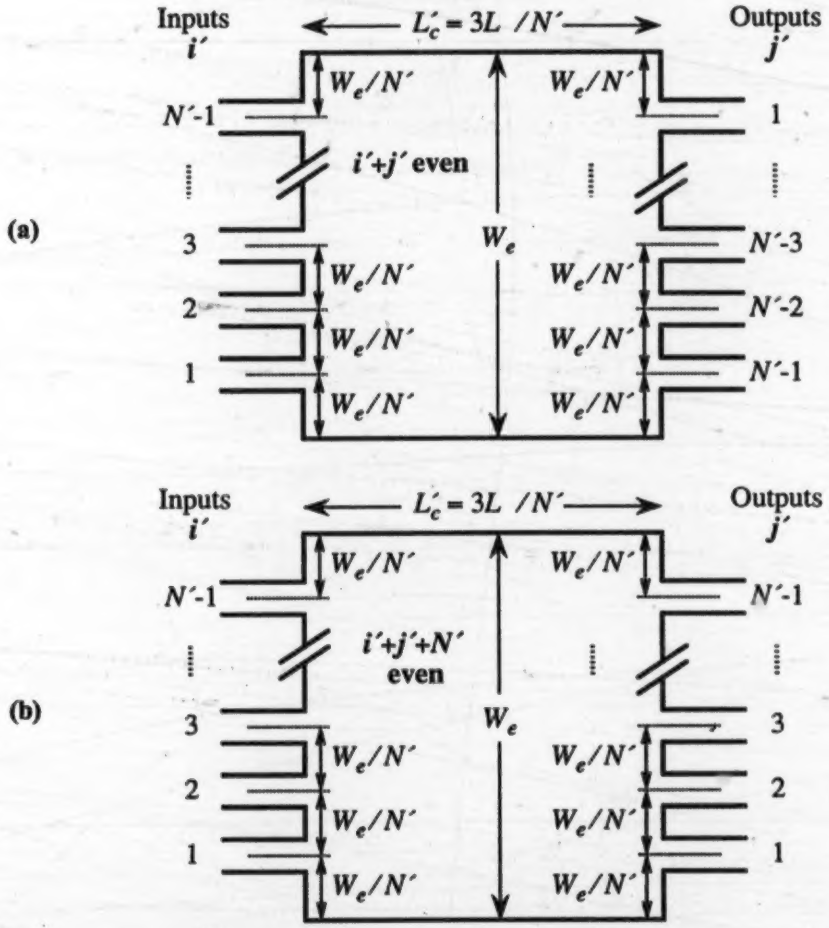
(a)
Inputs
i′
$L_c' = 3L\ /N'$
Outputs
j′
N′-1
3
2
1
W_e/N'
i′+j′ even
W_e
1
N′-3
N′-2
N′-1
(b)
Inputs
i′
$L_c' = 3L\ /N'$
Outputs
j′
N′-1
3
2
1
W_e/N'
i′+j′+N′ even
W_e
N′-1
3
2
1

Figure 2.11 Overlapping-image MMI coupler with a reduced number of images. There is a pair of overlapped images at every other output position. (a) Outputs have been numbered in the opposite direction to that of inputs. (b) The same numbering direction has been used for both inputs and outputs.

Our interest in the overlapping-image MMI couplers is mainly due to the fact that we use these couplers as 1 × N nonuniform power splitters in the design of MMI-phasar multiplexers, as will be explained in Chapter 4. A 1 × N MMI nonuniform power splitter is an overlapping-image MMI coupler with one input port and a reduced number of images N. The overlapping-image MMI coupler of Figure 2.11(b) can be directly translated to the 1 × N MMI power splitter depicted in Figure 2.12 by introducing parameters h_1 and h_2 where $h_1 = i'$ and $h_2 = j' - 2(j-1)$. Index j denotes the numbering of outputs of the 1 × N MMI power splitter. The restrictions on the values of N', i', and j' can be rewritten in terms of parameters h_1 and h_2 as follows:

$$\begin{aligned} h_1 &= 1,\ \ldots,\ N'-1; \\ h_2 &= 1, 2; \\ N' &= 2N + h_2, 2N + h_2 - 1; \end{aligned} \tag{2.74}$$

and $h_1 + h_2 + N'$ must be even. Parameters N', h_1, and h_2 control the coupler length, positions of access guides and, most importantly, output power distribution. The length of the 1 × N power splitter is

$$L_c' = 3L_\pi / N', \tag{2.75}$$

where L_π is as defined before. Now, by replacing i' with h_1 and j' with $h_2 + 2(j-1)$ in Equations (2.70)–(2.73), the corresponding expressions for intensities, phases, and input/output positions of the 1 × N power splitter are obtained. Intensities and phases of the resultant outputs in the 1 × N MMI power splitter can be written as

$$r_j'^{\,2} = \frac{4}{N'} \sin^2\left[\left(\frac{h_2}{2} + j - 1\right) h_1 \frac{\pi}{N'}\right], \tag{2.76}$$

$$\varphi_j' = \phi_1' - \frac{\pi}{N'}\left[\frac{h_1^2 + h_2^2}{4} + (j-1)^2 + h_2(j-1)\right] - \frac{\pi}{2}\operatorname{sgn}\left(\sin\left[\left(\frac{h_2}{2} + j - 1\right) h_1 \frac{\pi}{N'}\right]\right), \tag{2.77}$$

where ϕ_1' is a constant phase given by

$$\phi_1' = \beta_0 \frac{3L_\pi}{N'} - \frac{\pi}{N'} + \frac{5\pi}{4}. \tag{2.78}$$

The input and output positions are

$$x^{\text{in}} = h_1 W_e / N', \tag{2.79}$$

$$x_j^{\text{out}} = (2j - 2 + h_2) W_e / N', \tag{2.80}$$

where h_1 is an integer given by (2.74), and h_2 is either 1 or 2.

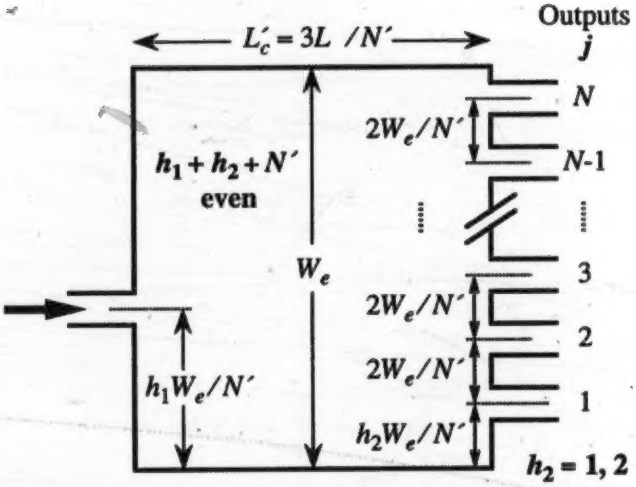

Figure 2.12 Schematic diagram of a $1 \times N$ MMI power splitter where parameters h_2 and N' have to be chosen from $h_2 = 1, 2$ and $N' = 2N + h_2$, $2N + h_2 - 1$ such that the term $h_1 + h_2 + N'$ is even. Depending on the position of the input guide, both equal and unequal power splitting is possible. All the values of h_1 except $N'/2$, $N'/3$, and $2N'/3$ result in nonuniform power distributions.

It is demonstrated in [10], and also it can be verified from (2.76), that output power distribution of the $1 \times N$ MMI power splitter is uniform only when h_1 has one of the three values of $N'/2$, $N'/3$, and $2N'/3$; power distribution is nonuniform for all the other values of h_1. In this thesis, we are not interested in the overlapping-image MMI couplers with uniform output power distributions. However, for the sake of completeness, a brief overview of these couplers is given next.

2.4.1 Uniform Power Splitters

The overlapping-image MMI couplers having uniform output power distributions are referred to as restricted interference MMI couplers since the input guides of these couplers are positioned such that only a restricted set of guided modes are excited. This selective modal excitation allows new interference mechanisms with shorter device lengths. These couplers have been divided into two groups: symmetric interference and paired interference [23]. In the case of the symmetric interference MMI coupler, the input guide is positioned at $W_e/2$. With this input position, only the even symmetric modes of the coupler are excited. It can be shown [10] that the length of the symmetric interference coupler producing N outputs with uniform intensities is then given by

$$L_c' = 3L_\pi/(4N), \tag{2.81}$$

which is four times shorter than the length of the $N \times N$ MMI coupler given by (2.22). In the case of the paired interference MMI coupler, the input guide is positioned at either $W_e/3$ or $2W_e/3$. With these two input positions, the modes with the mode number $\nu = 2, 5, 8, \ldots$ will not be excited. It can be shown [10] that the length of the paired interference coupler producing N outputs with uniform intensities is given by

$$L_c' = L_\pi/N, \tag{2.82}$$

which is three times shorter than the length of the $N \times N$ MMI coupler given by (2.22). Considering the fact that the restricted interference couplers are shorter than the $N \times N$ MMI couplers, in applications where $1 \times N$ uniform power splitters are required it would be advantageous to use the restricted interference couplers [15]. Table 2.1 summarizes the different possible types of MMI couplers that produce N outputs with uniform power.

Table 2.1 Summary of different multimode interference types that result in N outputs with uniform power.

Multimode interference mechanism	Coupler length	Conditions on the input position (x^{in})
General interference	$3L_\pi/N$	None
Restricted symmetric interference	$3L_\pi/(4N)$	$x^{\text{in}} = W_e/2$
Restricted paired interference	L_π/N	$x^{\text{in}} = W_e/3, 2W_e/3$

3. Performance of Multimode Interference Couplers

The theory of MMI couplers was described in the previous chapter, and the required tools for modeling the light propagation in MMI couplers were provided. To verify the theory, it is desired to fabricate a series of MMI couplers and compare their theoretical and experimental performances. Towards this end, a number of general 5 × 5 MMI couplers and overlapping-image 1 × 5 MMI nonuniform power splitters were designed and fabricated in a SiO_2–SiON deeply-etched rib waveguide system. In this chapter, the fabrication and testing procedure of the MMI couplers is described. The transmission of the couplers is examined. Also, fabrication tolerances and optical bandwidth of the MMI couplers are studied. The device fabrication was performed at the Alberta Microelectronic Centre (AMC), and the rest of the work, including the design and the device testing, was carried out at TRLabs.

3.1 Waveguide Structure and Device Fabrication

MMI couplers have been implemented in various materials [23] including III-V semiconductors and glass-on-silicon waveguide structures. Glass-based structures are generally cheaper and simpler to fabricate compared with structures based on III-V semiconductors. Glass waveguides formed on silicon wafers are also used in hybrid photonic integrated circuits. A glass layer structure, SiO_2–SiON, was used in the fabrication of our devices. These silica-based films were grown by the plasma enhanced chemical vapour deposition (PECVD) method. Silicon oxynitride (SiON) is a suitable material for passive optical components and has been used in a variety of applications [61]–[65]. The material SiO_2–SiON is compatible with the well-established silicon technology and offers the possibility of hybrid integration with III-V optoelectronic devices. The refractive index of SiON can be varied from that of SiO_2 ($n \approx 1.46$) to about that of Si_3N_4 ($n \approx 2.2$) by changing the ammonia flow rate during the film growth. Moreover, low loss optical SiON waveguides made by PECVD have been reported in the literature [62], [65].

The deeply-etched rib waveguide structure depicted in Figure 3.1 was employed in the fabrication of the MMI devices discussed in this thesis. The PECVD SiO_2–SiON films were deposited on a standard silicon wafer. A 1-μm-thick SiON layer was the waveguide core, and a 5-μm-thick silicon oxide (SiO_2) film was used as a buffer layer separating the core and the substrate. The optical parameters of the films were determined by broadband (250–1700 nm) ellipsometry, and the refractive indices were modeled using a six-term Cauchy relation [58]. The refractive indices of the SiON and the SiO_2 films at the 1550-nm wavelength were 1.561 and 1.46, respectively. The indices of the films had a typical variation of about ±0.003 over a 4-inch wafer. The thickness uniformity of the films was better than ±50 nm over a 4-inch wafer. The device pattern was transferred to the SiON film using a photoresist mask and CHF_3–CF_4 reactive ion etching (RIE) with an etch depth of 1 μm. As indicated by Equation (2.29), the optimal length of an MMI coupler is highly sensitive to variations of the coupler width. Tight control during photolithography was required to minimize the width variations. An accuracy of ±0.1 μm in the width of the fabricated waveguides, with respect to the dimensions of the photomask features, was repeatably achieved.

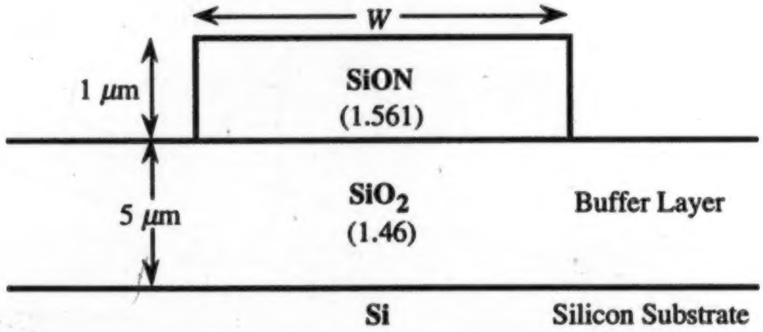

Figure 3.1 Cross-section of the SiO_2–SiON rib waveguide. The numbers inside the brackets indicate the refractive index values at 1550-nm wavelength.

Let us now describe, in more detail, the various steps involved in producing the SiO_2–SiON rib waveguides. These fabrication processes can be assembled into three groups: PECVD, photolithography, and RIE.

i) PECVD: In this process, vapour-phase reactants are delivered to the surface of a silicon substrate and react chemically to produce solid films of a desired composition. An

RF glow discharge plasma provides energy to activate the reaction. The chamber temperature and pressure, RF power, and gas flow rates can all affect the reaction and the physical and chemical characteristics of the resulting film. The process for depositing the SiON film used 29 Watts of RF power, and a chamber pressure and temperature of 1000 mTorr and 350 °C, respectively. The vapour constituents and their corresponding flow rates were as follows: silane (SiH_4) at 7.5 sccm, ammonia (NH_3) at 30 sccm, helium (He) at 700 sccm, nitrogen (N_2) at 100 sccm, nitrous oxide (N_2O) at 120 sccm. The flow rate parameter sccm refers to cubic centimeters per minute, at standard temperature and pressure. The ammonia flow rate determines the fractional incorporation of nitrogen in the SiON and, consequently, the refractive index of the films. Note that higher nitrogen levels in SiON increase the refractive index. The deposition duration for the 1-μm thick SiON layer was about 48 minutes. The SiO_2 film was produced with the following parameters: 7 sccm silane, 600 sccm helium, 100 sccm nitrogen, 800 sccm nitrous oxide, and the same RF power and temperature and pressure as those used in the SiON deposition. After depositing the films, the parameters such as the thickness and the refractive index of the films can be measured with an ellipsometer or a prism coupler.

ii) Photolithography: The basic steps involved in photolithography and RIE processes are shown in Figure 3.2. Before coating the wafers with photoresist, the wafers were primed with HMDS (hexamethylene disilazane) in an oven to improve the adhesion of the photoresist to the films. A positive photoresist (Shipley #504) was spun on at 500 rpm for 10 seconds followed by 6000 rpm for 30 seconds to obtain a photoresist layer with a thickness of 1.1 μm. The coated wafers were softbaked for one minute at 110 °C on a vacuum-applied hot plate. Then the wafers were placed in a mask aligner and were exposed to UV light for 1.6 seconds. An electron-beam-written chrome-on-quartz photomask was used. The exposed photoresist was developed with the Shipley 354 developer solution for 20 seconds. The expose time and the development duration were the critical parameters in accurately transferring the mask features to the photoresist, and it was required to fine tune these parameters to achieve the designed waveguide widths.

iii) Reactive Ion Etching (RIE): The remaining photoresist was hardened before etching by hardbaking the developed wafers for one minute at 120 °C on a vacuum-applied hot plate. The exposed film was etched down with an RIE process using 80% CHF_3 and 20% CF_4, at a total pressure of 40 mTorr and RF power of 100 Watts. The etch duration for the 1 μm SiON was about 27 minutes. The excess photoresist was removed using an acetone ultrasonic bath or/and with an oxygen plasma.

After completing the above fabrication processes, the devices were prepared for testing by cleaving the wafer at appropriate positions such that the access guides were perpendicular to the cleaved planes. Figure 3.3 illustrates a SEM (scanning electron microscope) picture showing the rib profile of the fabricated waveguide at a cleaved facet. The access guides of the MMI couplers were chosen to have a width of 3 μm. The modal calculations for the SiON–SiO$_2$ rib structure indicated that a 3-μm-wide waveguide is single-mode at 1550-nm wavelength. A scalar contour plot of the field distribution in the single-mode rib waveguide is depicted in Figure 3.4. The contour plot was generated by the, previously mentioned, 2-D mode solver FWave. The SiO$_2$ buffer layer is thick enough to prevent the leaking of the field into the silicon substrate.

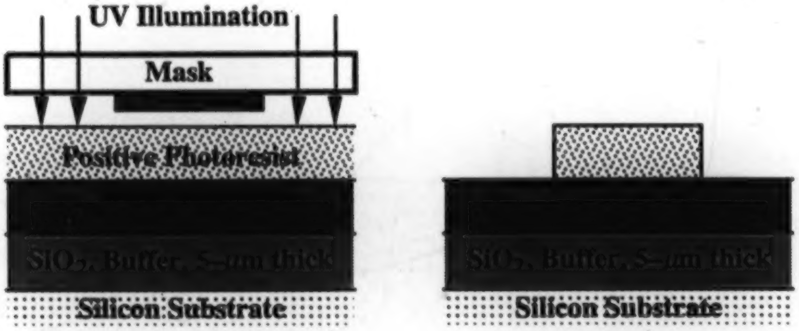
UV Illumination
Mask
Positive Photoresist
SiO$_2$, Buffer, 5–μm thick
Silicon Substrate
SiO$_2$, Buffer, 5–μm thick
Silicon Substrate

a) Expose the photoresist **b)** Develop the photoresist

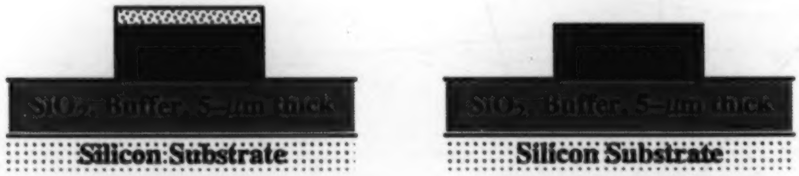
SiO$_2$, Buffer, 5–μm thick
Silicon Substrate
SiO$_2$, Buffer, 5–μm thick
Silicon Substrate

b) Etch the core layer using RIE **d)** Strip the excess resist

Figure 3.2 Photolithography and RIE process steps involved in the fabrication of the SiON–SiO$_2$ rib waveguide.

Figure 3.3 A SEM picture illustrating the rib profile.

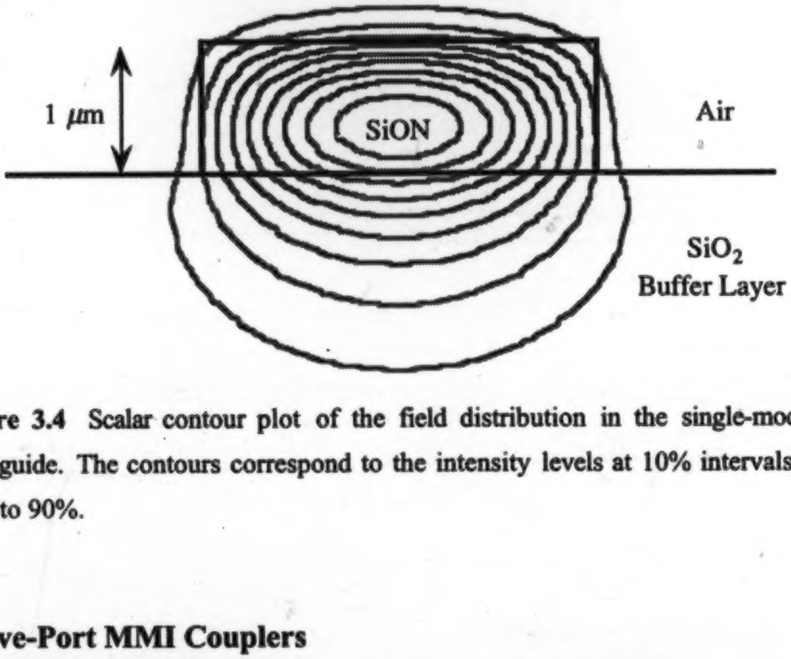

Figure 3.4 Scalar contour plot of the field distribution in the single-mode rib waveguide. The contours correspond to the intensity levels at 10% intervals from 10% to 90%.

3.2 Five-Port MMI Couplers

A general 5 × 5 MMI coupler and a 1 × 5 MMI nonuniform power splitter were designed, fabricated, and tested. The design wavelength was 1.55 μm. These five-port couplers will be used as the basic components of the five-channel MMI-phasar multiplexers in Chapter 4. The layouts of the 5 × 5 coupler and the 1 × 5 power splitter are similar to those shown previously in Figures 2.10 and 2.12, respectively, with $N = 5$. The values of the design parameters of the five-port MMI couplers are listed in Table 3.1. The couplers have a width of 30 μm, and the characteristic lengths of the 5×5 coupler and the 1×5 splitter are 708 μm and 354 μm, respectively. The 3-μm-wide access guides are placed at equally spaced positions, and the gap size between the adjacent access guides at their joining line to the MMI coupler is about 3.06 μm. Considering the tightly-bound characteristic of these waveguides, the coupling between the access guides can be safely ignored; this has been verified using FWave.

Table 3.1 Various parameters of the five-port MMI couplers designed and implemented in the SiON–SiO_2 rib waveguide system.

Description	Value
Width of the MMI couplers	30 μm
Width of the access guides	3 μm
Spacing of input/output positions of MMI couplers	6.06 μm
Number of guided modes in the MMI couplers	14
Beat length of the MMI couplers, L_π	1180 μm
Length of the 5 × 5 MMI couplers, L_c	708 μm
Length of the 1 × 5 MMI power splitter, L'_c	354 μm
General parameters of the 1 × 5 MMI power splitter	$h_1 = 7$, $h_2 = 1$, and $N' = 10$

The modal propagation analysis described in Chapter 2 was used to simulate the propagation characteristics of the MMI couplers. The light intensity pattern in the 5×5 coupler for excitation at two different input positions is illustrated in Figure 3.5. Formation of five images at the output plane of the coupler is clearly visible. By comparing the light intensity in each output port with the input power, the corresponding transmission of the coupler was determined. The simulations predict average insertion losses of 0.5 dB and 0.4 dB for the 5×5 coupler and the 1×5 splitter, respectively.

The couplers were implemented in the SiO_2–SiON rib waveguide system using the formerly-described fabrication procedure. Several versions of each device with varying coupler lengths were included on the mask to accommodate the fabrication tolerances. A 0.1-μm variation in the width of the 5×5 coupler results in a 4.5 μm change of its optimal length. Figures 3.6 and 3.7 show some of the SEM pictures of the 5×5 coupler and the 1×5 splitter. Compact *S*-bends were used to provide a separation of 150 μm between the adjacent access guides. The strongly guiding rib waveguide structure can be sharply bent without suffering excessive radiation losses.

An actual demonstration of the light propagation through the 5×5 coupler is shown in Figure 3.8. Visible light at 670-nm wavelength was launched into one of the input access guides. The light passes through the coupler and is divided between the five output ports of the coupler. The picture was taken using a CCD camera. Due to the limited resolution of the camera, the light intensity pattern in the MMI coupler is not distinguishable in Figure 3.8. Also, note that the light intensity pattern at 670-nm wavelength would be completely different from that at 1.55-μm wavelength, for which the coupler has been designed.

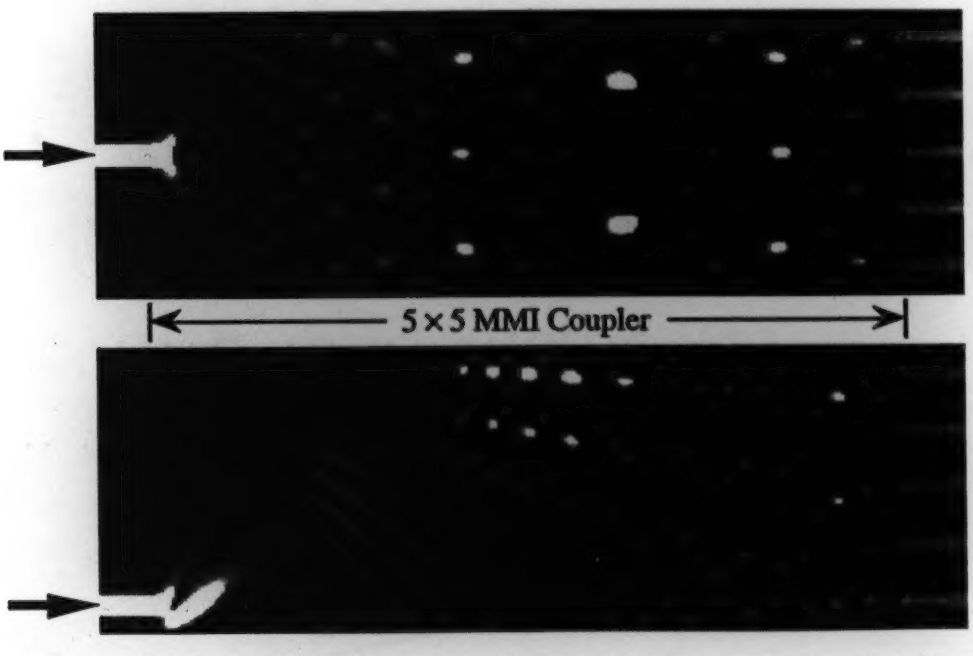

Figure 3.5 Light intensity pattern in the 5×5 MMI coupler, showing the excitation at input 3 (top) and input 1 (bottom).

(a)

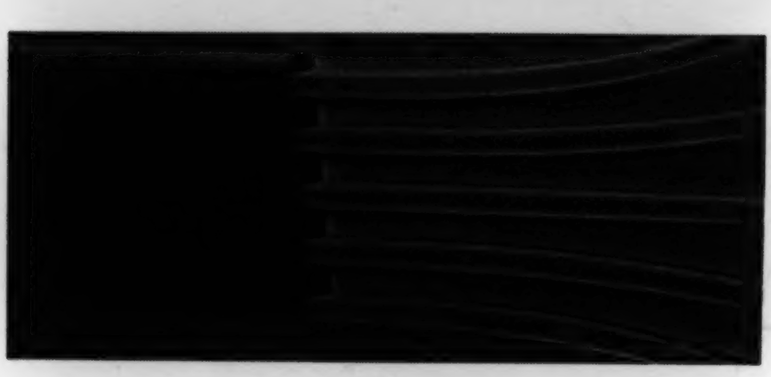

(b)

Figure 3.6 SEM picture of (a) the 5 × 5 MMI coupler fabricated in the rib waveguide structure, and (b) the magnified view of the output junction of the coupler.

Figure 3.7 SEM picture of the 1 × 5 MMI power splitter.

The transmission of the MMI couplers were measured using the experimental arrangement shown in Figure 3.9. The 1550 nm light from a DFB laser was directed via a single-mode optical fiber to a 10X collimating objective lens. The collimated beam was focused into the samples using a 20X objective lens. A polarizing beam-splitter cube was placed between the two lenses to provide TE polarized light. Also, by removing the polarizing cube we could test the devices with light beams having mixed polarizations. The samples were mounted on a three-axis micro-positioning stage. A butt-coupled multimode fiber collected the output light from the samples, for measurement using a photodetector and an optical power meter. The initial alignment of each sample was done using the visible light from a He-Ne laser instead of the 1550 nm light. Reference single-mode waveguides were placed alongside all devices, and the insertion loss of each device was measured by comparing the transmission through the device with that of the reference waveguide.

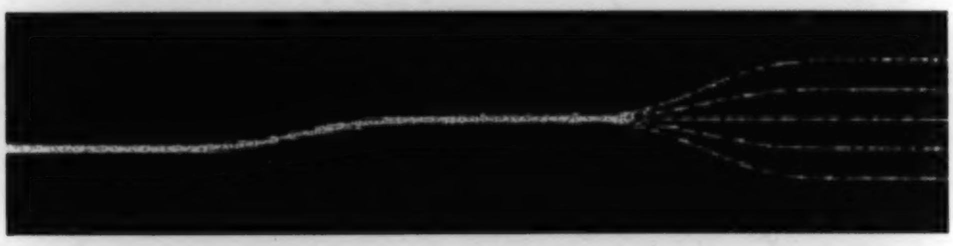

Figure 3.8 A picture showing the top view of actual light propagation in the 5 × 5 MMI coupler and its access guides. The picture was taken by a CCD camera, and a visible light wavelength of 670 nm was used.

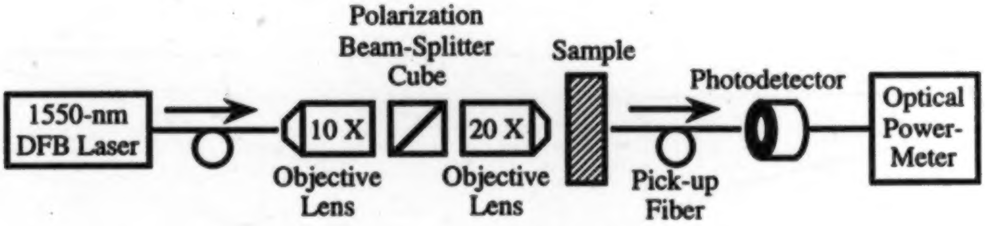

Figure 3.9 Experimental set-up used for measuring the transmission of the MMI couplers.

About twenty sets of each device were fabricated and tested. Figure 3.10 shows a typical measured transmission loss of the 5 × 5 coupler; it indicates that the coupler has an average insertion loss of about 0.3 dB and a uniformity of better than 1 dB among its outputs. The measured loss of the coupler is slightly lower than its modeled loss of 0.5 dB. This could be due to the fact that, as expected, the propagation loss caused by surface roughness of the rib waveguide is relatively larger for narrow single-mode guides than for wide multimode couplers. Another likely explanation is that the number of guided modes in the MMI coupler could be actually higher than what we have included in the modal propagation analysis.

The transmission loss of the 1 × 5 nonuniform power splitter is shown in Figure 3.11. Very good agreement between the measured and calculated results are observed. The average measured insertion loss of the 1 × 5 splitter was almost 0.3 dB. The general parameters of the 1 × 5 splitter, which were listed in Table 3.1, have been chosen for a specific output power distribution. The significance of this 1 × 5 nonuniform power splitter will become clear in Chapter 4 when we discuss the design of MMI-phasar multiplexers.

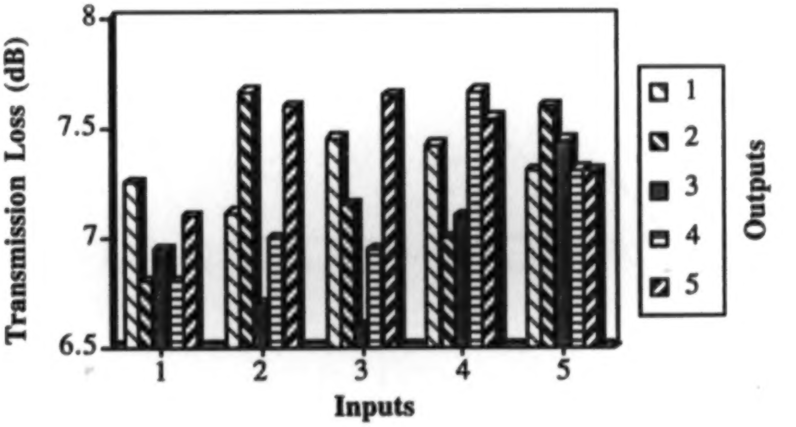

Figure 3.10 Measured on-chip transmission loss of the 5 × 5 MMI coupler at 1550-nm wavelength; the 7-dB inherent loss of the coupler is included. Each group of bars relates to the five images of an input. The estimated error in the measurements is ±0.2 dB.

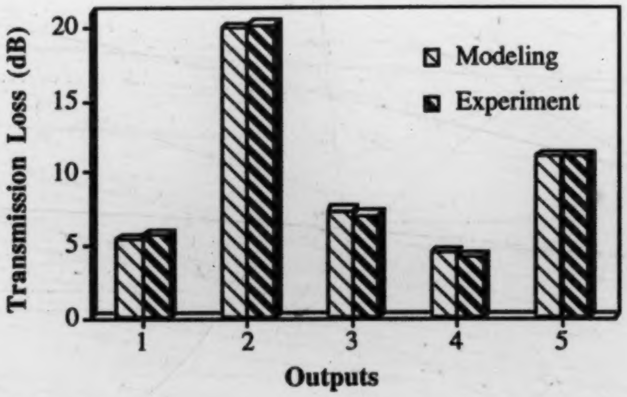

Figure 3.11 On-chip transmission loss of the 1 × 5 MMI nonuniform power splitter at 1550-nm wavelength.

3.2.1 Waveguide Losses

The propagation losses of the SiO_2–SiON rib waveguides are primarily due to two effects: material absorption because of the incorporation of hydrogen (N-H and O-H resonance absorptions) and scattering losses caused by surface roughness of the waveguides. The nitrogen-containing gases, like ammonia (NH_3), used in depositing the PECVD SiON films result in an increased amount of hydrogen in the SiON layer with resulting molecular resonance absorptions around 1.39 μm and 1.52 μm, which can be attributed to O-H and N-H resonances, respectively. This effect was first reported in [62] and it was shown that these absorption peaks can be largely removed by annealing the films at high temperature in a nitrogen atmosphere. We are particularly concerned with the N-H resonance absorption since our devices have been designed for operation at 1.55-μm wavelength. Using the cut-back method, we measured the propagation losses of the 3-μm-wide single-mode rib waveguides. The loss measurement was also performed for a set of waveguides annealed for one hour at 1050 °C in a nitrogen atmosphere. The waveguide propagation losses before and after annealing were approximately 4 dB/cm and 2 dB/cm, respectively. Thus it was verified, in agreement with [62], that annealing can overcome the molecular resonance absorptions to a large extent. Note that annealing also affects the film parameters and especially the refractive index. To completely characterize the annealing process and to examine its effects on the film parameters, the refractive index and the thickness of the films would have to be measured before and after annealing. Since our device design was done with the parameters of the unannealed films, we did not use annealing in our device fabrication.

Although the propagation losses of our SiO_2–SiON rib waveguides are relatively high, it should be said that most MMI couplers are very short (usually less than a millimeter) and their losses due to the waveguide propagation would be small. The emphasis of this thesis has been mainly on the device design and not on optimizing the fabrication process to minimize the waveguide propagation losses. Moreover, due to the limitations on access to processing equipment we were not able to modify the fabrication process. Several recommendations for further improvements in the fabrication process of the waveguides will be given in Chapter 6.

3.3 Tolerances of MMI Couplers

The performance of MMI couplers will be adversely affected if the actual parameters of the couplers vary from their design values. Relaxed tolerances for fabrication and for operating conditions are desirable. Fabrication tolerances refer to the variations in the device geometrical dimensions and the material parameters (such as refractive index) during processing. Operational tolerances relate to the variables, including wavelength, temperature, polarization, input field distribution etc., that affect the device behaviour during operation.

Modal propagation analysis can be used to investigate the effects of variations of the design parameters. Also, an analytical technique, which can predict the effect of tolerances on the device performance, has been presented in [11]. It starts with considering each image as a Gaussian beam focused at a self-imaging distance $z = L_c$. The loss penalty produced by a small finite shift δL_c in the z-position of the output waveguides can then be evaluated by overlapping the defocused beam with the output waveguide mode field. It can be shown [11] that the length shift, which produces a 0.5 dB loss penalty, is approximately equal to the so-called Rayleigh range:

$$\delta L_c \cong \frac{\pi n_g w_o^2}{4\lambda}, \tag{3.1}$$

where n_g was defined before in Section 2.1.1, and w_o is the Gaussian beam waist diameter and equals the full $1/e$ amplitude width of the input field. Expression (3.1) can be interpreted as an absolute length tolerance, which does not depend on the dimensions of the MMI coupler. The tolerances corresponding to other fabrication parameters or the wavelength can now be related to δL_c by differentiating Equation (2.29) appropriately and normalizing the results of the differentiation:

$$\frac{\delta L_c}{L_c} = 2\frac{\delta W_e}{W_e} \cong \frac{|\delta\lambda|}{\lambda} \cong \frac{\delta n_g}{n_g}. \tag{3.2}$$

In deriving (3.2), advantage is taken of the fact that the characteristic length L_c of MMI couplers is directly proportional to the beat length, as evident in Equation (2.22). A conclusion of (3.2) is that the MMI coupler length L_c must be as short as possible in order to allow for relaxed tolerances to other parameters. The width of MMI couplers has the tightest tolerance and is the most critical parameter to control during the fabrication. The sensitivity of the performance of MMI couplers to the width is simply due to the fact that, as expressed in (2.29), the beat length is directly proportional to the square of the effective width W_e.

Estimates of the tolerances for the width, wavelength, and index can be made analytically using (3.1) and (3.2). We applied (3.1) and (3.2) to the five-port MMI couplers described previously; the corresponding values of the fabrication tolerances and the optical bandwidth of these couplers for 0.5 dB excess losses are listed in Table 3.2. The analysis developed in [11] also indicates that for a given waveguide system the fabrication tolerances are independent of the number N of the input/output ports, while the optical bandwidth is inversely proportional to N. In the next two sections, the fabrication tolerances and optical bandwidth of the five-port MMI couplers will be examined using both the modal propagation analysis and the experimental measurements.

Table 3.2 Analytical estimates of the fabrication tolerances and optical bandwidth of the five-port MMI couplers for 0.5 dB excess losses.

	Length tol. δL_c (μm)	Width tol. δW_e (μm)	Bandwidth $2\delta\lambda$ (nm)	Index tol. δn_g
The 5 × 5 coupler	±8.8	±0.19	39	±0.0185
The 1 × 5 splitter	±8.8	±0.38	78	±0.037

3.3.1 Fabrication Tolerances

The average insertion loss of the 5 × 5 coupler was measured for several coupler lengths. The measurements as well as the results of the modal propagation simulation are shown in Figure 3.12. A coupler length with the lowest loss is considered to be optimum. It is seen that the actual optimum length of the coupler is a few microns higher than its calculated value of 708 μm. This is most likely due to the fact that the width of the fabricated coupler is slightly larger than its designed value. The fabrication tolerances can be evaluated using the curves shown in Figure 3.12. The simulated values of the fabrication tolerances are close to those listed previously in Table 3.2. From the experimental curve, fabrication tolerances of $\delta L_c = \pm 6$ μm corresponding to $\delta W_e = \pm 0.14$ μm are achieved with a limit of 0.5 dB excess losses. Also, note that a 0.1-μm variation of the width of the 5 × 5 coupler results in approximately 4.5-μm change of its optimal length, and this increases the coupler loss by about 0.25 dB.

In addition to the average insertion loss of the coupler, the behaviour of the individual outputs with respect to the fabrication variations is important for applications such as MMI-phasar multiplexers and Mach–Zehnder switches. The transmission loss and the phase response of all outputs of the 5 × 5 MMI coupler were calculated. Typical

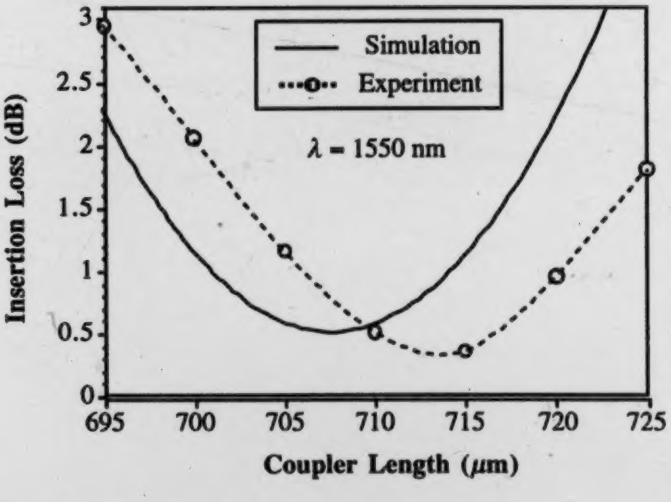

Figure 3.12 Insertion loss of the 5 × 5 MMI coupler as a function of the coupler length. A wavelength of 1550 nm was used.

normalized transmission of the outputs of the 5 × 5 coupler as a function of the coupler length is depicted in Figure 3.13. It is seen that each output transmission is at a local maximum around the optimum coupler length L_c. All output transmissions decrease similarly for deviations from the optimum length and, consequently, the sensitivity to the tolerances is minimum at the optimum length. It can be concluded that MMI couplers are capable of maintaining a very good output uniformity or balance over a large range of fabrication and operational variations. As it was mentioned in Chapter 1, the uniformity of the couplers translates directly into crosstalk in devices such as Mach–Zehnder switches or MMI-phasar multiplexers. The MMI couplers have a clear advantage over the conventional directional couplers in this regard.

Figure 3.14 shows the typical phase deviations of the outputs of the 5 × 5 coupler as a function of the coupler length. The phase deviations were calculated by comparing the results of the modal propagation simulation and the corresponding values from the analytical phase relation (2.58). It can be observed that the phase changes of all outputs are similar and follow each other closely over a certain range of tolerances. It can be predicted from Figure 3.14 that the phase deviations are limited to within ±5 degrees over a coupler length variations of about ±13 μm.

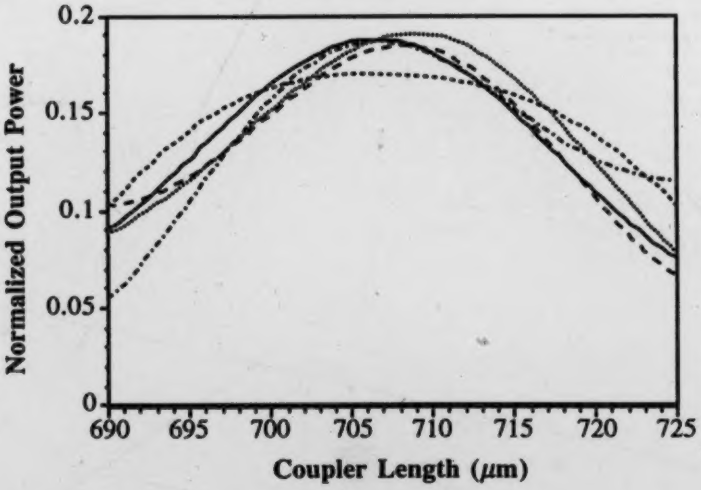

Figure 3.13 Typical relative transmission of the outputs of the 5 × 5 coupler as a function of the coupler length.

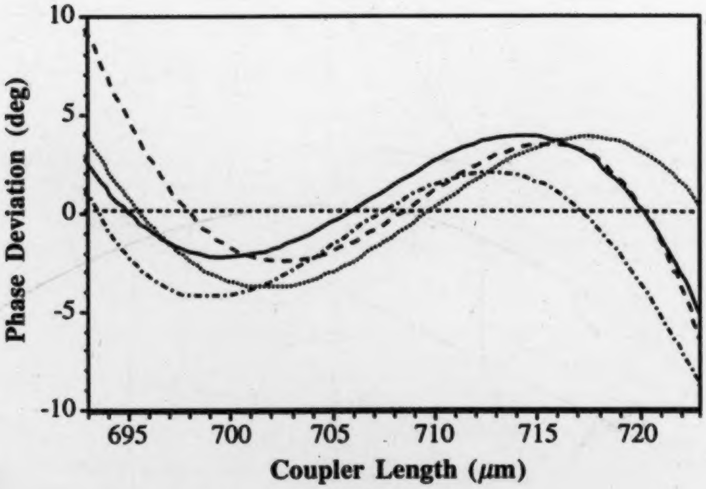

Figure 3.14 Typical phase deviations of the outputs of the 5 × 5 MMI coupler as a function of the coupler length.

3.3.2 Optical Bandwidth

The optical bandwidth of MMI couplers is of significance in designing devices such as MMI-phasar multiplexers, which have to operate over a range of wavelengths. The wavelength sensitivity of MMI couplers can be inferred from other tolerances through Equation (3.2). However, we investigated the wavelength dependence of the MMI couplers directly by the experimental measurements and the modal calculations.

The optical bandwidth the MMI couplers was measured with the set-up shown in Figure 3.15. The light from a external-grating tunable diode laser was directed through a half-wave plate and a mechanical chopper, and was focused by a lens into a polarization-maintaining single-mode fiber. The light was launched into the devices by butt-coupling the other end of the single-mode fiber to the samples. The output light from the samples was collected using a butt-coupled multimode fiber and directed to a photodetector. A lock-in amplifier was used to enhance the signal and suppress the noise in the system. The wavelength scanning of the tunable laser was done automatically via a micro-computer. The samples were mounted on a three-axis micro-positioning stage.

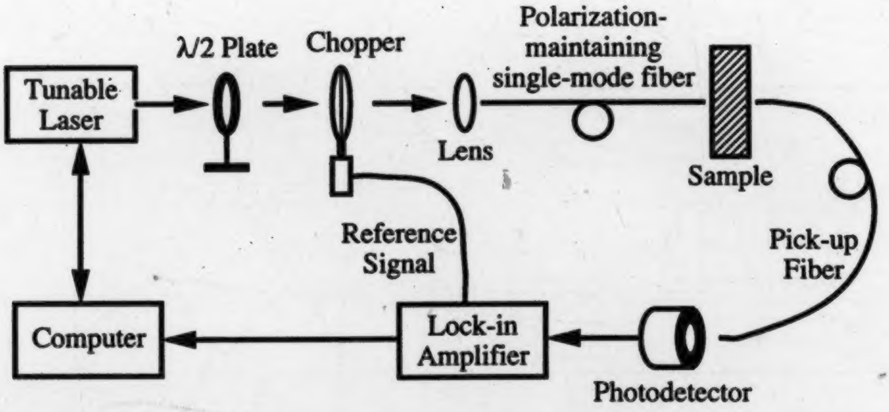
Tunable Laser
λ/2 Plate
Chopper
Lens
Polarization-maintaining single-mode fiber
Sample
Pick-up Fiber
Reference Signal
Computer
Lock-in Amplifier
Photodetector

Figure 3.15 Experimental arrangement used for measuring the optical bandwidth of the MMI couplers.

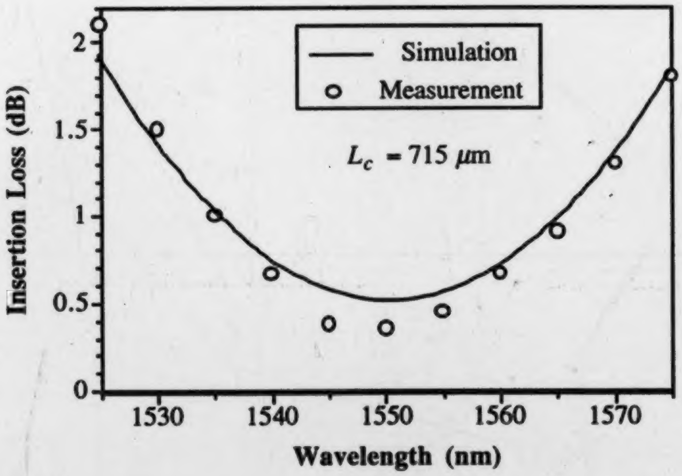

Figure 3.16 Optical bandwidth of the 5×5 MMI coupler. The performance has been considered at a coupler length of 715 μm.

The average insertion losses of the 5×5 coupler and the 1×5 splitter are shown in Figures (3.16) and (3.17), respectively. With a limit of 0.5 dB excess losses, measured optical bandwidths of more than 30 nm and 50 nm were obtained for the 5×5 coupler and the 1 × 5 splitter, respectively. The corresponding simulated results are again close to those listed previously in Table 3.2.

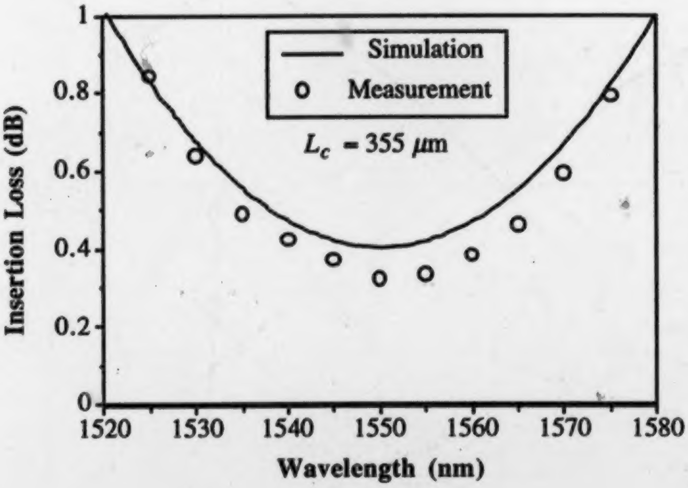

Figure 3.17 Optical bandwidth of the 1 × 5 MMI nonuniform power splitter. The performance has been considered at a coupler length of 355 μm.

3.3.3 Polarization Dependence

We know that beat length is the most significant parameter in the design of MMI couplers. The beat length is related to the variables n_g and W_e through Equation (2.29). Both n_g and W_e are polarization-dependent and generally, for an arbitrary waveguide structure, the beat lengths corresponding to TE and TM polarizations are not equal [17]. Consequently, the optimum imaging lengths for the two polarizations are slightly different. This polarization-dependent behaviour has even been employed to design an MMI coupler with a polarization splitting function [24]. However, for most applications it is desired that MMI couplers be polarization-insensitive. In principle, by designing the coupler at an intermediate length, polarization-insensitive operation can be obtained at the price of a small loss increase. Also, MMI couplers can be made polarization-independent by choosing the waveguide structure so that the beat lengths for the two polarizations are equal. This is a less demanding requirement than having to make the absolute values of the propagation constants of the TE and TM modes to be equal.

For the SiO_2–SiON rib waveguide structure used in our designs, the calculations indicated a small difference between the beat lengths corresponding to the two polarizations. For example, the TM optimum length of the 5 × 5 MMI coupler was calculated to be longer than its TE counterpart by about 7 μm. To examine this, the transmission loss of the couplers were measured with the TM-polarized light. For a 5 × 5 coupler with the TE optimum length, an extra loss of about 0.4 dB was observed for the TM polarization. The same measurements for the 1 × 5 power splitter revealed a negligible polarization sensitivity. Note that the polarization sensitivity of the MMI couplers increases with the length of the couplers. The 1 × 5 splitter is expected to be less sensitive to polarization since it is only half as long as the 5 × 5 coupler.

The performance results of the five-port MMI couplers, which were presented in this chapter, relate to the TE polarization. The corresponding TM results are only slightly different allowing for the small discrepancy between the TE and TM optimum lengths. In general, polarization insensitivity can be obtained with the couplers designed at intermediate lengths.

4. Phased-Array Wavelength Multiplexers Using Multimode Interference Couplers

The large optical bandwidth of existing fiber can be accessed through wavelength-division multiplexing (WDM). In addition to increasing the transmission capacity of a point-to-point system, WDM is also becoming increasingly important in optical network applications such as wavelength-routing and circuit switching. The key components of a WDM transmission system are wavelength (de)multiplexers. In this chapter, we demonstrate planar phased-array wavelength multiplexers using MMI couplers.

The analytical derivation of phases of images in general $N \times N$ MMI couplers [9] has paved the way for designing optical components such as generalized Mach–Zehnder switches [27], [28], and wavelength multiplexers based on $N \times N$ MMI couplers [66]–[70]. These wavelength multiplexers, which are referred to as MMI-phasar, consist of an array of N monomode waveguides placed between two MMI couplers, and operate on N equally spaced wavelength channels. The number of guides of the array of MMI-phasar multiplexers is much smaller compared with that of the AWG multiplexers described in Chapter 1. Moreover, unlike the AWG, the length difference between adjacent guides in the array of an MMI-phasar device is not necessarily a constant value. We provide a general methodology for designing MMI-phasar multiplexers, and present a simple procedure for finding an optimum combination of the lengths of the array guides that results in a small device size with improved performance. It is shown that the wavelength-routing characteristics of the MMI-phasar devices enable them to operate also as add–drop multiplexers and $N \times N$ interconnecting components in WDM-based optical networks; these routing functions are similar to those offered by the AWG multiplexers, as illustrated previously in Figure 1.5. The material of this chapter closely follows our work offered in [68]–[70].

4.1 Basic Device Structures and the Operation Principle

General layouts of two variations of N-channel MMI-phasar multiplexers are shown in Figure 4.1. An MMI-phasar device consists of three main elements: an N-way MMI power splitter, an array of N monomode waveguides, and an $N \times N$ MMI power splitter/recombiner. Wavelength dispersion is provided by the waveguide array. The MMI couplers are effectively insensitive to wavelength over the desired wavelength range. An optical field at any of the input ports of an $N \times N$ MMI coupler is reproduced at the coupler outputs in the form of N self-images with equal intensity and different phases. Incoming light to the multiplexer is therefore distributed by the first MMI coupler to the array guides. The several paths through the array induce relative phase delays proportional to the length differences between the array arms. The second MMI coupler distributes the power incident at each of its inputs to all outputs (k) where interference occurs between the relatively delayed optical fields. The lengths of the array arms have to be chosen so that constructive interference occurs for different wavelengths at different outputs of the combiner. To prevent cross coupling, waveguides of the array must not cross each other.

As shown in Figure 4.1, the same numbering direction has been used for input ports and output ports of the MMI couplers. The outputs of the splitter, inputs of the combiner, and the array arms have been numbered in the same way and are all denoted by index j. This numbering convention facilitates our analysis in the next section by allowing us to use the same numbering everywhere in the multiplexer structure. The device depicted in Figure 4.1(b) is similar to that shown in Figure 4.1(a) except that the former employs a $1 \times N$ MMI nonuniform power splitter instead of an $N \times N$ MMI coupler. With equal power splitting, the sidelobe levels in the spectral transmission of an MMI-phasar multiplexer cannot be lower than those of the sinc function. However, by using an appropriate nonuniform power splitter, the power distribution across the array guides can be properly shaped to improve the sidelobe suppression ratio [68].

Let the m-th guide of the array be its shortest arm; then in accordance with our assumption that the array guides do not cross each other, the lengths of the array arms (L_j) must meet the following requirement:

$$L_{j_2} > L_{j_1} \quad \text{if} \quad (j_2 > j_1 \geq m \text{ or } j_2 < j_1 \leq m). \tag{4.1}$$

The relationship between the phases of the self images in MMI couplers was derived in Chapter 2. The lengths of the array arms have to be chosen so that the relative phase delays through the array in combination with the phase relations of the MMI couplers bring about the required phase-match state at the outputs of the multiplexer. In an MMI-phasar device, there are several possible combinations of the lengths of the arms that satisfy the phase-match conditions. An important issue in the design of MMI-phasar multiplexers is finding an optimum combination of the lengths of the array arms that results in a small device with the best spectral response. In our search for an optimum

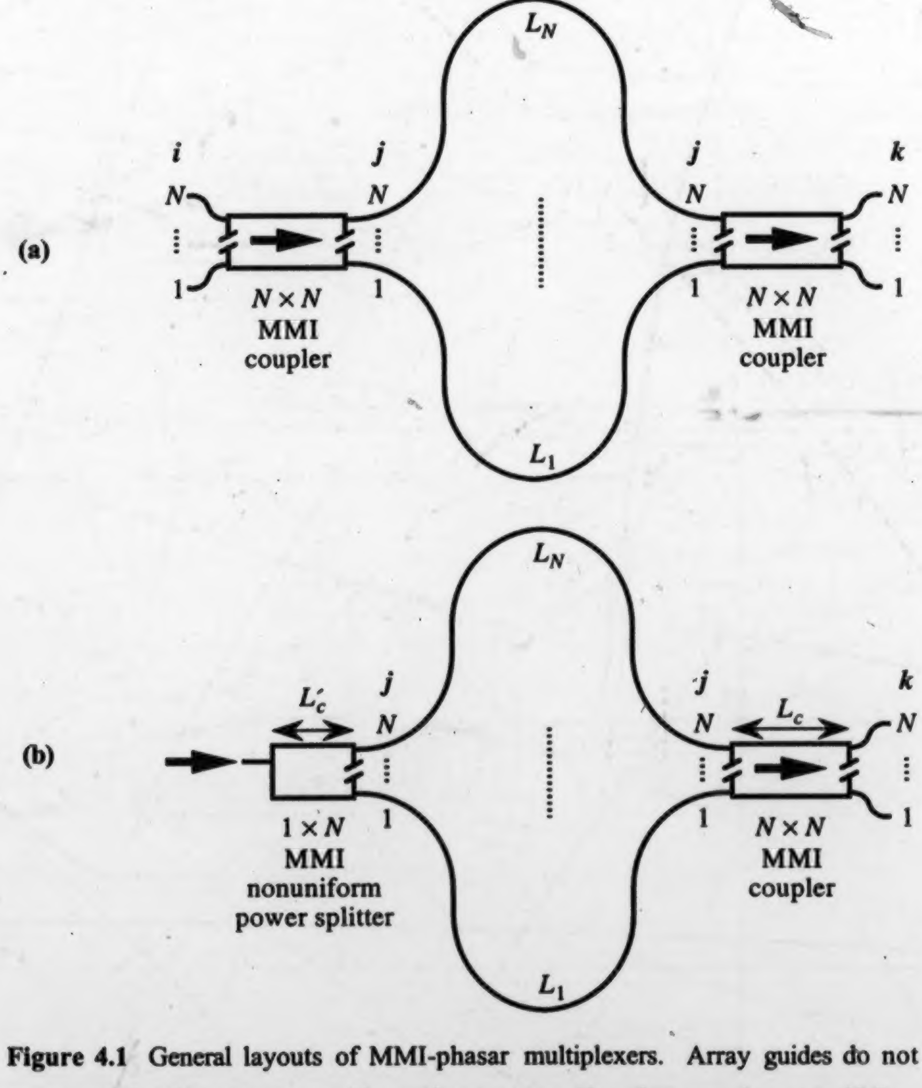
(a)
L_N
L_1
i
N
1
j
N
1
j
N
1
k
N
1
N × N
MMI
coupler
N × N
MMI
coupler
(b)
L_N
L_1
L'_c
L_c
j
N
1
j
N
1
k
N
1
1 × N
MMI
nonuniform
power splitter
N × N
MMI
coupler

Figure 4.1 General layouts of MMI-phasar multiplexers. Array guides do not cross, and the shortest array guide can be any arm other than arm 1 or arm N (i.e., $m \neq 1, N$). (a) With an $N \times N$ MMI coupler as the power splitter, (b) with a $1 \times N$ MMI nonuniform power splitter.

combination, we have to look at all possible values for m. For the geometric layouts shown in Figure 4.1, the shortest array guide can be any arm other than arm 1 or arm N ($m \neq 1, N$). The symmetry of the device allows us to restrict the value of m to the following range:

$$m = 2,\ 3,\ \ldots,\ \mathrm{Ceil}(N/2); \tag{4.2}$$

Ceil(x) is the smallest integer that is greater than or equal to x.

Waveguide bends are crucial elements in determining the size of an integrated planar photonic circuit. The radius of curvature of a waveguide bend has to be large enough to avoid excessive radiation losses. If the shortest array guide of an MMI-phasar multiplexer is chosen to be the first arm ($m = 1$), then a small device size can be obtained with the layout shown in Figure 4.2. Array guides bend through 180° in this layout, which is more compact overall than the layout presented in Figure 4.1(a), where array arms must bend through a total of 360°. However, because the possible sets of lengths of

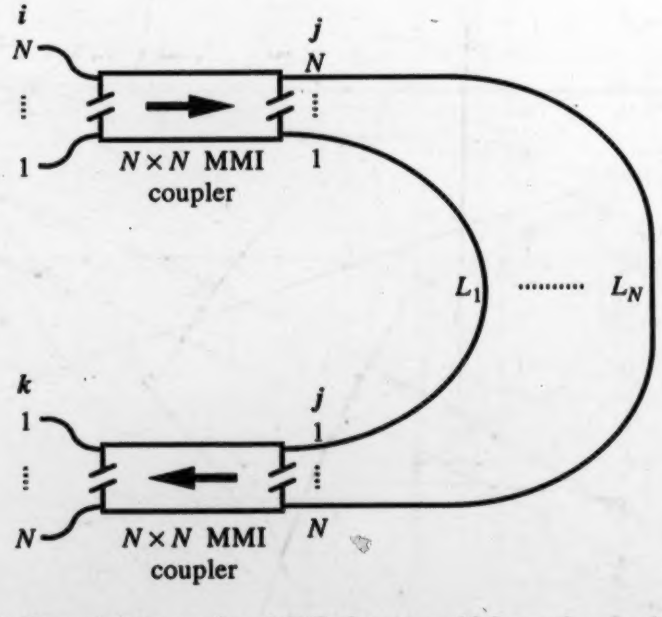

Figure 4.2 General layout of an MMI-phasar multiplexer that is similar to the structure depicted in Figure 4.1(a) except that the shortest array guide in this case is the first arm ($m = 1$).

the array guides are more limited in the case of the structure depicted in Figure 4.2, as we see in subsequent sections, this structure generally has a poorer spectral response compared with that offered by the structure shown in Figure 4.1(a).

The lengths of the array arms of an MMI-phasar do not necessarily relate to the array guide number j in a simple linear fashion. Therefore we introduce an integer parameter d_j called the array arm factor, and we show in the next section that the length L_j of an array guide is given by

$$L_j - L_m \cong d_j \Delta L \quad \text{for } j = 1,\ \ldots,\ N, \tag{4.3}$$

where L_m is the length of the shortest arm and ΔL is defined as the length that produces a phase shift of $2\pi/N$ between two adjacent wavelength channels. Exact values of L_j might be slightly different from those given in (4.3) in order to satisfy the phase-match requirements at the outputs of the multiplexer. The approximation sign in (4.3) indicates that the relative lengths $L_j - L_m$ have to be as close as possible to $d_j\Delta L$. Relation (4.3) implies that the condition on the lengths of the array arms as expressed by inequality (4.1) can be carried over directly to the array arm factor d_j; i.e.,

$$d_{j_2} > d_{j_1} \quad \text{if } (j_2 > j_1 \geq m \text{ or } j_2 < j_1 \leq m). \tag{4.4}$$

The smallest array arm factor is $d_m = 0$, and the largest one, $d_j^{\max}$, is either d_N or d_1 where $d_j^{\max} \geq N-1$. Now, a better understanding of an MMI-phasar device can be obtained by considering the fact that the operation of an MMI-phasar multiplexer, for each route (i, k), resembles that of an optical transversal filter having $d_j^{\max}+1$ taps of which N taps have nonzero weight and the remaining $d_j^{\max}+1-N$ taps have zero weight. It is desirable to reduce the number of zero-weight taps in order to diminish the magnitude of the unwanted spectral content in the transmission response of the device. An improved spectral response together with a small device size can therefore be obtained by minimizing $d_j^{\max}$. Design optimization of an MMI-phasar multiplexer involves finding a set of values of the array arm factor with a $d_j^{\max}$ as small as possible. Also, it should be noted that the multiplexer of Figure 4.1(b) allows for a suitable weight distribution to improve the sidelobe suppression ratio. The rejection of sidelobes can be increased by selecting a properly shaped weight distribution. In such a distribution, tap weights gradually increase with the tap number (or d_j in this case) and then gradually decrease; the taps with the highest weight values are located close to $d_j^{\max}/2$.

4.2 Theoretical Formulation and Device Design

An MMI-phasar multiplexer operates over *N* equally spaced wavelength channels. Let us represent these *N* wavelengths as λ_s, where the subscript *s* is an integer defined in the following range:

$$s = -\mathrm{Ceil}\left(\frac{N-1}{2}\right), \ \ldots, \ \mathrm{Ceil}\left(\frac{N}{2}\right) - 1. \tag{4.5}$$

For example, the channels for cases $N = 4$ and $N = 5$ are denoted by $\{\lambda_{-2}, \lambda_{-1}, \lambda_0, \lambda_1\}$ and $\{\lambda_{-2}, \lambda_{-1}, \lambda_0, \lambda_1, \lambda_2\}$, respectively. The wavelength increases with the subscript; that is, $\lambda_{s+1} - \lambda_s = \Delta\lambda$, where $\Delta\lambda$ is the channel spacing. λ_0 is taken as the center wavelength. The spectral response of the MMI-phasar multiplexer is taken to be periodic with a free spectral range of $N\Delta\lambda$. This assumption of periodicity is valid in the range over which the MMI couplers can be assumed to be wavelength insensitive.

Consider the device structures of Figures 4.1(a) and 4.2, which have multiple input ports. These structure are symmetrical in the sense that input ports and output ports can be used interchangeably. When an optical signal consisting of *N* wavelengths $\{\lambda_s\}$ is launched into input guide *i*, each wavelength is incident on one and only one of the multiplexer outputs *k*. Each route (*i*, *k*) in the multiplexer corresponds to a wavelength $\lambda_{s_{i,k}}$. Exploiting both the symmetry and the reciprocity of the device, we can write the following useful relation:

$$s_{i',k'} = s_{i,k} \ \text{ if } \left(i' = k \text{ and } k' = i\right). \tag{4.6}$$

Routes (*i'*, *k'*) and (*i*, *k*) have similar spectral transmissions and are assigned to the same wavelength channels when the condition stated in (4.6) is satisfied. For example, routes (2, 5) and (5, 2) correspond to the same wavelength. The important consequence of (4.6) is that the design of these multiplexers is independent of the input port. In other words, the lengths of the array arms do not change if we alter the input port in our design. It is therefore sufficient to consider the design of the multiplexer for only one of its inputs.

The wavelength selection by a given output of the MMI-phasar multiplexer is a result of constructive interference (or phase match) between signal components arriving at that output and phase mismatch for that wavelength at other outputs. A phase-match state at an output of an MMI-phasar device is produced if the relative phase delays through the array arms compensate for the phase relations of the MMI couplers. To design an MMI-phasar multiplexer, one has to find an appropriate set of lengths for the array arms to bring about the phase-match state simultaneously at different outputs of the multiplexer for different wavelength channels. We show that such a set of lengths exists and provide a simple procedure for determining the lengths of the arms. As described before, all the arms of an array are compared with the reference (shortest) arm, which is denoted by m.

Let us first examine the multiplexer operation at the center wavelength λ_0. It is always possible and trivial to find a set of lengths for the arms to establish a phase match for only one wavelength channel of the multiplexer. It is assumed that the lengths of the arms are chosen to achieve phase match at the multiplexer output $k = m$, that is, all the signal components of wavelength λ_0 are in phase on arrival at the multiplexer output m. However, such constructive interference does not occur for the center wavelength at other outputs $k \neq m$; this phase mismatch is dictated only by the phase relations of the $N \times N$ MMI power combiner and does not depend on the power splitter. Note that, for a given input port of the multiplexer, the paths through the MMI power splitter remain fixed for all outputs of the multiplexer. At the multiplexer output k, the phase difference between the signal component arriving from an arm $j \neq m$ and the one arriving from the reference arm m can be expressed as

$$\Delta\varphi_{j,k} = \left(\varphi_{j,k} - \varphi_{m,k}\right) - \left(\varphi_{j,m} - \varphi_{m,m}\right), \tag{4.7}$$

where the phase expression φ was given previously by (2.58). $\Delta\varphi_{j,k}$ is independent of the MMI power splitter and the multiplexer input port i. The term inside the second set of parentheses in (4.7) represents the phase difference between these signal components at the input of the $N \times N$ MMI power combiner if we assume phase match at the multiplexer output $k = m$. Now, if the length difference between arms j and m is chosen such that the relative phase delay through these arms at a given wavelength $\lambda \neq \lambda_0$ offsets the value of $\Delta\varphi_{j,k}$, then wavelength λ will be selected by output k. The significance of expression (4.7) is the fact that it decides the required combination of lengths for the array arms and determines the wavelength channel assignment of the multiplexer. By substituting for φ from (2.58) into (4.7), we get

$$\begin{aligned}\Delta\varphi_{j,k} = {} & \frac{\pi(-1)^N}{2N}\left[\left((-1)^{j+m}(j-1/2)-(m-1/2)\right)\left((-1)^{k+m}(k-1/2)-(m-1/2)\right)\right] \\ & -\frac{\pi(-1)^N}{2}\left[1-(-1)^{j+m}-(-1)^{k+m}+(-1)^{j+k}\right].\end{aligned} \tag{4.8}$$

The terms enclosed by the two brackets in (4.8) are both integer multiples of 4, and, consequently, $\Delta\varphi_{j,k}$ is always an integer multiple of $2\pi/N$. This property of $\Delta\varphi_{j,k}$ confirms the validity of two of our earlier statements: that of equal channel spacing, and relation (4.3) for the lengths of the array arms. Note that, according to relation (4.3), the length difference between the array arms j and m results in a phase shift of an integer multiple of $2\pi/N$ between any two wavelength channels. To find the array arm factor d_j, let us define a new parameter as follows:

$$\psi_{j,k} = \left(-\frac{N}{2\pi}\Delta\varphi_{j,k}\right) \bmod N, \tag{4.9}$$

where mod indicates the modular arithmetic operation. It is more convenient to deal with $\psi_{j,k}$ since its value is always an integer number and not a multiple of $2\pi/N$. The mod N operation has been used to limit the value of $\psi_{j,k}$, which has a periodicity of N, to the range $0, \ldots, N-1$. The phase term associated with travel through the array arms has to be of opposite sign to the transfer phase of the $N \times N$ MMI coupler, and hence we have the negative sign in (4.9). By substituting for $\Delta\varphi_{j,k}$ from (4.8) into (4.9), we obtain

$$\psi_{j,k} = \left[-\frac{(-1)^N}{4}\left((-1)^{j+m}(j-\frac{1}{2})-(m-\frac{1}{2})\right)\left((-1)^{k+m}(k-\frac{1}{2})-(m-\frac{1}{2})\right)\right] \bmod N. \tag{4.10}$$

The symmetry relation $\psi_{j,k} = \psi_{k,j}$ is easily derived from (4.10). Also, it can be seen that, as expected, values of $\psi_{m,k}$ and $\psi_{j,m}$ are always zero. The array arm factor is directly related to $\psi_{j,k}$ and can be expressed as

$$d_j = \psi_{j,k_1} + B_j N \quad \text{for } j = 1, \ldots, N; \tag{4.11}$$

where B_j is the smallest integer that satisfies the requirement expressed by (4.4) and k_1 is the multiplexer output that selects the channel λ_1 adjacent to the center wavelength. Note that k_1 can represent any output other than output m, which has been assigned to the center wavelength λ_0. A characteristic of $\psi_{j,k}$ is that it does not necessarily increase monotonically with j. Therefore, B_j has been introduced in (4.11) to avoid waveguide crossing in the array.

The channel assignment of the multiplexer can also be inferred from $\psi_{j,k}$. Each output of the multiplexer has to select a different channel. Assuming that output $k = m$ corresponds to the center wavelength λ_0, then the subscript s of a wavelength channel, as defined in (4.5), is related to an output k by

$$s \bmod N = \psi_{j_1,k} \quad \text{for} \quad k = 1, \ldots, N; \tag{4.12}$$

where $\psi_{j_1,k_1} = 1$ for k_1 as defined before and the mod N operation has been used to make the range of defined values of s consistent with that of $\psi_{j,k}$.

For each combination of m and k_1, one can obtain a distinct possible set of values of d_j using (4.11) and (4.10). The largest array arm factor $d_j^{\max}$ is not the same for all sets. As explained in Section 4.1, the spectral response of an MMI-phasar multiplexer is optimized if $d_j^{\max}$ is as small as possible. Therefore, after determining the value of $d_j^{\max}$ for every possible combination of m and k_1, one must pick a combination that results in the smallest $d_j^{\max}$ for the multiplexer design. Output k_1 can be any integer from 1 to N except that $k_1 \neq m$. The range of values of m is restricted to that given by (4.2); we have also allowed the case of $m = 1$ to include the multiplexer structure of Figure 4.2.

To illustrate this straightforward procedure for finding an optimum set of values of d_j, let us look at the example of the five-channel multiplexer ($N = 5$). After calculating the value of $d_j^{\max}$ for all possible combinations of m and k_1, we find that the smallest value of $d_j^{\max}$ is achieved for the combination of $m = 2$ and $k_1 = 5$. Values of $\psi_{j,k}$ for the case of $m = 2$ are shown in Table 4.1. One can obtain a different set of values of d_j by applying (4.11) to each row of Table 4.1; the last column of Table 4.1 shows the value of $d_j^{\max}$ for each set. Since the shaded row has the smallest value of $d_j^{\max}$, its associated set of values for the array arm factor d_j is optimum in terms of the spectral response of the device. Also, to find the channel assignment of the multiplexer, we first need to find j_1 such that $\psi_{j_1,k_1} = 1$. By inspecting Table 4.1, it is seen that $\psi_{3,5} = 1$, that is, $j_1 = 3$. Then one can infer the wavelength assignment of the multiplexer by applying (4.12) to the column associated with j_1; this is the shaded column.

Using the procedure described above, we can easily find the optimum set of d_j values for an MMI-phasar multiplexer of any number of channels, N. Table 4.2 shows the optimum sets of values of the array arm factor for the cases of $N = 3$ as high as $N = 12$. In fact, the last number in each row gives the value of $d_j^{\max}$ for each case. We already know that $d_j^{\max} \geq N - 1$ and that the spectral response of the multiplexer is optimized if the value of $d_j^{\max} - N$ is as small as possible. However, it is seen from Table 4.2 that the value of $d_j^{\max} - N$ increases rapidly with *N*. It can therefore be said that these WDM devices perform best for a moderate value of *N*.

Let us turn our attention to the device structures of Figures 4.1(a) and 4.2, in which all input ports can be used for the demultiplexing operation. The wavelength-routing provided by each input is distinct from that of other inputs. A given output *k* is addressed by different inputs *i* through different wavelengths; one can easily verify this by exploiting the symmetry of the multiplexer structure and treating the multiplexer outputs as its inputs. The wavelength-routing properties of these devices make them potentially capable of functions such as $N \times N$ WDM interconnecting. To find the complete wavelength assignment of the multiplexer, a relationship between the wavelengths associated with different routes has to be derived. Using the fact that $\psi_{j,k}$ is independent of the multiplexer input *i*, we can write

$$\left(s_{i,k} - s_{i,m}\right) \bmod N = \left(s_{m,k} - s_{m,m}\right) \bmod N . \tag{4.13}$$

Replacing $s_{i,m}$ by $s_{m,i}$ in (4.13) and after rearranging, we get

$$s_{i,k} \bmod N = \left(s_{m,i} + s_{m,k} - s_{m,m}\right) \bmod N . \tag{4.14}$$

Assuming that the center wavelength λ_0 is assigned to route (*m*, *m*), then the wavelengths

Table 4.1 Values of $\psi_{j,k}$ for the case of $m = 2$ in a five-channel multiplexer. The last column shows the value of $d_j^{\max}$ for each possible set of values of d_j. The shaded row, which corresponds to the smallest $d_j^{\max}$, is used to obtain an optimum set of values of d_j. Channel assignment of the multiplexer can be determined from the shaded column.

k	***j***					$d_j^{\max}$
	1	**2**	**3**	**4**	**5**	
1	1	0	2	4	3	8
2	0	0	0	0	0	—
3	2	0	4	3	1	11
4	4	0	3	1	2	7
5	3	0	1	2	4	4

Table 4.2 Optimum set of values of the array arm factor d_j for an N-channel multiplexer. The cases of $N = 3$ to as high as $N = 12$ are shown.

N	Array guide number (j)											
	1	**2**	**3**	**4**	**5**	**6**	**7**	**8**	**9**	**10**	**11**	**12**
3	0	1	2									
4	1	0	2	3								
5	3	0	1	2	4							
6	5	4	0	3	7	8						
7	4	0	1	3	5	6	9					
8	6	3	1	0	4	5	7	10				
9	14	7	3	0	1	2	8	13	15			
10	16	9	3	2	0	5	7	8	14	21		
11	23	17	7	0	2	5	8	10	14	15	20	
12	15	10	8	5	1	0	6	7	11	14	16	21

corresponding to routes (m, k) are given by (4.12). Hence, all the terms inside the parentheses in (4.14) are known, and the wavelength corresponding to any arbitrary route (i, k) can be determined. As an example, the wavelength assignment of the five-channel device, which was already discussed, is given in Table 4.3. The wavelengths in column $i = 2$ have been obtained by applying (4.12) directly to the shaded column in Table 4.1. The other wavelengths in Table 4.3 were found using (4.14). A 5×5 WDM interconnection operation is possible with only five wavelength channels. Also, note that it is a general characteristic of MMI-phasar multiplexers that neighboring channels are not necessarily selected by adjacent output guides; this fact is apparent in Table 4.3.

As the final step in our analysis, we need to derive expressions for the exact lengths of the array guides. The lengths of the array guides have to be such that the relative phase delays associated with traveling through the array compensate for the corresponding phase relations of both the MMI power splitter and the MMI power splitter/combiner. For the case of the multiplexer structures of Figures 4.1(a) and 4.2, the phase-match state is established if the lengths L_j of the array arms satisfy the following relation:

$$(L_j - L_m)\beta(\lambda_{s_{i,k}}) - (\varphi_{i,j} + \varphi_{j,k} - \varphi_{i,m} - \varphi_{m,k}) = A_{i,j,k}2\pi, \tag{4.15}$$

where $\beta(\lambda)$ is the propagation constant at wavelength λ, m indicates the shortest (reference) arm, $\lambda_{s_{i,k}}$ is the wavelength assigned to route (i, k), phase φ is given by (2.58), and $A_{i,j,k}$ is an integer. Now for i, $k = m$, and $s_{m,m} = 0$, we can rewrite (4.15) as

$$(L_j - L_m)\frac{2\pi n_{e0}}{\lambda_0} - 2(\varphi_{m,j} - \varphi_{m,m}) = A_{m,j,m}2\pi, \tag{4.16}$$

where n_{e0} is the effective index value of the mode of an array guide at wavelength λ_0. Note that the relation $\varphi_{m,j} = \varphi_{j,m}$ has been used in deriving (4.16). By rearranging (4.16), we arrive at

$$L_j - L_m = \left(A_{m,j,m} + \frac{\varphi_{m,j} - \varphi_{m,m}}{\pi}\right)\frac{\lambda_0}{n_{e0}}. \tag{4.17}$$

The arm length L_j has to satisfy (4.17) while it has to be as close as possible to that given by (4.3). Using this fact, an expression for $A_{m,j,m}$ can be obtained by combining (4.17) and (4.3):

$$A_{m,j,m} = \mathrm{Rnd}\left(d_j\Delta L\frac{n_{e0}}{\lambda_0} - \frac{\varphi_{m,j} - \varphi_{m,m}}{\pi}\right), \tag{4.18}$$

where Rnd(x) is the closest integer to x. Now, let us find an expression for ΔL, which was defined previously as the length that produces a phase shift of $2\pi/N$ between two adjacent wavelength channels. If n_e represents the effective index of the mode of an array guide and n_{e0} denotes the value of n_e at the center wavelength λ_0, then the effective index

Table 4.3 Wavelength assignment of a five-channel MMI-phasar multiplexer. A 5 × 5 WDM interconnection is possible.

Output (k)	Input (i)				
	1	2	3	4	5
1	λ_{-1}	λ_2	λ_1	λ_0	λ_{-2}
2	λ_2	λ_0	λ_{-1}	λ_{-2}	λ_1
3	λ_1	λ_{-1}	λ_{-2}	λ_2	λ_0
4	λ_0	λ_{-2}	λ_2	λ_1	λ_{-1}
5	λ_{-2}	λ_1	λ_0	λ_{-1}	λ_2

value at the neighboring channel, $\lambda_0 + \Delta\lambda$, is given by $n_{e0} + \Delta\lambda \frac{dn_e}{d\lambda}$. An expression for ΔL can be written as follows:

$$\Delta L = \rho \frac{\lambda_0}{n_{e0}} = \left(\rho - \frac{1}{N}\right) \frac{\lambda_0 + \Delta\lambda}{n_{e0} + \Delta\lambda \frac{dn_e}{d\lambda}}, \tag{4.19}$$

where ρ is a real number. By eliminating ρ from (4.19), ΔL can be rewritten as

$$\Delta L = \frac{\lambda_0(\lambda_0 + \Delta\lambda)}{N\Delta\lambda\left(n_{e0} - \lambda_0 \frac{dn_e}{d\lambda}\right)}. \tag{4.20}$$

By substituting for ΔL from (4.20) into (4.18), we get

$$A_{m,j,m} = \text{Rnd}\left(\frac{d_j n_{e0}(\lambda_0 + \Delta\lambda)}{N\Delta\lambda\left(n_{e0} - \lambda_0 \frac{dn_e}{d\lambda}\right)} - \frac{\varphi_{m,j} - \varphi_{m,m}}{\pi}\right). \tag{4.21}$$

Thus, one can determine the arm length L_j by combining (4.17) and (4.21).

Similar expressions can be derived for the multiplexer structure of Figure 4.1(b). For this structure, the value of an arm length L_j is given by

$$L_j - L_m = \left(A_{j,m} + \frac{\varphi'_j + \varphi_{j,m} - \varphi'_m - \varphi_{m,m}}{2\pi}\right)\frac{\lambda_0}{n_{e0}}, \tag{4.22}$$

where φ and φ' are given by (2.58) and (2.77), respectively, and $A_{j,m}$ is an integer expressed as

$$A_{j,m} = \text{Rnd}\left(\frac{d_j n_{e0}(\lambda_0 + \Delta\lambda)}{N\Delta\lambda\left(n_{e0} - \lambda_0 \frac{dn_e}{d\lambda}\right)} - \frac{\varphi'_j + \varphi_{j,m} - \varphi'_m - \varphi_{m,m}}{2\pi}\right). \tag{4.23}$$

Now we have the means required for designing an MMI-phasar multiplexer with any number of channels. In the following section, we examine the actual design and the performance of a five-channel multiplexer. Before leaving this section, however, we would like to point out another interesting property of MMI-phasar devices. It can be seen from Equations (4.17)–(4.23) that the lengths of the array arms relate to the ratio λ_0 / n_{e0} so that the lengths of the arms would not change as long as this ratio is kept constant. An important consequence of this property is that the fabrication and the operational tolerances would not affect the spectral response of the MMI-phasar multiplexers other than shifting the response.

4.3 Five-Channel Multiplexers

A five-channel MMI-phasar multiplexer with 2-nm channel spacing at 1.55-μm wavelength was designed in the SiO_2–SiON rib waveguide described in Chapter 3. The five wavelength channels used in the design have been placed from 1546 to 1554 nm. The free spectral range of the multiplexer is 10 nm, which is well within the optical bandwidth of the MMI couplers. The values of various design parameters are listed in Table 4.4. Three device variations, associated with the three general multiplexer structures that have been examined in this chapter, are considered. First, we need to know the optimum set of values of the array arm factor d_j. This set has been determined already for the five-channel multiplexers with layouts similar to those of Figure 4.1 and is given in row $N = 5$ of Table 4.2. Similarly, for the five-channel multiplexer with a layout similar to that of Figure 4.2, an optimum set of d_j values can be easily found by applying the procedure described in the previous section to the case of $m = 1$; the optimum set for this multiplexer structure is $\{0, 2, 3, 4, 6\}$ corresponding to $\{d_1, \ldots, d_5\}$. It is seen that, in this case, $d_j^{\max} = 6$, which is larger than $d_j^{\max} = 4$ of the other two structures. Consequently, we expect the spectral response of the more physically compact five-channel multiplexer with $m = 1$ to be poorer than those of the other two multiplexers.

Table 4.4 Various parameters of the designed five-channel multiplexers.

Description	Value
Number of channels, N	5
Channel spacing, $\Delta\lambda$	2 nm
Center wavelength, λ_0	1550 nm
Free spectral range	10 nm
ΔL, as given by (4.20)	158.87 μm
Effective refractive index of the array guides, n_{e0}	1.4772

Furthermore, we need to find a 1 × 5 MMI nonuniform power splitter with a suitable output power distribution. As discussed in Section 4.1, output power distribution of the nonuniform power splitter should be such that the relative portion of power distributed to an array guide gradually increases with the value of the array arm factor d_j and then gradually decreases. This reduces the sidelobe levels in the multiplexer spectral response. We know, from the analysis in Chapter 2, that the power in the output guides of a $1 \times N$ MMI power splitter depends on the parameters h_1, h_2, and N'. An appropriate set of values of these parameters, which are restricted by (2.74), have to be determined. Using (2.76) and (2.74), all possible output power distributions of a 1 × 5 MMI power splitter were examined and the values of $h_1 = 7$, $h_2 = 1$, and $N' = 10$ were selected. The power distribution of this 1 × 5 MMI power splitter, as calculated by (2.76), is shown in Figure 4.3. It should be noted that the 5 × 5 MMI coupler and the 1 × 5 nonuniform power splitter employed in the design of the five-channel multiplexers are the same five-port MMI couplers that were studied in Chapter 3.

To simplify our design, the same bends were used in all the array guides, and the length difference between the array arms was introduced only in the straight sections of the arms. Figures 4.4(a) and 4.4(b) show the layouts of the five-channel multiplexers that

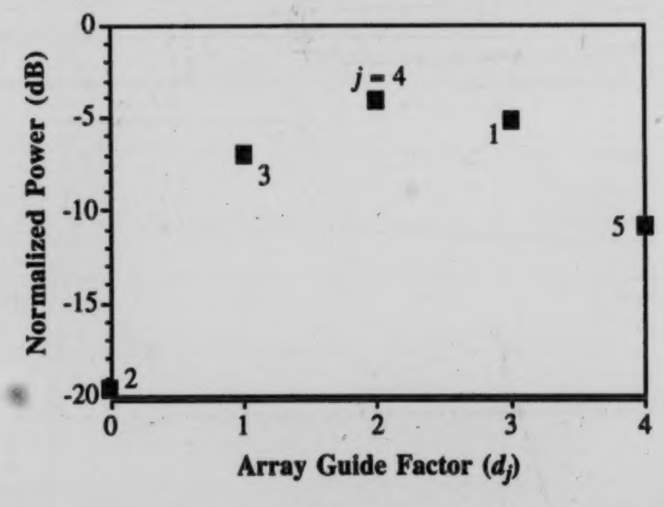

Figure 4.3 Normalized output power distribution of a 1 × 5 MMI nonuniform power splitter versus the array guide factor (d_j). The number next to each symbol indicates the corresponding output j.

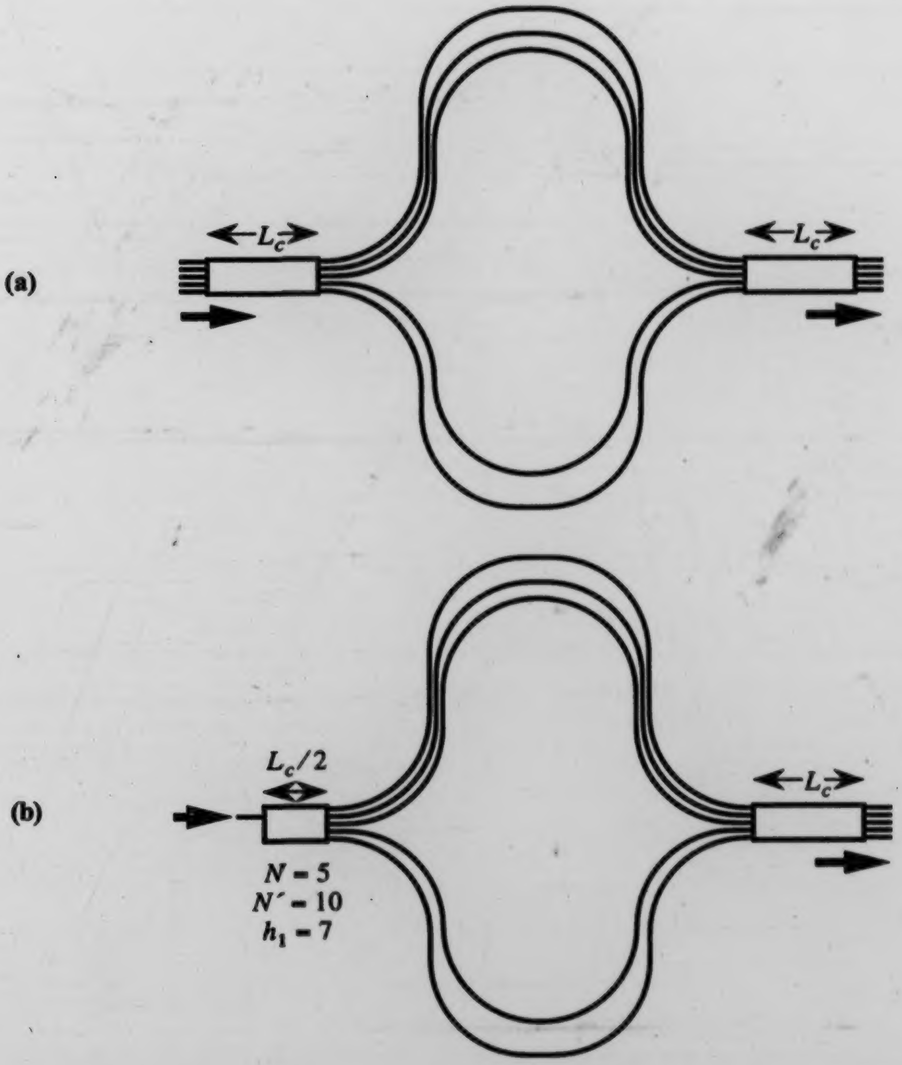
(a)
L_c
L_c
(b)
$L_c/2$
$N = 5$
$N' = 10$
$h_1 = 7$
L_c

Figure 4.4 Layouts of the five-channel MMI-phasar multiplexers with the optimized set of values d_j: (a) with a 5 × 5 MMI coupler as the power splitter, (b) with a 1 × 5 MMI nonuniform power splitter.

correspond to the general device structures of Figure 4.1. In both cases, the length difference between the longest and the shortest arms is about 636 μm. With a bending radius of 0.5 mm, which has a negligible bending loss, the total device size would be around 4×2.6 mm. Figure 4.5 depicts the layout of the five-channel multiplexer that corresponds to the general structure of Figure 4.2. The length difference between the longest and the shortest arms of this multiplexer is about 954 μm. With a bending radius of 0.5 mm, a total device size of approximately 2×1.1 mm is obtained.

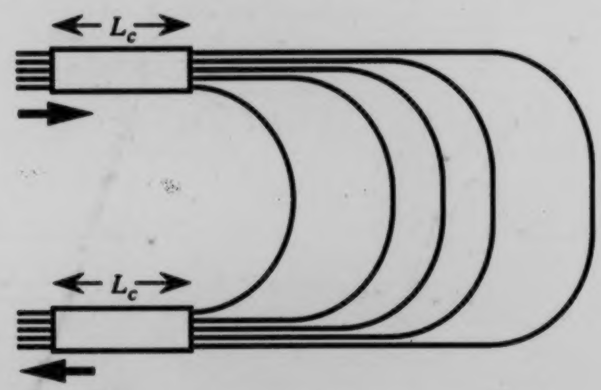

Figure 4.5 Layout of the five-channel MMI-phasar multiplexer in which the shortest array guide is the first arm ($m = 1$).

The spectral response of each multiplexer was evaluated using modal propagation simulation of the MMI couplers and introducing phase delays corresponding to the relative lengths of the array arms. Also, the two multiplexers depicted in Figure 4.4 were fabricated, and their spectral transmission was measured using the experimental arrangement shown previously in Figure 3.15. The waveguide structure of our single-mode array guides does not have zero birefringence and, consequently, the multiplexers are expected to be polarization sensitive. The results are presented for the TE polarization only.

The spectral response of the multiplexer of Figure 4.4(a) is shown in Figure 4.6, where high uniformity among different channels is observed. The measured spectral response of the multiplexer has shifted by about +1 nm from the modeled response. An insertion loss of 1.5 dB, and a worst-case crosstalk of –10 dB in a 0.5-nm-wide window are achieved. The 1-dB full width is about 1.1 nm. The measured crosstalk is nearly 6 dB worse than its simulated counterpart (–16 dB). The surface roughness of the waveguides and any defects along the guides result in residual phase errors in the array arms and prevent the total constructive or destructive interference behavior of the device; this is the main cause of the overall degradation of the measured spectral response as compared to the simulated performance [71]. To verify the wavelength-routing properties of the MMI-phasar multiplexer of Figure 4.4(a), the spectral response of all routes of the device were examined and the wavelength assignment given already in Table 4.3 were observed.

The spectral response of the multiplexer of Figure 4.4(b) is illustrated in Figure 4.7. As expected, the sidelobe levels have decreased to a considerable extent. On average, the sidelobes in the spectral response depicted in Figure 4.7 are more than 10 dB lower than those of Figure 4.6. The measured insertion loss is around 2 dB. The mainlobe has widened and this results in increased crosstalk from the nearest neighboring channel.

The simulated spectral transmission of the multiplexer of Figure 4.5 is shown in Figure 4.8. Compared with that of Figure 4.6(a), a degradation of the spectral response is clearly observed in this case, because the value of d_j^{max} for this multiplexer structure is larger than that for the structure of Figure 4.4(a).

By comparing Figures 4.6(a), 4.7(a), and 4.8, one can observe that the dips in the spectral response of Figure 4.7(a) are located where the peaks of the lobes in the other two responses occur. By cascading the spectral transmission of Figure 4.7(a) with one of the other two spectral transmissions, we can expect a great improvement of the overall performance. Figure 4.9 shows the simulated spectral response of a cascaded configuration of the two multiplexers of Figures 4.4(b) and 4.5. The combined loss is about 3 dB, and the sidelobes are down by more than 32 dB.

A number of steps can be taken to improve the measured performance of the device and to narrow the gap between the experimental and the modeled spectral transmissions. The surface roughness of the waveguides has to be reduced to limit the propagation losses and, more importantly, to decrease the residual phase error in the array arms. This can be done by modifying the etching process [17], and/or by using an upper cladding in the waveguide structure. Also, the polarization sensitivity of these multiplexers can be reduced by using a waveguide structure which has zero birefringence.

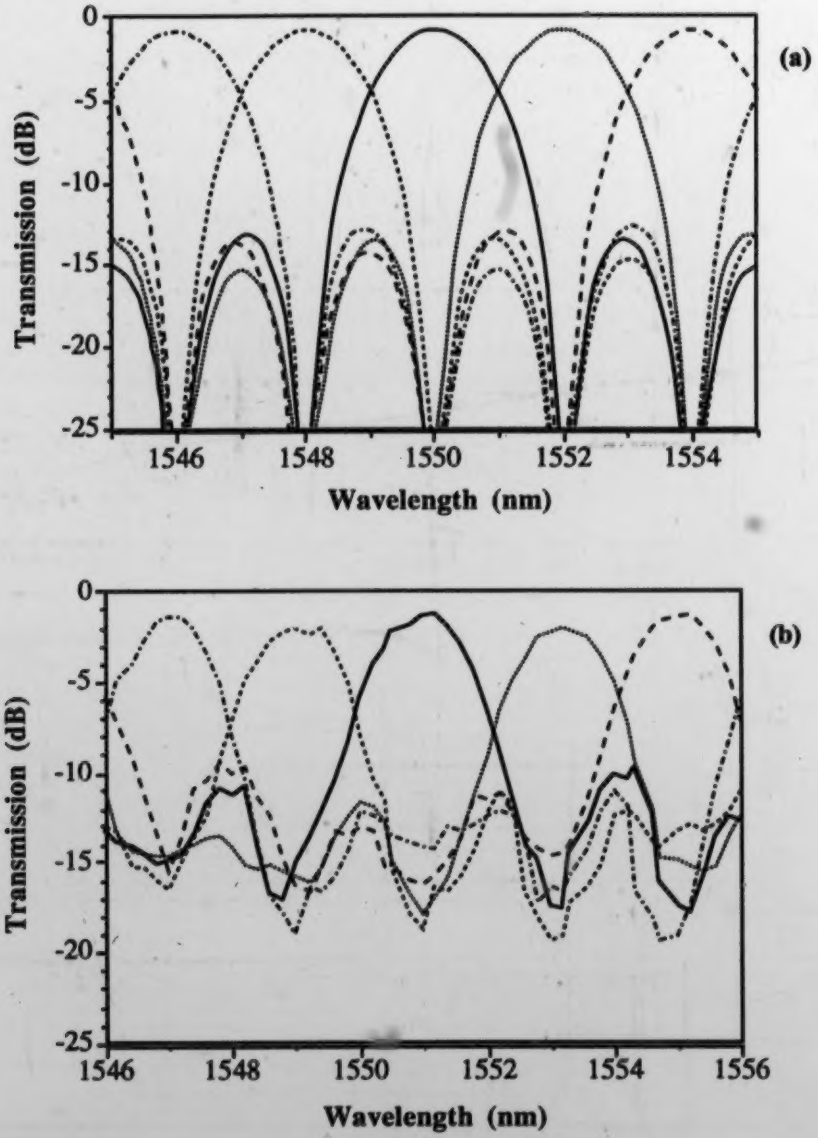

Figure 4.6 Spectral response of the multiplexer of Figure 4.4(a). The response of all five routes associated with one input guide are shown only. The routes originating from other inputs have similar transmissions. (a) Simulated performance. (b) Measured response.

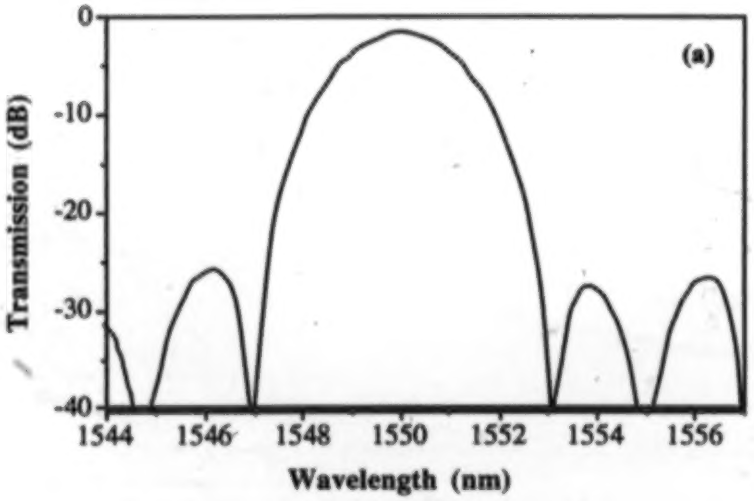

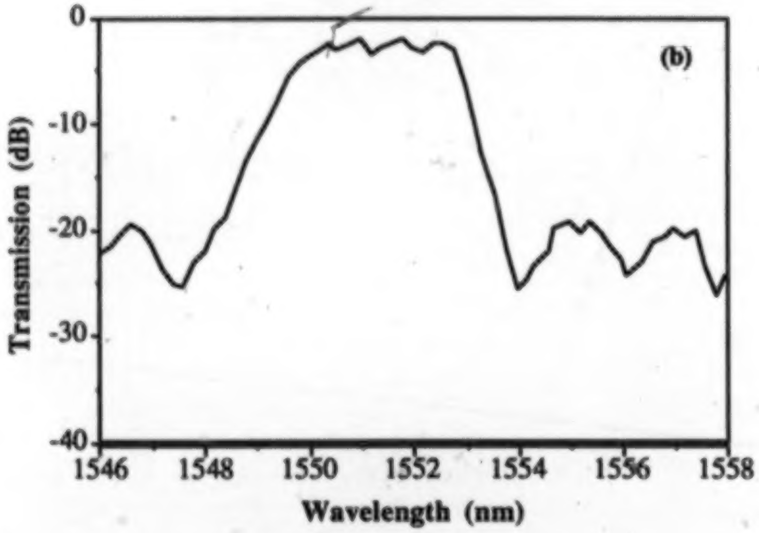

Figure 4.7 Spectral response of the multiplexers of Figure 4.4(b); the transmission at only one output guide is displayed. Other routes behave similarly. (a) Simulated performance. (b) Measured response.

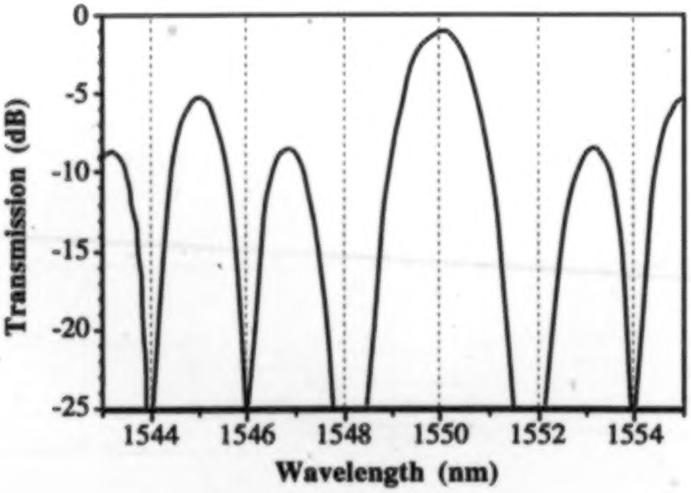

Figure 4.8 Simulated spectral response of the multiplexer of Figure 4.5; the response of only one route is displayed.

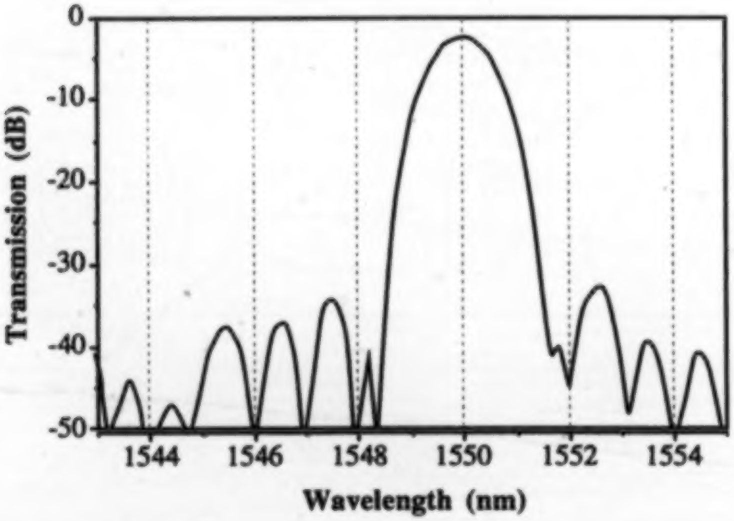

Figure 4.9 Expected spectral response of a combined configuration of multiplexers of Figures 4.4(b) and 4.5. Only one channel is shown.

The effects of the fabrication tolerances on the performance of the five-channel multiplexers were also investigated. A ±5-μm change in the optimal lengths of both couplers increases the overall loss of the multiplexer by only 0.5 dB; otherwise, the spectral response would be largely unaffected. Variation of the waveguide dimensions and of the refractive-index values of the waveguide material alters the effective index value of the mode of an array waveguide and, consequently, shifts the multiplexer spectral response in wavelength. For example, a 0.01% change in the refractive index of the waveguide core material (SiON) shifts the multiplexer spectral response by 0.12 nm, without increasing the insertion loss.

The MMI-phasar devices possess functionalities that could make them suitable for a number of interesting WDM-related applications. Two such applications will be examined in the next two sections.

4.4 Application as Dynamic Wavelength Routers

Wavelength routers direct the optical signals with different wavelengths to separate destinations and are key components for WDM optical networks. Wavelength routers can be classified into two types: static routers having a fixed wavelength permutation and dynamic routers that can reconfigure the wavelength permutation on demand. The most well-known static wavelength router is the arrayed-waveguide grating (AWG) multiplexer discussed in Chapter 1; wavelength tuning can be done with this device by altering the temperature of the substrate but individual phase control and independent routing change for each wavelength is not possible.

We showed that the wavelength-routing characteristics of the MMI-phasar devices enable them to operate as $N \times N$ WDM interconnecting components. An MMI-phasar device, which is basically a static wavelength router, can be converted to a dynamic wavelength router by simply including phase shifters on the array arms, as shown in Figure 4.10. Then any of the N wavelength channels can be routed from a given input port to any output port. The number of the array arms of the MMI-phasar device is small enough that allows the phase shifters placed on the arms to be independently controlled; this fact gives a clear advantage to the MMI-phasar devices over the AWG multiplexers for re-configurable wavelength-routing applications. The device of Figure 4.10 is a promising candidate for applications in wavelength add-drop multiplexing and

WDM cross-connect switching. This device can also function as a tunable wavelength demultiplexer.

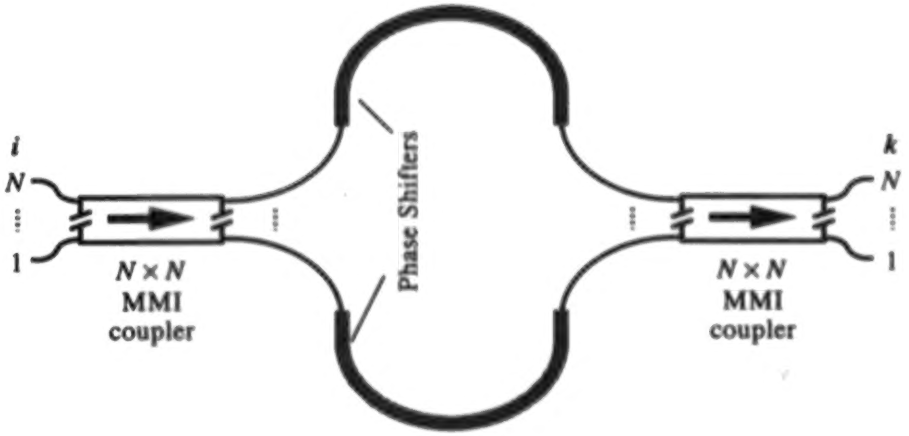

Figure 4.10 Layout of an MMI-phasar WDM cross-connect switch.

4.5 MMI-phasar for Multiwavelength Laser Applications

Multiwavelength lasers that are based on the integration of wavelength-selective filters and optical amplifiers are attractive components for wavelength-division multiplexing systems. The AWG multiplexers have been employed as intra-cavity filters in multiwavelength lasers [47]–[50]. The possibility of using an MMI-phasar device instead of the AWG multiplexer in multiwavelength lasers is intriguing. Here, the application of MMI-phasar multiplexers in multiwavelength lasers is studied.

Figure 4.11 shows the schematic diagram of a multiwavelength laser incorporating an MMI-phasar device. The *N* ports at one end of the multiplexer terminate in optical amplifiers with cleaved mirror facets, and one port at the other end terminates in a partially reflected mirror, or possibly an additional optical amplifier. Each of the *N* resonant cavities supports a different wavelength due to the wavelength-routing properties of the MMI-phasar device. These intracavity filters are precisely spaced with respect to each other, resulting in an output consisting of *N* stable and accurately spaced laser wavelengths.

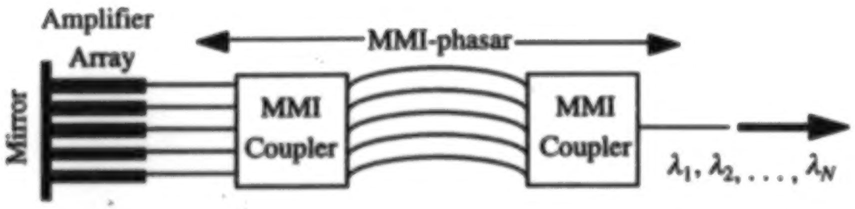

Figure 4.11 Schematic diagram of a multifrequency laser incorporating the MMI-phasar multiplexer as an intra-cavity filter.

The design of multiwavelength lasers requires several trade-offs. First, one would like to have the filter bandwidth of the intracavity filter as narrow as possible. A narrow filter bandwidth guarantees that the laser locks on a single longitudinal Fabry-Perot mode, regardless of how many longitudinal modes are contained within that filter bandwidth [47]. On the other hand, the free spectral range (FSR) of the multiplexer should be large so that the selectivity of the amplifier gain profile is sufficient to choose lasing in only one order of the multiplexer. Since the spacing of Fabry-Perot modes is inversely proportional to the device length, the multiplexer used in the multiwavelength laser configuration should have a small size to secure single-mode stability. The MMI-phasar devices are generally more compact than the AWG multiplexers and, therefore, they are more advantageous in this regard than their AWG counterparts. The design of a 12-channel MMI-phasar multiplexer [70] suitable for multiwavelength laser applications is discussed next.

4.5.1 A Twelve-Channel Multiplexer

The layout of the 12-channel MMI-phasar multiplexer is shown in Figure 4.12. As before, an optimum set of values of the array arm factor d_j was found using the procedure described in Section 4.3; this set is {15, 10, 8, 5, 1, 0, 6, 7, 11, 14, 16, 21} corresponding to $\{d_1, \ldots, d_{12}\}$. This 12-channel multiplexer is of the same general family of multiplexer structures shown in Figure 4.1(b). The MMI nonuniform power splitter employed in the structure of the 12-channel multiplexer is intended to increase the sidelobe rejection by providing a suitable weight distribution among the array guides. An appropriate set of values of the parameters h_1, h_2, and N' of the 1×12 MMI power splitter were determined after examining all possible output power distributions of the MMI splitter using (2.76) and (2.74). The parameter values of $N' = 26$, $h_1 = 22$, and $h_2 = 2$ were selected.

The 12-channel multiplexer was designed, with 1-nm channel spacing at the center wavelength of 1550 nm, in a deeply-etched InP/InGaAsP rib waveguide system. The wavelength channels have been placed from 1545 to 1556 nm. The 12 × 12 MMI coupler is 46 μm wide and 1480 μm long. The 1 × 12 MMI splitter is 49.8 μm wide and 805 μm long. The array guides and the input/output access guides are 2 μm wide, and ΔL is 61.3 μm. The same waveguide bends are used in the array arms; see Figure 4.12. Using a bending radius of 200 μm, the total size of the multiplexer would be approximately 2 × 3.2 mm.

The spectral transmission of the multiplexer was evaluated using the modal propagation analysis of the MMI couplers and introducing phase delays corresponding to the relative lengths of the array arms. Figure 4.13(a) shows the response of the center channel of the multiplexer. The multiplexer has a periodic transmission with a free

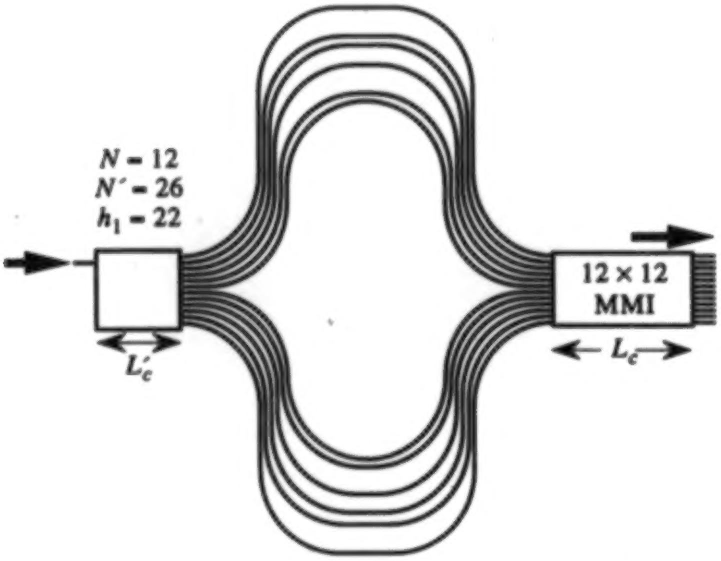

Figure 4.12 Layout of the 12-channel MMI-phasar multiplexer. Parameters h_1 and N' of the 1 × 12 MMI nonuniform power splitter are as described in the text.

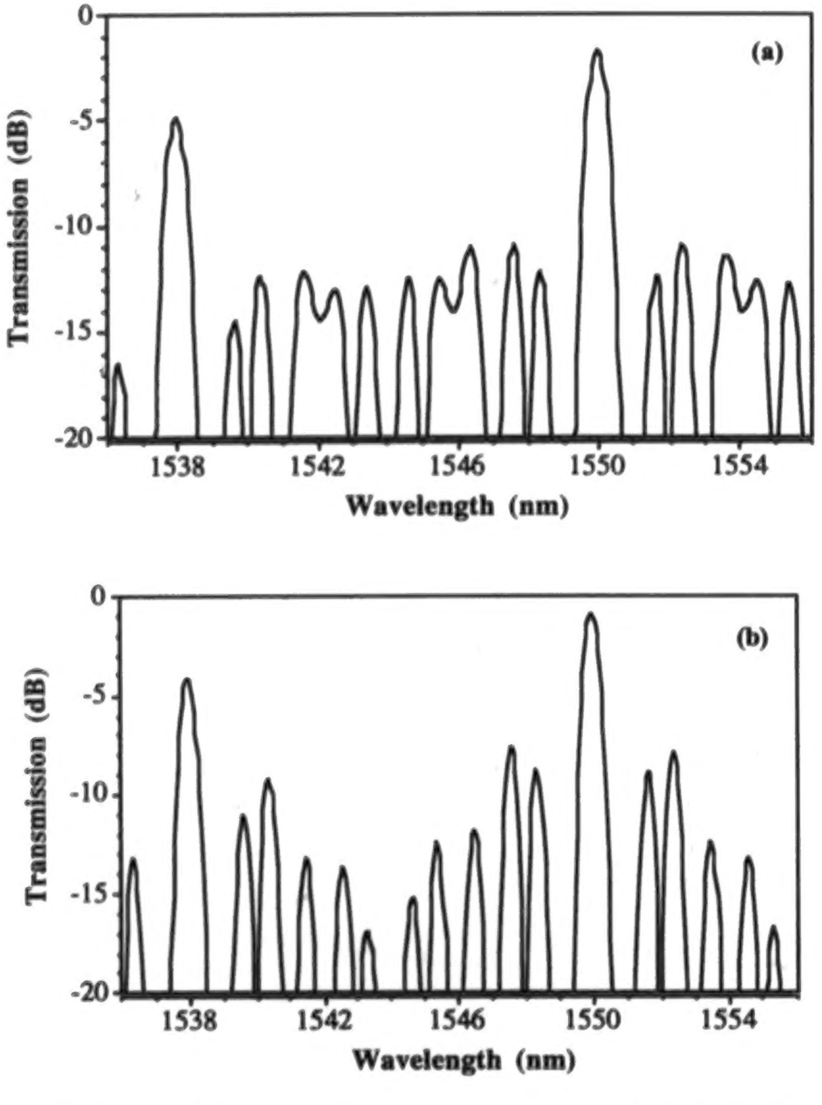

Figure 4.13 Simulated spectral response of the 12-channel MMI-phasar multiplexer. The transmission of only the center channel is displayed. Other channels have similar transmissions, except for appropriate wavelength shifts of integer multiples of the channel spacing (1 nm). (a) With nonuniform power splitter as depicted in Figure 4.12, (b) with equal power splitting.

spectral range of 12 nm. The loss at the center wavelength is 1.7 dB, and the 1-dB full width is about 0.32 nm. A transmission uniformity of better than 0.8 dB among all the channels was observed. The sidelobes in Figure 4.13(a) are down by at least 9.5 dB. For comparison purposes, the spectral transmission of an MMI-phasar multiplexer with uniform power splitting is depicted in Figure 4.13(b); it is seen that the sidelobe levels in this case are relatively high. The worst-case sidelobes in Figure 4.13(a) are about 2.8 dB lower than the sidelobes in Figure 4.13(b).

To control the lasing wavelength in multiwavelength lasers, the multiplexer response should be sufficiently suppressed at the undesired orders. As displayed in Figure 4.13, the response at the adjacent order at 1538 nm is suppressed by nearly 3.2 dB compared with that at the center wavelength. This is due to the limited operating bandwidth of the 12-port MMI couplers. For wavelength channels, which are positioned farther from the center wavelength of the multiplexer, the difference between the multiplexer transmission at the passband wavelength and its neighboring order will be smaller. Hence, absolute wavelength control can be expected only for channels located close to the center wavelength. Notwithstanding, this shortcoming can be overcome by chirping the lengths of the array guides, thereby destroying the periodicity of the multiplexer spectral response [50].

5. MMI Couplers for Broadly-Spaced Dual-Channel Wavelength Demultiplexing

Integrated devices that achieve (de)multiplexing of two broadly-separated wavelengths are needed for many applications. For example, as illustrated previously in Figure 1.6, rare-earth doped waveguide amplifiers and lasers require the combination and separation of pump and signal light [72]–[74]. Also, the transceivers in local-area optical networks may use 1.3/1.55-μm wavelength multiplexers. Several devices can perform this multiplexing function [74]–[78]. Conventional directional couplers [74], and unbalanced Mach-Zehnder interferometers [75] are generally characterized by relatively long devices. Composite asymmetric Y-branches [76] employ asymmetry in the refractive index profile and require a two-mask fabrication process. Two-mode interference couplers implemented in diffused waveguides have been utilized to build dual-channel wavelength multiplexers [77]. Also, a novel technique was recently demonstrated which uses two-mode interference in a short bent coupler to achieve demultiplexing of two broadly separated wavelengths [78].

MMI couplers can also perform dual-channel wavelength multiplexing if one wavelength is in the bar-coupled state and the other is cross coupled. This is possible because the beat length of MMI couplers, as expressed by Equation (2.29), is wavelength dependent. Generally, the length of the MMI couplers used for wavelength multiplexing could be too long because the wavelength-sensitivity of MMI couplers is relatively low, but if the wavelengths of interest are on the order of a few hundreds of nanometers apart, fairly small size demultiplexing couplers can be designed.

It was described in Section 2.3.1 that MMI couplers have the property that they are in bar and cross-coupled states at lengths equal to even and odd multiples of $3L_\pi$, respectively. An MMI coupler can separate the two wavelengths λ_1 and λ_2 if it is a bar-coupler for one wavelength and a cross-coupler for the other wavelength; the length (L_c) of the demultiplexing coupler has to satisfy the following relation:

$$\begin{aligned} L_c &= p(3L_\pi^{\lambda_1}) \\ &= (p+q)(3L_\pi^{\lambda_2}) \, , \end{aligned} \tag{5.1}$$

where p is a positive integer, q is an odd integer, and L_π^λ is the beat length at wavelength λ. The coupler length has to be minimized since a short coupler is desirable for the purpose of integration and for reducing propagation losses. Moreover, as described in Chapter 3, fabrication tolerances become more relaxed and polarization sensitivity decreases as the coupler gets shorter. From (5.1), the ratio of the two beat lengths is given by

$$\text{Beat Length Ratio} = L_\pi^{\lambda_1} / L_\pi^{\lambda_2} = (p+q)/p. \tag{5.2}$$

We know, from Equation (2.29), that the beat lengths of the two wavelengths and, consequently, the beat length ratio depend on the coupler width, so we should choose a coupler width that results in the beat length ratio being in the form of $(p+q)/p$ with the smallest possible coupler length.

Next, we demonstrate a compact 980/1550 nm (pump/signal) wavelength (de)multiplexer useful for integration with rare-earth doped waveguide amplifiers and lasers [79]–[81]. The device operates both as a multiplexer or a demultiplexer with the direction of light propagation reversed from one configuration to the other. We concentrate on the demultiplexing configuration here. It is shown that the device performance can be optimized by careful selection of the waveguide parameters, and in particular, the coupler width.

5.1 Compact 980/1550-nm Wavelength Demultiplexer

The 980/1550-nm wavelength demultiplexer was designed and implemented in the SiO_2–SiON rib waveguide system described in Chapter 3. The refractive indices of SiO_2 and SiON films were 1.465/1.46 and 1.565/1.561, respectively, at 980/1550-nm wavelengths. This layer structure (SiO_2–SiON) is compatible with several hybrid integrated optical circuits in glass [82]. Also, SiON has been used in a number of rare-earth doped waveguide amplifiers [83]–[85]. Spontaneous emission and transmitted signal enhancement were reported in an amplifier made with a highly erbium-doped glass sputtered film combined with a SiON strip-loading layer [83]. The photoluminescent characteristics of deep high-dose erbium implantation in low-loss SiON waveguides were studied and it was predicted that SiON could be considered as a promising material for integrated optical amplifiers and lasers [84], [85].

Using the FWave 2D mode-solver, the beat lengths of the two wavelengths were evaluated for several values of the coupler width. The ratio of TE beat lengths of the two wavelengths as a function of the coupler width is plotted in Figure 5.1. The ratio is about 1.5 at a coupler width of 6 μm; this beat length ratio corresponds to $p = 2$ and $q = 1$ in Equation (5.2).

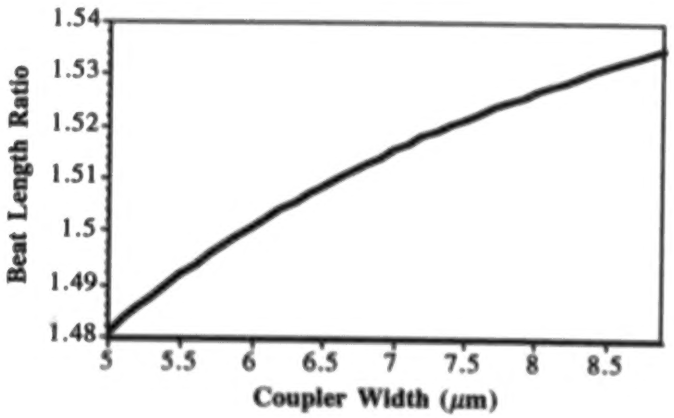

Figure 5.1 Calculated beat length ratio (L_π^{980}/L_π^{1550}) as a function of the MMI coupler width; TE polarization. A ratio of 1.5 (3/2) is predicted at a width of about 6 μm.

The basic layout of the 980/1550 nm demultiplexing coupler is shown in Figure 5.2. The coupler is in bar and cross-coupled states at 980-nm and 1550-nm wavelengths, respectively. The coupler length is $L_c = 6L_\pi^{980} = 9L_\pi^{1550}$. The MMI coupler is 6-$\mu m$ wide and supports five and two modes at 980- and 1550-nm wavelength, respectively. The widths of the input guide, bar-output guide (pump channel) and the cross-output guide (signal channel) are 3, 2.3 and 3 μm, respectively. The input guide supports two modes at 980 nm and is single-moded at 1550 nm. The gap size at the junction tip between the output guides is 0.7 μm. Figure 5.3 shows a SEM picture of the output junction of a fabricated coupler.

Transmission characteristics of the device were found using the modal propagation analysis. The light intensity pattern in the demultiplexer is depicted in Figure 5.4.

Contrast and insertion loss are used as measures of performance of the device. Referring to Figure 5.2, the contrast and insertion loss at 980-nm wavelength are defined as

$$
\begin{aligned}
\text{Contrast} &= 10\,\mathrm{Log}\left(P_2^{980}/P_3^{980}\right), \\
\text{Insertion Loss} &= -10\,\mathrm{Log}\left(P_2^{980}/P_1^{980}\right).
\end{aligned}
\tag{5.3}
$$

The expressions related to the 1550-nm wavelength are defined in a similar manner.

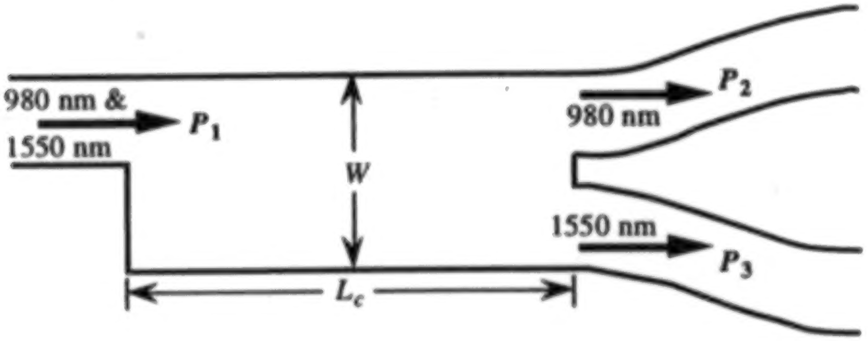

Figure 5.2 Top view of the demultiplexing coupler. 980-nm wavelength is in bar-coupled state and 1550 nm is cross-coupled. The widths of the multimode section, input guide, top and bottom output guides are 6, 3, 2.3 and 3 μm, respectively.

3,80KX 20KV WD:16MM S:00000 P:00000
10UM

Figure 5.3 A SEM picture of the 0.7 μm gap at the output junction of the MMI demultiplexing coupler.

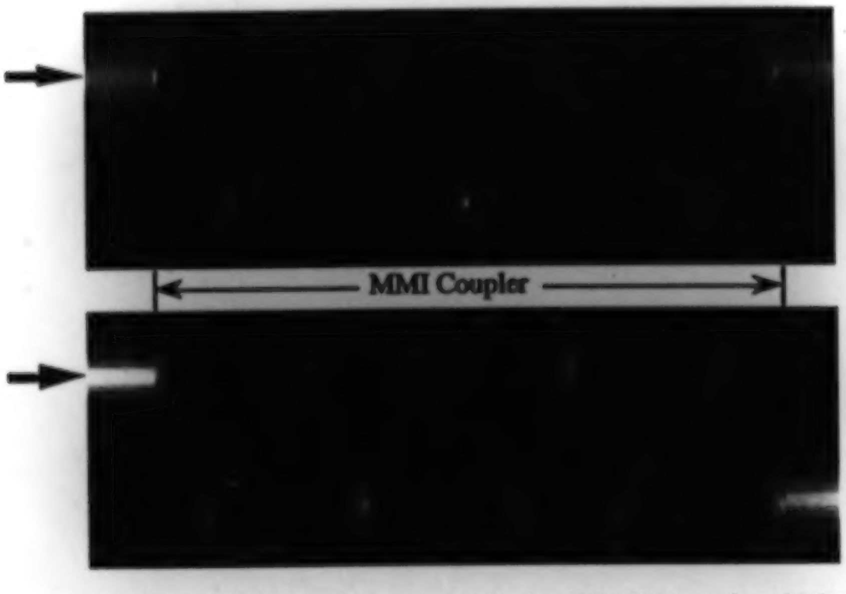

Figure 5.4 Simulated light intensity pattern in the 980/1550 nm demultiplexing coupler. The upper and lower pictures represent the 980- and 1550-nm wavelength, respectively.

Assuming a symmetric input field excitation, the power in the first order mode of 980-nm wavelength in the input guide is ignored. The simulated TE performance of the demultiplexer as a function of the coupler length is shown in Figure 5.5. Insertion losses below 1 dB at both wavelengths, and contrasts of 24 dB at 980 nm and 15 dB at 1550 nm are predicted at an optimum coupler length of 467 μm.

The devices were fabricated with the coupler length varying in steps of 5 μm around its optimum value. A 0.1-μm variation in the width of our demultiplexing coupler results in a change of 14 μm in its optimal length, so tight control during photolithography was required to minimize the width variations. Compact *S*-bends were used to provide a separation of 250 μm between the output access guides. To measure the insertion losses, reference waveguides were included alongside each device.

The experimental arrangement depicted in Figure 5.6, which is similar to that shown formerly in Figure 3.9, was used to measure the performance of the 980/1550-nm wavelength demultiplexer. Contrast of about 18 dB and insertion loss of 0.5 dB at both wavelengths were achieved with an optimum coupler length of 458 μm; see Figure 5.7. The device performance at 1550 nm is better than the theoretical evaluations; this can be attributed to the contribution of leaky modes or a possible third mode in the multimode interference section. The contrast at 980 nm is a few dB lower than that predicted theoretically which could be because there is some power in the first order mode of 980 nm in the input waveguide. The optimum coupler length is lower by a few microns than its calculated value; this can be expected if the actual coupler width is slightly smaller than its nominal value of 6 μm.

TM beat lengths of the demultiplexing coupler were calculated to be larger than their TE counterparts by 3 μm and 5 μm at 980 nm and 1550 nm, respectively. This means that optimum values of the coupler width and length are different for each of the two polarizations, and our 6-μm wide demultiplexing coupler has been optimized for TE polarization only. In principle, as stated in Chapter 3, by setting the coupler width and length at intermediate values, polarization-independent operation can be obtained at the expense of a performance degradation. Furthermore, the waveguide structure can be modified to make the coupler less polarization-sensitive. In the next section, we will examine a polarization-insensitive 980/1550-nm wavelength demultiplexer [81].

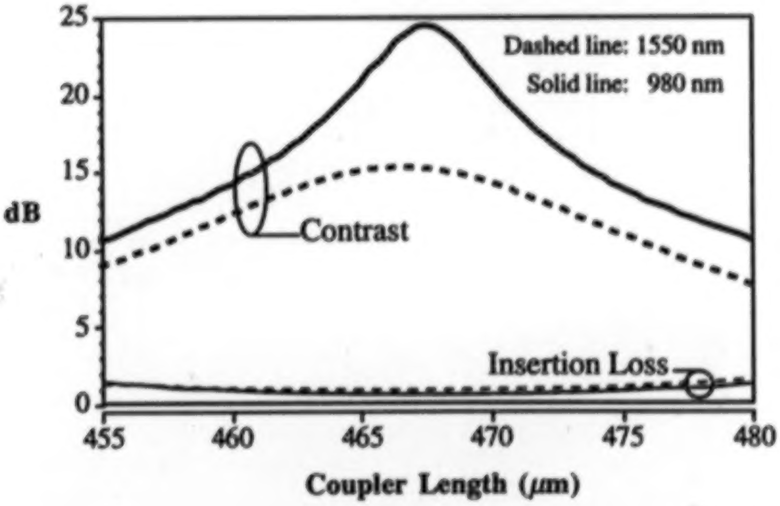

Figure 5.5 Simulated TE performance of the MMI demultiplexing coupler as a function of the coupler length (L_c). The multimode section is 6-μm wide.

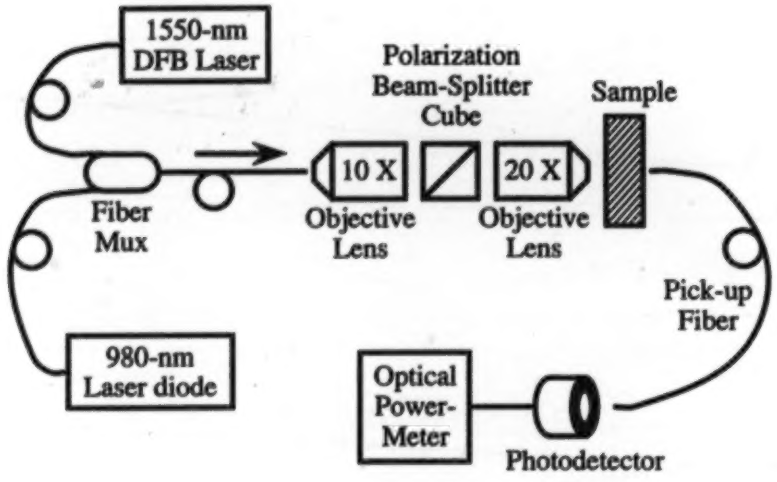
1550-nm
DFB Laser
Polarization
Beam-Splitter
Cube
Sample
10 X
20 X
Fiber
Mux
Objective
Lens
Objective
Lens
Pick-up
Fiber
980-nm
Laser diode
Optical
Power-
Meter
Photodetector

Figure 5.6 Schematic diagram of the experimental arrangement used for testing the 980/1550-nm wavelength demultiplexer.

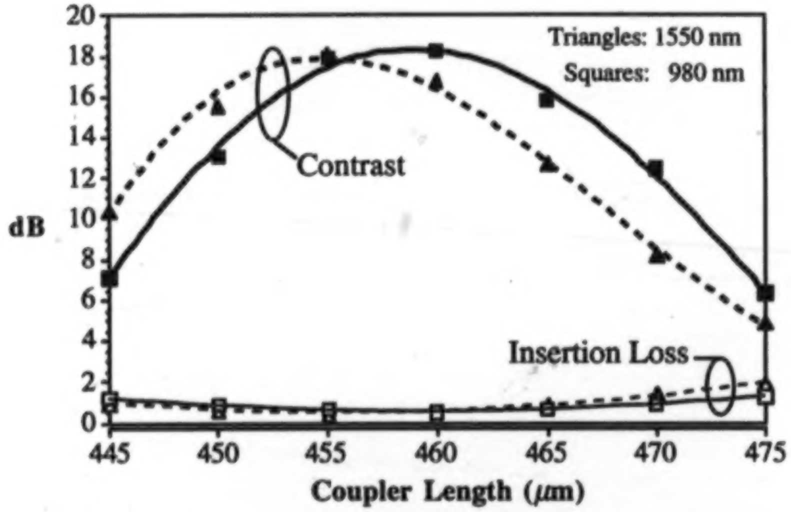

Figure 5.7 Measured TE performance of the fabricated devices with coupler length (L_c) varying in steps of 5 μm. The multimode section is 6-μm wide. Thin lines are quadratic curve fits and thick lines are fourth degree polynomial fits.

5.2 Polarization-Insensitive 980/1550-nm Wavelength Demultiplexer

The SiO_2–SiON rib waveguide structure was modified to design a polarization-insensitive 980/1550-nm wavelength demultiplexer. As shown Figure 5.8, the modified rib structure consists of SiO_2 buffer and upper-cladding layers, and a partially-etched SiON core. The refractive indices of the films are the same as before. It has been shown in [64] that SiON is almost free from stress around the index value of 1.55. Hence, any stress-induced birefringence can be safely ignored in the design.

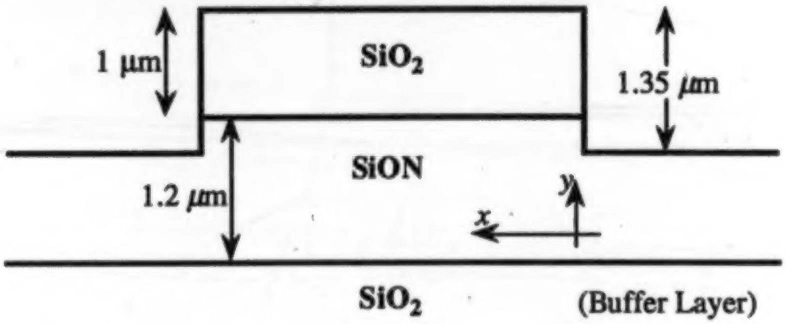

Figure 5.8 Cross-section of the rib waveguide structure for the polarization-insensitive MMI demultiplexing coupler.

The beat lengths of the two wavelengths for both polarizations were evaluated for several values of the coupler width. It is assumed that the dominant component of electric field for quasi-TE, and the dominant component of magnetic field for quasi-TM, are along the *x*-axis as depicted in Figure 5.8. The ratio of TE beat lengths of the two wavelengths as a function of the coupler width is plotted in Figure 5.9. Also, the beat length difference of the two polarizations ($L_{\pi,\mathrm{TM}} - L_{\pi,\mathrm{TE}}$) is illustrated in Figure 5.9. It can be seen that the polarization sensitivity is minimal for both wavelengths at a coupler width of about 6 μm, while the beat length ratio is equal to 1.5 at a coupler width of 7 μm. As a compromise, an MMI coupler with a width of 6.5 μm was selected. This coupler supports four and three modes at 980- and 1550-nm wavelength, respectively. The input/output access guides are 2.8-μm wide; they are single-moded at 1550 nm and support two modes at 980 nm.

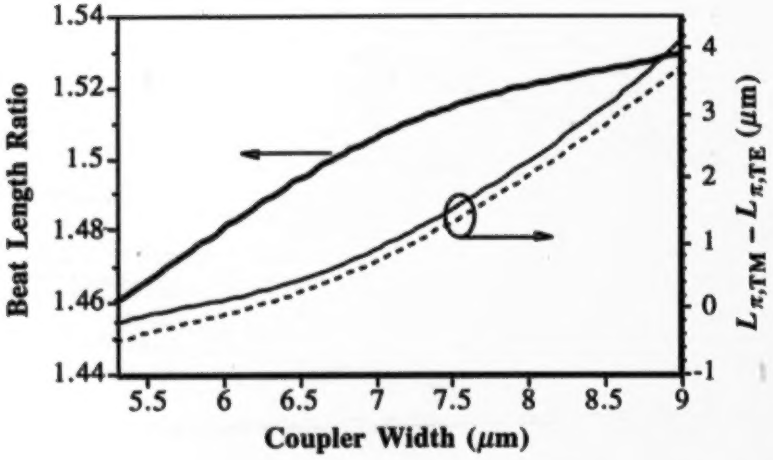

Figure 5.9 Beat length ratio as a function of the MMI coupler width (TE polarization). Also, the beat length difference of the two polarizations ($L_{\pi,TM} - L_{\pi,TE}$) is shown for both wavelengths; thin solid line and thin dashed line relate to 980 nm and 1550 nm, respectively.

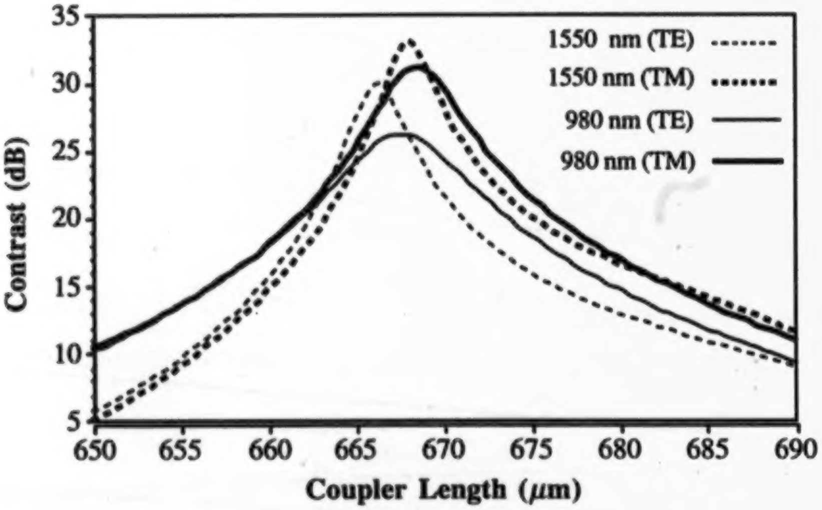

Figure 5.10 Modeled performance of the polarization-insensitive 980/1550 nm demultiplexing coupler as a function of the coupler length (L_c). The MMI coupler is 6.5-μm wide.

The contrast of the demultiplexing coupler as a function of the coupler length is shown in Figure 5.10. As expected, the shift between TE and TM curves is very small. Contrasts of more than 25 dB at both wavelengths and for both polarizations are predicted at a coupler length of 667 μm. The calculated insertion losses for all cases were below 0.5 dB at the optimum coupler length.

Fabrication tolerances of the coupler were also investigated. With a limit of 15-dB contrast, variations of up to ±9 μm in the coupler length can be tolerated. A 0.1 μm variation in the etch depth will result in a change of only 2.5 μm in the optimal length of the coupler, while a 0.1 μm variation in the coupler width will shift its optimal length by about 20 μm. Both of these fabrication variations have negligible effect on the device performance as far as the insensitivity to polarization is concerned. The tolerance of the width of the MMI coupler is much tighter in this case because the coupler is longer.

6. Summary and Conclusion

This thesis has been mainly concerned with the design and development of WDM devices using MMI couplers. A summary of the major parts of the work and the corresponding results are presented in this section.

MMI couplers have emerged as a new class of optical components that can provide multi-port coupling and splitting with a compact size, low loss, and high uniformity. These features together with their ease of fabrication and their relaxed tolerances, have led to the rapid incorporation of the MMI couplers in complex photonic integrated circuits. Splitting and combining of multiple optical beams is an important function in integrated optics, and MMI couplers can perform this function efficiently. MMI couplers have a definite role to play in the future of integrated optics.

The full characteristics of MMI couplers have been well understood only during last few years. In fact, the complete self-imaging characteristics of general $N \times N$ MMI couplers, which are important components in the design of MMI-phasar multiplexers and generalized Mach–Zehnder switches, were analytically described only recently [9], [10]. In this work, we have taken full advantage of the properties of MMI couplers in the design of novel WDM components.

A modal propagation analysis was developed to simulate the light propagation in MMI couplers. The self-imaging mechanism in general $N \times N$ MMI couplers is completely described by this analysis. Simple analytical expressions that relate the coupler geometry to image intensities, phases, and positions were derived. We saw that different variations of MMI couplers such as 3-dB coupler, cross coupler, and overlapping-image coupler can be simply considered as special cases of $N \times N$ MMI couplers. Overlapping-image MMI couplers, which allow both uniform and nonuniform power splitting, were examined and special attention was paid to the design of $1 \times N$ power splitters.

Our devices have been implemented in a PECVD SiO_2–SiON rib waveguide system on silicon substrates. Various steps involved in the fabrication procedure were described. The most critical parameter to control during the fabrication is the width of couplers since the optimal length of MMI couplers is highly sensitive to variations of the coupler width. By tight control during photolithography processing, an accuracy of ±0.1 μm in the width of the fabricated waveguides, with respect to the dimensions of the photomask features, was repeatably achieved.

To verify the theory of MMI couplers, a 5×5 MMI coupler and a 1×5 nonuniform power splitter were designed and fabricated. The couplers were relatively short; about 708 μm and 354 μm for the 5×5 MMI coupler and the 1×5 splitter, respectively. The measured transmission loss of the 5×5 coupler indicated that the coupler had an average insertion loss of nearly 0.3 dB and a uniformity of better than 1 dB among its outputs. Also, the 1×5 splitter exhibited an average measured insertion loss of about 0.3 dB. The transmission measurements of the couplers were in good agreement with the simulation results.

The tolerances of MMI couplers were studied, and analytical expressions, which can estimate the effect of tolerances on the device performance, were presented. The fabrication tolerances and the optical bandwidth of the five-port MMI couplers were measured. With a limit of 0.5 dB excess losses, fabrication tolerances of $\delta L_c = \pm 6$ μm corresponding to $\delta W_e = \pm 0.14$ μm were obtained for the 5×5 coupler, while measured optical bandwidths of more than 30 nm and 50 nm were achieved for the 5×5 coupler and the 1×5 splitter, respectively. It was demonstrated that MMI couplers have the advantage of maintaining a very good output uniformity or balance over a large range of fabrication and operational variations. The polarization dependence of MMI couplers was also discussed, and it was noted that polarization-insensitive MMI couplers can be designed by choosing a waveguide structure so that the beat lengths for the two polarizations are equal. The five-port MMI couplers implemented in the SiO_2–SiON rib waveguide exhibited a small polarization-dependent penalty loss.

We have demonstrated novel designs of phased-array wavelength multiplexers, which incorporate two MMI couplers interconnected by an array of N monomode waveguides. A general theoretical analysis of MMI-phasar multiplexers was presented, and a simple procedure for finding an optimum set of lengths for the array guides was given. With the design methodology we have presented, it is possible to optimize the multiplexer spectral performance while at the same time organize the layout for compactness and the avoidance of crossings and minimization of bends in the waveguide array. It was shown that wavelength-routing properties of MMI-phasar multiplexers enabled them to operate as $N \times N$ wavelength-selective interconnecting components. It was also demonstrated that, by using a $1 \times N$ MMI nonuniform power splitter, tap weight tapering in the multiplexer could be used to suppress the spectral sidelobes.

Two variations of a 5-channel multiplexer with 2-nm channel spacing at 1550-nm wavelength were designed and fabricated. The spectral response of these multiplexers revealed high uniformity among channels. An insertion loss of 1.5 dB and a worst-case crosstalk of –10 dB in a 0.5-nm-wide spectral window were measured. The modeled performance predicts a worst-case crosstalk of –16 dB in the same spectral window. Smoother waveguide sidewalls are expected to reduce the phase errors in the array arms and to improve the performance of the multiplexers. It was shown that by cascading the 5×5 multiplexer and a 1-to-5 device optimized for sidelobe rejection, integrated multiplexers with low crosstalk could be built.

Application of the MMI-phasar in WDM cross-connect switches was discussed. An MMI-phasar device can be converted to a dynamic wavelength router by simply including phase shifters on the array arms. For this particular application, the MMI-phasar has a definite advantage over the arrayed-waveguide grating multiplexer since the number of array arms of the MMI-phasar is comparatively much smaller.

A 12-channel MMI-phasar multiplexer with potential applications in multiwavelength lasers was proposed and analyzed. Calculated transmission of the device designed in a InP/InGaAsP rib waveguide system indicated an insertion loss of 1.7 dB and a transmission uniformity of better than 0.8 dB among all channels. The multiplexer has a length of only 3.2 mm. Using a suitable 1×12 MMI nonuniform power splitter in the multiplexer structure, the sidelobe suppression ratio was improved by about 2.8 dB.

A compact high performance 980/1550-nm wavelength multiplexer useful for integration with rare-earth doped waveguide amplifiers and lasers was demonstrated. The operation of this multiplexer is based on wavelength-selective coupling in MMI couplers. It was shown that the device performance can be optimized with a right choice of the coupler width. The experimental results of the multiplexer supported the theoretical predictions. Contrast of about 18 dB and insertion loss of 0.5 dB at both wavelengths were achieved with an optimum coupler length of only 458 μm. It was also demonstrated that a polarization-insensitive multiplexer can be obtained by choosing the waveguide parameters appropriately.

6.1 Future Work

To continue the work performed in this thesis, further investigation in a number of areas will be suggested. The experimental performance of our designed devices can be improved by making some modifications in the waveguide structure and/or the fabrication process.

In Chapter 4, the surface roughness of the waveguides was identified as the main cause of the overall degradation of the measured spectral response of the MMI-phasar multiplexers. The waveguide surface roughness results in residual phase errors in the array arms, and also increases the propagation losses. The surface roughness of the waveguides can be decreased by using a modified RIE process as described in [17]. The effect of the waveguide surface roughness can be further reduced by adding an upper cladding in the rib waveguide system.

Some work would be needed to address the polarization sensitivity of the devices. The response of the MMI-phasar multiplexers is polarization-dependent mainly due to the birefringence of the array arms. One way to reduce the polarization sensitivity of the MMI-phasar multiplexers is to use a waveguide structure that has zero birefringence. Also, it was observed in Chapter 5 that a polarization-insensitive 980/1550 nm demultiplexing coupler can be obtained with a right choice of the waveguide structure so that the beat lengths corresponding to the two polarizations are equal.

It was mentioned in Chapter 3 that PECVD SiON films suffer from high absorption losses in the wavelength range 1.5-1.55 μm caused by the N-H resonance absorptions. These losses can be largely reduced by annealing the films at temperatures around 1000 °C but in many application, annealing at such high temperatures is not desirable from the integration viewpoint. Moreover, annealing causes some changes in the film parameters, and increases the number of steps in the fabrication process. This problem can be totally avoided if nitrogen-containing source materials are not used in the PECVD deposition process. Then the films would contain no nitrogen and would be free from losses associated with the N-H resonance absorptions. For example, a PECVD process was recently reported [86] that used oxygen as an alternative to nitrous oxide as an oxidant, and fluorine as the refractive index-varying dopant. The propagation losses of channel waveguides formed in these silica-based films were reported to be less than 0.2 dB/cm in the 1.5-1.55-μm wavelength range. Further research in similar PECVD processes for fabricating suitable low-loss films would definitely lead to devices with very low insertion losses.

It was indicated that MMI-phasar multiplexers could be used in applications such as multiwavelength lasers and dynamic wavelength routers. It is necessary to implement and test some of these devices to verify the suitability of MMI-phasar multiplexers for these applications. The wavelength-routing properties of MMI-phasar multiplexers might make them suitable for applications that are not obvious at the present time but may show up in the future. Also, it would be desirable to try to incorporate components such as Bragg gratings in the design of MMI-phasar multiplexers to improve the spectral response of the multiplexers [87]. This could be an engaging research area in the future.

References

[1] C. A. Brackett, "Dense wavelength division multiplexing networks: principles and applications," *J. Selected Areas Commun.*, vol. 8, pp. 948–964, 1990.

[2] C. Dragone, C. H. Henry, I. P. Kaminow, and R. C. Kistler, "Efficient multichannel integrated optics star coupler on silicon," *IEEE Photon. Technol. Lett.*, vol. 1, no. 8, pp. 241–243, 1989.

[3] R. Ardar, C. H. Henry, R. F. Kazarinow, R. C. Kistler, and G. R. Weber, "Adiabatic 3-dB couplers, filters, and multiplexers made with silica waveguide on silicon," *J. Lightwave Technol.*, vol. 10, no. 9, pp. 46–50, 1992.

[4] H. Yamagawa, S. Nakamura, I. Ohyama, and K. Ueki, "Broad-band high-silica optical waveguide star coupler with asymmetrical directional coupler," *J. Lightwave Technol.*, vol. 8, no. 9, pp. 1292–1297, 1990.

[5] O. Bryngdahl, "Image formation using self-imaging techniques," *J. Optical Soc. Amer.*, vol. 63, no. 4, pp. 416–419, 1973.

[6] R. Ulrich and G. Ankele, "Self-imaging in homogeneous planar optical waveguides," *Appl. Phys. Lett.*, vol. 27, no. 6, pp. 337–339, 1975.

[7] R. Ulrich, "Image formation by phase coincidences in optical waveguides," *Opt. Commun.*, vol. 13, no. 3, pp. 259–264, 1975.

[8] L. B. Soldano, F. B. Veerman, M. K. Smit, B. H. Verbeek, A. H. Dubost, and E. C. M. Pennings, "Planar monomode optical couplers based on multimode interference effects," *J. Lightwave Technol.*, vol. 10, no. 12, pp. 1843–1850, 1992.

[9] M. Bachmann, P. A. Besse, and H. Melchior, "General self-imaging properties in $N \times N$ multimode interference couplers including phase relations," *Appl. Opt.*, vol. 33, no. 18, pp. 3905–3911, 1994.

[10] M. Bachmann, P. A. Besse, and H. Melchior, "Overlapping-image multimode interference couplers with a reduced number of self-images for uniform and nonuniform power splitting," *Appl. Opt.*, vol. 34, no. 30, pp. 6898–6910, 1995.

[11] P. A. Besse, M. Bachmann, H. Melchior, L. B. Soldano, and M. K. Smit, "Optical bandwidth and fabrication tolerances of multimode interference couplers," *J. Lightwave Technol.*, vol. 12, no. 6, pp. 1004–1009, 1994.

[12] E. C. M. Pennings, R. van Roijen, M. J. N. van Stralen, P. J. de Waard, R. G. M. P. Koumans, and B. H. Verbeek, "Reflection properties of multimode interference devices," *IEEE Photon. Technol. Lett.*, vol. 6, no. 6, pp. 715–718, 1994.

[13] E. C. M. Pennings, R. J. Deri, A. Scherer, R. Bhat, T. R. Hayes, N. C. Andreadakis, M. K. Smit, L. B. Soldano, and R. J. Hawkins, "Ultracompact, low-loss directional couplers on InP based on self-imaging by multimode interference," *Appl. Phys. Lett.*, vol. 59, pp. 1926–1928, 1991.

[14] J. M. Heaton, R. M. Jenkins, D. R. Wight, J. T. Parker, J. C. H. Birbeck, and K. P. Hilton, "Novel 1-to-*N* way integrated optical beam splitters using symmetric mode mixing in GaAs/A1GaAs multimode waveguides," *Appl. Phys. Lett.*, vol. 61, no. 15, pp. 1754–1756, 1992.

[15] A. Ferreras, F. Rodrígues, E. Gómez-Salas, J. L. de Miguel, and F. Hernández-Gil, "Useful formulas for multimode interference power splitter/combiner design," *IEEE Photon. Technol. Lett.*, vol. 5, no. 10, pp. 1224–1227, 1993.

[16] M. Bouda, J. W. M. van Uffelen, C. van Dam, and B. H. Verbeek, "Compact 1 × 16 power splitter based on symmetrical 1 × 2 MMI splitters," *Electron. Lett.*, vol. 30, no. 21, pp. 1756–1757, 1994.

[17] L. H. Spiekman, Y. S. Oei, E. G. Metaal, F. H. Groen, I. Moerman, and M. K. Smit, "Extremely small multimode interference couplers and ultrashort bends on InP by deep etching," *IEEE Photon. Technol. Lett.*, vol. 6, no. 8, pp. 1008–1010, 1994.

[18] T. J. Tayag, D. M. Mackie, and G. W. Bryant, "A manufacturable technique for implementing low-loss self-imaging waveguide beamsplitters," *IEEE Photon. Technol. Lett.*, vol. 7, no. 8, pp. 896–898, 1995.

[19] T. Rasmussen, J. K. Rasmussen, and J. H. Povlsen, "Design and performance evaluation of 1-by-64 multimode interference power splitter for optical communications," *J. Lightwave Technol.*, vol. 13, no. 10, pp. 2069–2074, 1995.

[20] C. M. Weinert and N. Agrawal, "Three-dimensional finite difference simulation of coupling behavior and loss in multimode interference couplers," *IEEE Photon. Technol. Lett.*, vol. 7, no. 5, pp. 529–531, 1995.

[21] Q. Lai, M. Bachmann, W. Hunziker, P. A. Besse, and H. Melchior, "Arbitrary ratio power splitters using angled silica on silicon multimode interference couplers," *Electron. Lett.*, vol. 32, no. 17, pp. 1576–1577, 1996.

[22] P. A. Besse, E. Gini, M. Bachmann, and H. Melchior, "New 2 × 2 and 1 × 3 multimode interference couplers with free selection of power splitting ratios," *J. Lightwave Technol.*, vol. 14, no. 10, pp. 2286–2293, 1996.

[23] L. B. Soldano and E. C. M. Pennings, "Optical multi-mode interference devices based on self-imaging: principles and applications," *J. Lightwave Technol.*, vol. 13, no. 4, pp. 615–627, 1995.

[24] F. Tian, Ch. Harizi, H. Hermann, V. Reimann, R. Ricken, U. Rust, W. Sohler, F. Whermann, and S. Westenhöfer, "Polarization-independent integrated optical, acoustically tunable double-stage wavelength filter in $LiNbO_3$," *J. Lightwave Technol.*, vol. 12, no. 7, pp. 1192–1197, 1994.

[25] R. J. Deri, E. C. M. Pennings, A. Scherer, A. S. Gozdz, C. Caneau, N. C. Andreadakis, V. Shah, L. Curtis, R. J. Hawkins, J. B. D. Soole, and J.-I. Song, "Ultracompact monolithic integration of balanced, polarization diversity

photodetectors for coherent lightwave receivers," *IEEE Photon. Technol. Lett.*, vol. 4, no. 11, pp. 1238–1240, 1992.

[26] R. van Roijen, E. C. M. Pennings, M. J. N. van Stralen, T. van Dongen, B. H. Verbeek, and J. M. N. van der Heijden,"Compact InP-based ring lasers employing multimode interference couplers and combiners," *Appl. Phys. Lett.*, vol. 64, no. 14, pp. 1753–1755, 1994.

[27] R. M. Jenkins, J. M. Heaton, D. R. Wight, J. T. Parker, J. C. H. Birbeck, G. W. Smith, and K. P. Hilton, "Novel $1 \times N$ and $N \times N$ integrated optical switches using self-imaging multimode GaAs/A1GaAs waveguides," *Appl. Phys. Lett.*, vol. 64, no. 6, pp. 684–686, 1994.

[28] M. Bachmann, Ch. Nadler, P. A. Besse, and H. Melchior, "Compact polarization-insensitive multi-leg 1 × 4 Mach-Zehnder switch in InGaAsP/InP," in *Proceedings of the European Conference on Optical Communication*, (Istituto Internationale delle comunicazioni, Genova, Italy, 1994), pp. 519–522.

[29] R. Krähenbühl, W. Vogt, W. Hunziker, H. Schneibel, R. Bauknecht, E. Gini, and H. Melchior, "Low-loss polarization-insensitive high-speed InP/InGaAsP optical space switch modules fully packaged with electronic drivers and single-mode fibers," in *Proceedings of Photonics in Switching Conference*, Stokholm, Sweden, 1997, pp. 154–157.

[30] J. Leuthold, R. Hess, J. Eckner, P. A. Besse, and H. Melchior, "Spatial mode filters realized with multimode interference couplers," *Opt. Lett.*, vol. 21, no. 11, pp. 836–838, 1996.

[31] J. B. D. Soole, A. Scherer, H. P. LeBlanc, N. C. Andreadakis, M. A. Koza, and R. Bhat, "Monolithic InP/InGaAsP/InP grating spectrometer for the 1.48-1.56 μm wavelength range," *Appl. Phys. Lett.*, vol. 58, pp. 1949–1951, 1991.

[32] K. R. Poguntke, J. B. D. Soole, H. P. LeBlanc, N. C. Andreadakis, P. Grabbe, R. Bhat, C. Caneau, and M. A. Koza, "High-performance InP reflection-grating wavelength multiplexer," *Electron. Lett.*, vol. 30, no. 6, pp. 512–513, 1994.

[33] F. N. Timofeev, P. Bayvel, E. G. Churin, and J. E. Midwinter, "1.5 μm free-space grating multi/demultiplexer and routing switch," *Electron. Lett.*, vol. 32, no. 14, pp. 1307–1308, 1996.

[34] E. Acosta and K. Iga, "Design of a wavelength multiplexer-demultiplexer by the use of planar microlenses," *Appl. Opt.*, vol. 33, no. 16, pp. 3415–3419, 1994.

[35] M. Shirasaki, "Large angular dispersion by a virtually imaged phased array and its application to a wavelength demultiplexer," *Opt. Lett.*, vol. 21, no. 5, pp. 366–368, 1996.

[36] B. H. Verbeek, C. H. Henry, N. A. Olsson, K. J. Orlowsky, R. F. Kazarinov, and B. H. Johnson, "Integrated four-channel Mach–Zehnder multi/demultiplexer fabricated

with phosphorous doped SiO_2 waveguides on Si," *J. Lightwave Technol.*, vol. 6, no. 6, pp. 1011–1015, 1988.

[37] N. Takato, T. Kominato, A. Sugita, K. Jinguji, H. Toba, and M. Kawachi, "Silica-based integrated optic Mach–Zehnder multi/demultiplexer family with channel spacing of 0.01–250 nm," *IEEE J. on Selected areas in Comm.*, vol. 8, no. 6, pp. 1120–1127, 1990.

[38] C. Dragone, and C. A. Edwards, and R. C. Kistler, "Integrated optics $N \times N$ multiplexer on Silicon," *IEEE Photon. Technol. Lett.*, vol. 3, no. 10, pp. 896–899, 1991.

[39] M. Zirngibl, C. Dragone, and C. H. Joyner, "Demonstration of a 15×15 arrayed waveguide multiplexer on InP," *IEEE Photon. Technol. Lett.*, vol. 4, no. 11, pp. 1250–1253, 1992.

[40] H. Takahashi, S. Suzuki, and I. Nishi, "Wavelength multiplexer based on SiO_2–Ta_2O_5 arrayed-waveguide grating," *J. Lightwave Technol.*, vol. 12, no. 6, pp. 989–995, 1994.

[41] H. Takahashi, K. Oda, H. Toba, and Y. Inoue, "Transmission characteristics of arrayed waveguide $N \times N$ wavelength multiplexer," *J. Lightwave Technol.*, vol. 13, no. 3, pp. 447–455, 1995.

[42] B. H. Verbeek, A. A. M. Staring, E. J. Jansen, R. van Roijen, J. J. M. Binsma, T. van Dongen, M. R. Amersfoort, C. van Dam, and M. K. Smit, "Large bandwidth polarization independent and compact 8 channel PHASAR demultiplexer/filter," in *Optical Fiber Communication Conference*, vol. 4 of 1994 OSA Technical Digest Series (Optical Society of America, Washington, D.C., 1994), pp. PD13-1–PD13-4.

[43] H. Bissessur, P. Pagnod-Rossiaux, R. Mestric, and B. Martin, "Extremely small polarization independent phased-array demultiplexer on InP," *IEEE Photon. Technol. Lett.*, vol. 8, no. 4, pp. 554–556, 1996.

[44] B. Glance, "Wavelength-tunable add/drop optical filter," *IEEE Photon. Technol. Lett.*, vol. 8, no. 2, pp. 245–247, 1996.

[45] B. Glance, I. P. Kaminow, and R. W. Wilson, "Applications of the integrated waveguide grating router," *J. Lightwave Technol.*, vol. 12, no. 6, pp. 957–961, 1994.

[46] N. J. Frigo, P. P. Iannone, P. D. Magill, T. E. Darcie, M. M. Downs, B. *N.* Desai, U. Koren, T. L. Koch, C. Dragone, H. M. Presby, and G. E. Bodeep, "A wavelength-division multiplexed passive optical network with cost-shared components," *IEEE Photon. Technol. Lett.*, vol. 6, no. 11, pp. 1365–1367, 1994.

[47] M. Zirngibl, B. Glance, L. W. Stulz, C. H. Joyner, G. Raybon, and I. P. Kaminow, "Characterization of a multiwavelength waveguide grating router laser," *IEEE Photon. Technol. Lett.*, vol. 6, no. 9, pp. 1082–1084, 1994.

[48] M. Zirngibl, C. H. Joyner, C. R. Doerr, L. W. Stulz, and H. M. Presby, "An 18-channel multifrequency laser," *IEEE Photon. Technol. Lett.*, vol. 8, no. 7, pp. 870–872, 1996.

[49] A. A. M. Staring, L. H. Spiekman, J. J. M. Binsma, E. J. Jansen, T. van Dongen, P. J. A. Thijs, M. K. Smit, and B. H. Verbeek, "A compact nine-channel multiwavelength laser," *IEEE Photon. Technol. Lett.*, vol. 8, no. 9, pp. 1139–1141, 1996.

[50] C. R. Doerr, C. H. Joyner, M. Zirngibl, and L. W. Stulz, "Chirped waveguide grating router multifrequency laser with absolute wavelength control," *IEEE Photon. Technol. Lett.*, vol. 8, no. 12, pp. 1606–1608, 1996.

[51] N. S. Kapany and J. J. Burke, *Optical Waveguides*, Academic Press, N.Y., 1972.

[52] R. G. Hunsperger, *Photonic Devices and Systems*, Marcel Dekker, N.Y., 1994.

[53] W. V. McLevige, T. Itoh, and R. Mittra, "New waveguide structures for millimeter-wave and optical integrated circuits," *IEEE Transactions on Microwave Theory and Techniques*, vol. MTT-23, no. 10, pp. 788–794, 1975.

[54] K. S. Chiang, "Dual effective-index method for the analysis of rectangular dielectric waveguides," *Appl. Opt.*, vol. 25, no. 13, pp. 2169–2174, 1986.

[55] A. Kumar, D. F. Clark, and B. Culshaw, "Explanation of errors inherent in the effective-index method for analyzing rectangular-core waveguides," *Opt. Lett.*, vol. 13, no. 12, pp. 1129–1131, 1988.

[56] K. S. Chiang, "Performance of the effective-index method for the analysis of dielectric waveguides," *Opt. Lett.*, vol. 16, no. 10, pp. 714–716, 1991.

[57] P. C. Kendall, M. J. Adams, S. Ritchie, and M. J. Robertson, "Theory for calculating approximate values for the propagation constant of an optical rib waveguide by weighting the refractive indices," *IEE Proceedings*, vol. 134, Pt. A, no. 8, pp. 699–702, 1987.

[58] C. F. Janz, *Ph.D. Thesis*, University of Alberta, 1995.

[59] M. Taylor, *Fwave: two-dimensional mode solver*, public domain, 1995.

[60] K. Chandrasekharan, *Introduction to Analytic Number Theory*, (pp. 34–44), Springer-Verlag, Berlin, 1968.

[61] H. J. Lee, C. H. Henry, R. F. Kazarinov, and K. J. Orlowsky, "Low loss Bragg reflectors on SiO_2–Si_3N_4–SiO_2 rib waveguides," *Appl. Opt.*, vol. 26, no. 13, pp. 2618–2620, 1987.

[62] C. H. Henry, R. F. Kazarinov, H. J. Lee, K. J. Orlowsky, and L. E. Katz, "Low loss Si_3N_4–SiO_2 optical waveguides on Si," *Appl. Opt.*, vol. 26, no. 13, pp. 2621–2624, 1987.

[63] H. Bezzaoui and E. Voges, "Integrated optics combined with micromechanics on silicon," *Sensors and Actuators A*, no. 29, pp. 219–223, 1991.

[64] K. Fischer and J. Müller, "Sensor application of SiON integrated optical waveguides on silicon," *Sensors and Actuators B*, no. 9, pp. 209–213, 1992.

[65] D. S. Walker, W. M. Reichert, and C. J. Berry, "Corning 7059, silicon oxynitride, and silicon dioxide thin-film integrated optical waveguides: in search of low loss, nonfluorscent, reusable glass waveguides," *Applied Spectroscopy*, vol. 46, no. 9, pp. 1437–1441, 1992.

[66] C. van Dam, M. R. Amersfoort, G. M. ten Kate, F. P. G. M. van Ham, M. K. Smit, P. A. Besse, M. Bachmann, and H. Melchior, "Novel InP-based phased-array wavelength demultiplexer using a generalized MMI-MZI configuration," in *Proceedings of the ECIO'95*, (Delft University Press, Delft, The Netherlands, 1995), pp. 275–278.

[67] L. O. Lierstuen and A. Sudbø, "8-channel wavelength division multiplexer based on multimode interference couplers," *IEEE Photon. Technol. Lett.*, vol. 7, no. 9, pp. 1034–1036, 1995.

[68] M. R. Paiam and R. I. MacDonald, "Design of phased-array wavelength division multiplexers using multimode interference couplers," *Appl. Opt.*, vol. 36, no. 21, pp. 5097–5108, 1997.

[69] M. R. Paiam and R. I. MacDonald, "Planar phased-array wavelength multiplexers based on multimode interference couplers," in *Proceedings of the SPIE'97*, vol. 3007, (SPIE, Bellingham, Washington, 1997), pp. 104–111.

[70] M. R. Paiam and R. I. MacDonald, "A 12-channel phased-array wavelength multiplexer with multimode interference couplers," Submitted to *Photon. Technol. Letters*.

[71] S. Lin, W. Feng, J. C. Powelson, R. J. Feuerstein, L. J. Bintz, D. Tomic , and A. R. Mickelson, "Scattering induced crosstalk in active directional couplers," *J. Lightwave Technol.*, vol. 14, no. 9, pp. 2012–2025, 1996.

[72] R. N. Ghosh, J. Shmulovich, C. F. Kane, M.R.X. de Barros, G. Nykolak, A. J. Bruce, and P. C. Becker, "8-mW threshold Er^{3+}-doped planar waveguide amplifier," *IEEE Photon. Technol. Lett.*, vol. 8, no. 4, pp. 518–520, 1996.

[73] T. Kitagawa, K. Hattori, Y. Hibino, Y. Ohmori, and M. Horiguchi, "Laser oscillation in Er-doped silica-based planar ring resonator," in *Proceedings ECOC* 1992, pp. 907–910.

[74] K. Hattori, T. Kitagawa, M. Oguma, Y. Ohmori, and M. Horiguchi, "Erbium-doped silica-based waveguide amplifier integrated with a 980/1530 nm WDM coupler," *Electron. Lett.*, vol. 30, no. 11, pp. 856–857, 1994.

[75] G. Zhang, S. Honkanen, A. Tervonen, C.-M. Wu, and I. Najafi, "Glass Integrated optics circuit for 1.48/1.55 and 1.3/1.55 μm wavelength division multiplexing and 1/8 splitting," *Appl. Opt.*, vol. 33, no. 16, pp. 3371–3374, 1994.

[76] T. Negami, H. Haga, and S. Yamamoto, "Guided-wave optical wavelength demultiplexer using an asymmetric y-junction," *Appl. Phys. Lett.*, vol. 54, pp. 1080–1082, 1989.

[77] F. Rottmann, A. Neyer, W. Mevenkamp, and E. Voges, "Integrated-optic wavelength multiplexers on Lithium Niobate based on two-mode interference," *J. Lightwave Technol.*, vol. 6, no. 6, pp. 946–952, 1988.

[78] C. F. Janz, M. R. Paiam, B. P. Keyworth, and J. N. Broughton, "Bent waveguide couplers for (de)multiplexing of broadly-separated wavelengths using two-mode interference," *IEEE Photon. Technol. Lett.*, vol. 7, no. 9, pp. 1037–1039, 1995.

[79] M. R. Paiam, C. F. Janz, R. I. MacDonald, and J. N. Broughton, "Compact planar 980/1550-nm wavelength multi/demultiplexer based on multimode interference," *IEEE Photon. Technol. Lett.*, vol. 7, no. 10, pp. 1180–1182, 1995.

[80] M. R. Paiam, C. F. Janz, R. I. MacDonald, B. P. Keyworth, and J. N. Broughton, "Compact planar waveguide couplers for broadband dual-channel wavelength (de)multiplexing," presented at the *ICAPT'96*, Montreal, Canada, July 1996.

[81] M. R. Paiam and R. I. MacDonald, "Polarization-insensitive 980/1550-nm wavelength (de)multiplexer using MMI couplers," *Electron. Lett.*, vol. 33, no. 14, pp. 1219–1220, 1997.

[82] C. H. Henry, G. E. Blonder, and R. F. Kazarinov, "Glass waveguides on silicon for hybrid optical packaging," *J. Lightwave Technol.*, vol. 7, no. 10, pp. 1530–1539, 1989.

[83] M. Krishnaswamy, J. N. McMullin, B. P. Keyworth, and J. S. Hayden, "Optical properties of strip-loaded Er-doped waveguides," *Optical Materials*, 6 (1996), pp. 287–292, 1996.

[84] A. V. Chelnokov, J.-M. Lourtioz, Ph. Boucaud, H. Bernas, J. Chaumont, and T. Plowman, "Deep high-dose erbium implantation of low-loss silicon oxynitride waveguides," *Electron. Lett.*, vol. 30, no. 22, pp. 1850–1851, 1994.

[85] ———, "Deep erbium-ytterbium implantation codoping of low-loss silicon oxynitride waveguides," *Electron. Lett.*, vol. 31, no. 8, pp. 636–638, 1995.

[86] M. V. Bazylenko, M. Gross, P. M. Allen, and P. L. Chu, "Fabrication of low-temperature PECVD channel waveguides with significantly improved loss in the 1.50-1.55-μm wavelength range," *IEEE Photon. Technol. Lett.*, vol. 7, no. 7, pp. 774–776, 1995.

[87] Hideaki Okayama and Takeshi Kamijoh, "Multiport wavelength routers using multimode interference," *Opt. Eng.*, vol. 36, no. 4, pp. 1078–1081, 1997.